Titre: Title:	Modeling and Control of a Parafoil-Based Guided Payload
Auteur: Author:	Olivier Fréchette
Date:	2024
Type:	Mémoire ou thèse / Dissertation or Thesis
Référence: Citation:	Fréchette, O. (2024). Modeling and Control of a Parafoil-Based Guided Payload [Mémoire de maîtrise, Polytechnique Montréal]. PolyPublie. https://publications.polymtl.ca/59423/

URL de PolyPublie: PolyPublie URL:	https://publications.polymtl.ca/59423/
Directeurs de recherche: Advisors:	David Saussié, & Sofiane Achiche
Programme: Program:	Génie aérospatial

POLYTECHNIQUE MONTRÉAL
affiliée à l'Université de Montréal

Modeling and Control of a Parafoil-Based Guided Payload

OLIVIER FRÉCHETTE
Département de génie électrique

Mémoire présenté en vue de l'obtention du diplôme de *Maîtrise ès sciences appliquées*
Génie aérospatial

Août 2024

POLYTECHNIQUE MONTRÉAL
affiliée à l'Université de Montréal

Ce mémoire intitulé :

Modeling and Control of a Parafoil-Based Guided Payload

présenté par **Olivier FRÉCHETTE**
en vue de l'obtention du diplôme de *Maîtrise ès sciences appliquées*
a été dûment accepté par le jury d'examen constitué de :

Luc BARON, président
David SAUSSIÉ, membre et directeur de recherche
Sofiane ACHICHE, membre et codirecteur de recherche
Bowen YI, membre

DEDICATION

To Sushi and Felix,
Forever curled up in my lap, your purrs cheered me on...

ACKNOWLEDGEMENTS

First and foremost, I would like to thank my supervisors David Saussié and Sofiane Achiche for giving me the opportunity to fully dive into the world of aerospace, robotics and control. Your support, patience, diligence, and flexibility were invaluable to my success.

Thank you as well to Lux Aerobot and MITACS for providing me the opportunity to gain hands-on experience by applying my skills in a real-world startup environment, and for their financial support which made this journey economically viable.

Thank you to everyone I worked alongside in the lab. You made for a great environment, surrounded by brilliant colleagues with various fields of expertise, and you were always happy to answer my questions about these subjects in which I am not an expert but which find fundamentally fascinating. Your diverse cultural and national backgrounds, combined with your curiosity and open-mindedness, led to many thought provoking discussions even outside of academic subjects. I felt like I was surrounded by geniuses, which was intimidating at first, but also wildly inspiring. In no specific order: Rémi, Lucas, Samy, Ahmad, Narimane, Cyrille, David, Christopher, Marc, Justin, Tzu-Yi, and Félix.

Thank you to all the students who attended the tutorial and laboratory sessions I instructed as a teaching assistant. Learning to apply and structure my knowledge of control theory in an educational context, where one has to reach an audience with varied learning styles contributed tremendously to cementing my fundamental understanding of the subject and my ability to give informative and engaging presentations.

Thank you to my friends, who were always there to listen to my technical explanations and help me unwind and recharge outside of work hours: Maya, Manel, Kiri, Guillaume, Daniel, Billie, Jacob, Tiko, Chris, and Eve.

Finally, thank you to my family for their continued presence and support throughout my studies. To my parents Janique and Philippe, you always welcomed me with open arms when I would come home to Québec for some much needed rest and recuperation, and enthusiastically listened to my progress updates and asked pertinent questions despite the field being completely foreign to you. To my sister Sarah, who was always there to provide advice and second opinions as my engineer-minded brain navigated the world of interpersonal affairs. To Coralie, the only one in my family who can rival my knowledge in internet culture. I love you all.

RÉSUMÉ

La dernière phase d'une mission d'un ballon stratosphérique est une descente en parachute, typiquement non guidée. L'atterrissage à un endroit désiré se limite à la sélection du point de déploiement du parachute selon des simulations a priori, après quoi aucun ajustement ne peut être effectué. Les descentes résultantes sont généralement imprécises et imprévisibles. Une alternative aux parachutes non guidés est l'utilisation d'un système basé sur un parafoil dirigeable. Ce mémoire présente la formulation et la démonstration d'une méthodologie pour la modélisation, l'identification, et la commande du cap et de la finesse d'un tel système.

Deux modèles dynamiques non linéaires de la littérature, avec 4 et 6 degrés de liberté (DDL), ont été analysés. Le système est contrôlé en raccourcissant les lignes de frein gauche et droite pour déformer le parafoil. Ces entrées sont converties en déflexion symétrique et asymétrique. Le réponse dynamique du système, ainsi que son évolution avec l'augmentation de l'altitude jusqu'à 18 km, a été analysée. Éclairé par ces observations, le modèle à 4 DDL a été mis à jour pour offrir une meilleure approximation de l'effet de l'altitude sur la dynamique latérale.

L'identification de paramètres du modèle à 4 DDL est réalisée par estimation du maximum de vraisemblance, à l'aide de données issues d'un récepteur GPS, une centrale inertielle et des encodeurs rotatif sur les actionneurs du système. Cette approche est validée en générant des données de vol simulées avec le modèle à 6 DDL, pour ensuite y appliquer la procédure d'identification et comparer la trajectoire du modèle identifié à celle du modèle original. Les résultats démontrent l'efficacité de cette méthode d'identification, même en présence de vent.

Un correcteur linéaire basé sur la linéarisation du modèle à 4 DDL est synthétisé grâce à une procédure combinant les commandes optimale et modale. Ce correcteur est ensuite séquencé en fonction de l'altitude. La performance et la robustesse du correcteur ont été testées en simulant le suivi d'une trajectoire balisée. Le correcteur latéral s'est avéré performant face aux variations en altitude, en vent et en présence d'erreurs de modélisation. Le correcteur longitudinal s'est avéré moins efficace, du fait des limitations physiques du parafoil et d'une faible robustesse face au vent. La loi de commande est tout de même bien adaptée pour le suivi d'une trajectoire au sol via le contrôle du cap.

Le rendu final est une approche accessible, à faible coût et conservatrice en quantité de calculs pour concevoir un algorithme de déscente guidé à base de parafoil. La principale limitation de la recherche est l'utilisation exclusive d'essais simulés pour la validation. Des travaux futurs comprenant une enquête plus approfondie comprenant des essais physiques sont proposées.

ABSTRACT

The last phase of a stratospheric balloon based mission consists of a parachuted descent, with typical operations using an unguided parachute. Control over the touchdown location is limited to pre-flight simulation and selection of the parachute deployment point, after which no further adjustments can occur. The resulting descent trajectories are generally inaccurate and unpredictable. An alternative is the use of a steerable parafoil-based system. The research presented is the formulation and demonstration of a methodology for the modeling, parameter identification and heading and glide ratio control of such a system.

Two non-linear dynamic models from literature with 4 and 6 degrees of freedom (DOF) were analysed. The system is controlled by shortening the left and right brake lines to deform the canopy. These inputs are processed into symmetric and asymmetric deflection. Steady-state and transient behavior, and their evolution of with increasing altitude up to 18 km was analysed. From these observations the 4-DOF model was refined with better modeling of altitude's effect on lateral dynamics.

Systems identification is performed for the 4-DOF model using output-error maximum likelihood estimation, using data from a GPS receiver, an IMU and a rotational encoder on each of the system actuators. Validation consisted of generating simulated noisy flight data with the 6-DOF model, applying the identification procedure to this data, and comparing the trajectories of the original and identified models when given the same sequence of inputs. An accurate 4-DOF approximation was successfully obtained in trials with atmospheric wind velocities ranging from 0 to 5 m/s.

A linear corrector based on the linearization of the 4-DDL model is synthesized using a procedure combining optimal and modal control. This corrector is then scheduled as a function of altitude. Effectiveness and robustness of the controller was tested through simulations of the 6-DOF model using a waypoint based trajectory. Lateral control proved reliable and accurate over variations in altitude, wind velocities and modeling errors. Longitudinal control was less effective, due to physical limitations in achievable glide ratio range, and weak robustness to the presence of wind. The controller is well suited to following a ground-track trajectory through heading control, but the limited longitudinal control suggests the use of alternate altitude regulation methods.

This work presents an accessible, low cost and computationally conservative approach for integrating a parafoil-based guided recovery system for high-altitude applications. The primary limitation of the research the exclusive use of simulated trials for validation. Further investigation using real-world flight tests and advanced wind modeling is proposed.

TABLE OF CONTENTS

LIST OF TABLES

LIST OF FIGURES

LIST OF SYMBOLS AND ABBREVIATIONS

Coordinate frames and rotations

$\mathcal{F}_o$	North-East-Down (NED) frame
$\mathcal{F}_b$	Body frame
$\mathcal{F}_p$	Canopy frame
$\mathcal{F}_s$	Stability frame
$\mathbf{R}_{b/o}$	NED frame to body frame rotation matrix
$\mathbf{R}_{b/s}$	Stability frame to body frame rotation matrix
$\mathbf{R}_{p/b}$	Body frame to canopy frame rotation matrix

Atmospheric variables

h	Altitude	km
ρ	Air density	$\mathrm{kg\,m^{-3}}$
P	Air pressure	Pa
T	Air temperature	K
g_0	Gravitational acceleration at sea level	$\mathrm{m\,s^{-2}}$
$\mathbf{W}$	Wind velocity vector $\mathcal{F}_o : \mathbf{W}^o = [w_N,\ w_E,\ w_D]^\top$	$\mathrm{m\,s^{-1}}$

Parafoil kinematics

$\boldsymbol{\omega}_{b/o}$	Angular velocity vector $\mathcal{F}_b : \boldsymbol{\omega}^b_{b/o} = [p,\ q,\ r]^\top$	$\mathrm{rad\,s^{-1}}$
$\mathbf{v}_{cm/o}$	Velocity vector $\mathcal{F}_o : \mathbf{v}^o_{cm/o} = [v_N,\ v_E,\ v_D]^\top$ $\mathcal{F}_b : \mathbf{v}^b_{cm/o} = [u,\ v,\ w]^\top$	$\mathrm{m\,s^{-1}}$
$\mathbf{p}$	Position vector $\mathcal{F}_o : \mathbf{p}^o = [p_N,\ p_E,\ p_D]^\top$	m
$\mathbf{\Phi}$	Euler angles vector	rad
ϕ	Roll angle	rad
θ	Pitch angle	rad
ψ	Yaw angle	rad
χ	Heading angle	rad
GR	Glide ratio	

Parafoil dynamics

$\mathbf{F}$	Total force vector	N
$\mathbf{F}_a$	Aerodynamic force vector	N
$\mathbf{F}_g$	Gravitational force vector	N
$\mathbf{F}_{am}$	Apparent mass force vector	N
$\mathbf{M}$	Total moment vector	N m
$\mathbf{M}_a$	Aerodynamic moment vector	N m
$\mathbf{M}_{ai}$	Apparent inertia moment vector	N m
K_ϕ	Roll gain	rad
T_ϕ	Roll time constant	rad

Aerodynamics

α	Angle of attack	rad
β	Sideslip angle	rad
$\mathbf{v}_a$	Airspeed vector	$\mathrm{m\,s^{-1}}$
V_T	Total airspeed	$\mathrm{m\,s^{-1}}$
$\bar{q}$	Dynamic pressure	Pa
C_D	Drag coefficient	
C_Y	Side force coefficient	
C_L	Lift coefficient	
C_l	Rolling moment coefficient	
C_m	Pitching moment coefficient	
C_n	Yawing moment coefficient	
$\mathbf{I}_{am}$	Apparent mass matrix	$\mathrm{m^3}$
$\mathbf{I}_{ai}$	Apparent inertia matrix	$\mathrm{m^5}$
$\mathbf{r}_{BP}$	Vector from real to apparent mass center	m

Actuator dynamics

$\bar{\delta}_l$	Normalized left brake deflection	
$\bar{\delta}_l$	Normalized right brake deflection	
δ_s	Symmetric brake deflection	
δ_a	Asymmetric brake deflection	
$\dot{\bar{\delta}}_{max}$	Maximum brake slew rate	$\mathrm{s^{-1}}$
T_δ	Brake time constant	s

Parameter identification

N	Number of recorded observations
$\mathbf{z}$	Measured outcome vector
$\mathbf{y}$	Expected outcome vector
n_y	Number of measured outputs
$\mathbf{u}$	Input vector
n_u	Number of inputs
$\boldsymbol{\Theta}$	Parameter vector
n_p	Number of system parameters
$\mathbf{R}$	Measurement noise covariance matrix

Control law synthesis

$\mathbf{x}$	State vector
n	Number of states
$\mathbf{u}$	Input vector
m	Number of inputs
$\mathbf{y}$	Output vector
p	Number of outputs
$\mathbf{z}$	Regulated output vector
q	Number of regulated outputs
$\mathbf{r}$	Setpoint vector
$\mathbf{K}$	State feedback gain matrix
$\mathbf{H}$	Feedforward gain matrix
$\mathbf{K}_i$	Integral gain matrix

LIST OF APPENDICES

CHAPTER 1 INTRODUCTION

1.1 Context

1.1.1 Wildland fires in Canada

In Canada, wildfires are of major concern due to their substantial effects on the economy, ecosystems, and local communities. With the ongoing effects of climate change, these impacts have only grown more significant.

Over the past ten years, a yearly average of around 7,000 fires have burned over 2.5 million hectares of land annually, with costs for suppression alone totaling close to $800 million per year. As a result, 70,000 people are affected annually and the number of evacuations averages 8,500. Between 1980 and 2017, both the number of evacuations and the number of evacuees have increased, and this trend is expected to continue [10] (Fig. 1.1). Among the key areas of research in wildfire management is the ability to "[assess] current fire activity by monitoring forest conditions, keeping track of current fires and evaluating the risk of new fires starting" [11].

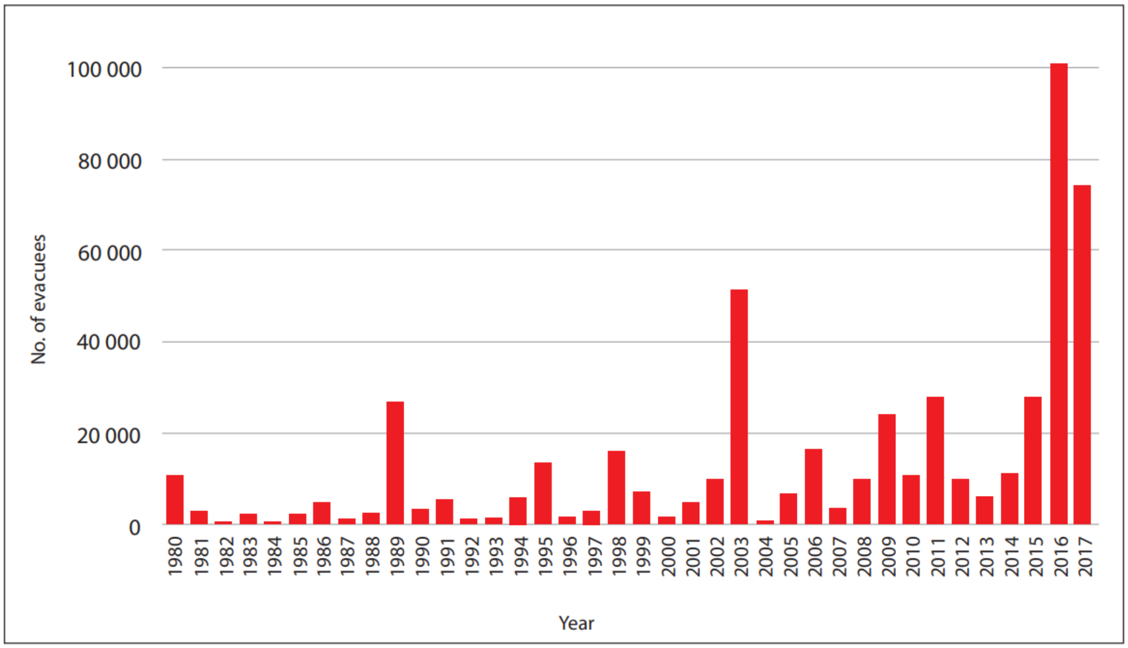

Figure 1.1 Number of wildfire evacuees in Canada (1980-2017), from [1]

Further supporting this point, according to the report entitled *Blueprint for wildland fire science in Canada (2019-2029)*, published by the Northern Forestry Center of Natural Resources

Canada, “Innovative science and technologies (such as remote sensing and earth observation tools) will allow for earlier and more accurate detection of fires and hot spots.[. . .] Enhanced fire monitoring and smoke forecasting will help to protect the health and safety of communities” [1]. Within this context, stratospheric balloon-based high-altitude Earth-observation platforms offer a promising source of added value.

1.1.2 Stratospheric balloons

Aerial Earth observation has proven to be an extremely useful tool for many applications including such environmental use cases as the aforementioned monitoring of forest fires and the identification and quantification of land erosion. Fixed-wing aircraft and satellites remain the two most common methods of this type of data acquisition, but both of these options present some drawbacks. Planes fly at a relatively low altitude and move at high speeds, which can present challenges in acquiring high-quality images. They are also costly to operate, with expenses including fuel, maintenance, and personnel. Satellites offer a high-altitude perspective but are costly to deploy, operate, and maintain.

Stratospheric balloon-based high-altitude platforms (HAPs) offer an in-between option by flying at altitudes of the order of 20 kilometers, in contrast to the typical aircraft altitude of 10 kilometers (approximately 35,000 feet) and Earth observation satellites, which operate at more than 500 kilometers from the Earth’s surface. HAPs are significantly cheaper than either aircraft or satellite-based imagery methods and operate beyond the typical altitude of commercial aircraft, thus avoiding the risk of interference and collision, other than during ascent and descent. They move much slower than aircraft and require less expertise than aircraft or satellites for operations and maintenance (Fig. 1.2).

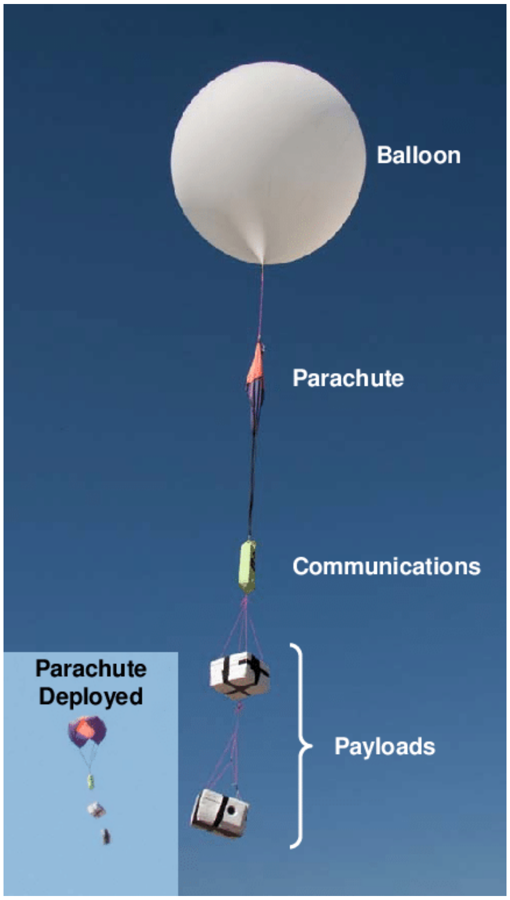

Figure 1.2 Typical configuration of a stratospheric balloon, from [2]

Lux Aerobot[1], the industrial partner for this research project, is an Alma-based startup

---

[1] https://www.luxaerobot.com/

with operations in Canada, Australia, and the UK. The company produces a HAP that can carry various types of payloads for clients to perform data acquisition. These include visible spectrum cameras, but also other methods of data collection, such as radio signal analysis and hyperspectral imaging. Their current projects include forest fire analysis, land erosion surveying, coastal ship surveillance, and invasive insect population analysis.

1.1.3 Recovery

Most stratospheric balloon missions can be roughly separated into four phases: (i) launch and ascent, (ii) float, (iii) descent, and (iv) recovery. Recovery is a significant part of ballooning operations, because most systems use an unguided parachute for the descent phase, making the exact landing location difficult to predict. An educated estimate can be obtained through simulation of the system using known wind predictions, but these predictions can be unreliable, especially for longer flights. Consequently, recovery operations tend to be mostly reactive, and there are risks involved in terms of the feasibility of the recovery (for example, if the system lands in a dense forest far from any roads), damage to equipment (e.g., from landing in water), and damage to infrastructure (although this can be mitigated by allowing for a large safety buffer when selecting a flight plan). From these risks, there emerges a tradeoff between ensuring a safe landing location – far from lakes, roads, and man-made structures – that allows for uncertainty on the exact touchdown point and finding a location that is easy to access for the recovery team.

From these facts, one can conclude that a guided descent system that can take as an input a desired landing location, and automatically navigate to a waiting recovery team, would offer significant benefits to ballooning operations. This is the context in which this research project was proposed.

Lux Aerobot's current recovery procedure consists of performing simulations to determine the optimal times for launch and flight termination to land in a desirable area. This is followed by confirming the true landing location through GPS trackers, and finally the dispatching of the recovery team to the true landing location. By allowing the HAP operator to select a specific landing zone in a desired location (e.g., an open field that is free of infrastructure and hazards, and easy to access), and having the recovery team on-site ready to receive it, this strategy would offer significant savings in recovery costs. It would also provide greater leeway in the launch and termination time windows (i.e., the beginning of the descent phase), and save on costs related to damaged or lost equipment.

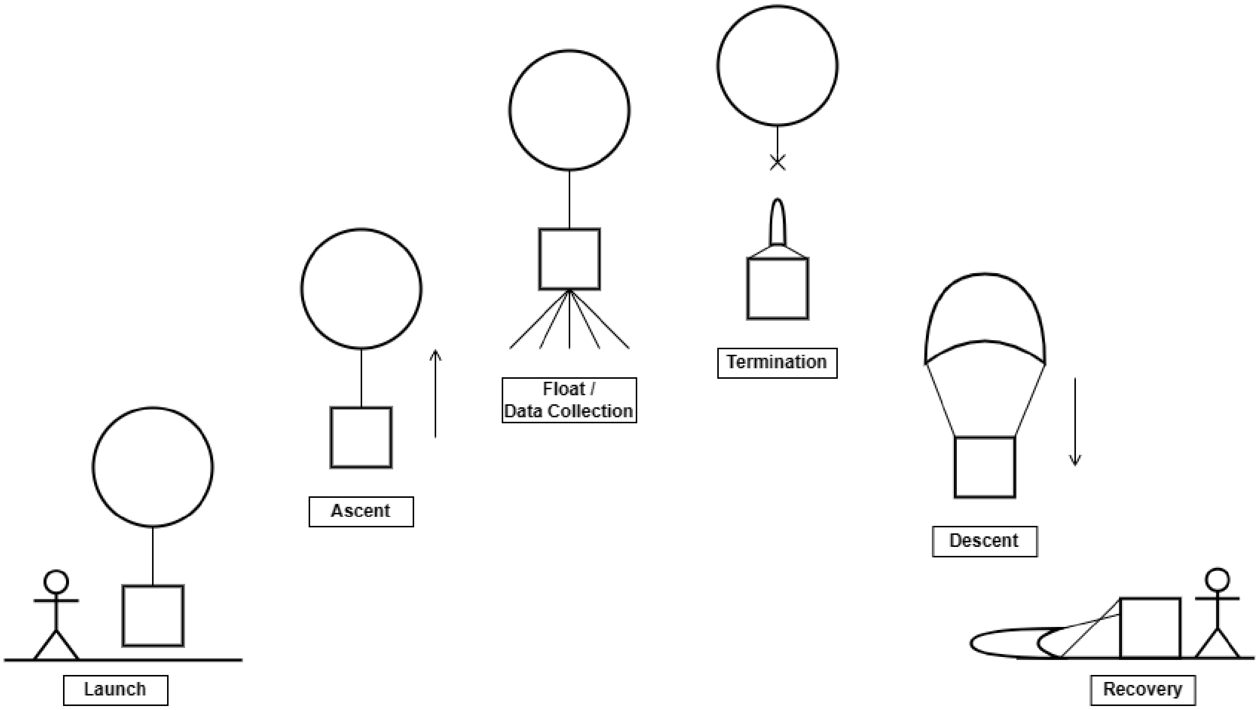

Figure 1.3 Typical procedure for a stratospheric balloon flight

1.1.4 PX4 Autopilot

Lux's system configuration makes use of a gondola equipped with a flight computer in the form of the Pixhawk 6C, a microcontroller running the open-source PX4 autopilot software [12]. Primarily designed for drones and remotely operated vehicles, this software offers a variety of functionalities useful for flight observation, control, and communication. While Lux's current use of the software is mainly limited to its communication and flight recording capabilities, PX4 offers powerful functionality relating to sensor compatibility and sensor fusion algorithms (namely Extended Kalman Filters) for measuring various states of the system. Critically, it also supports the implementation of fully customized control algorithms and actuator configurations. The current research is tailored to both make use of the available data outputs from this framework and the support for non-standard control inputs.

1.2 Objective

The main objective of this research project is to lay out the foundational theoretical work for the development of an autonomously guided descent vehicle for stratospheric Earth-observation platforms. This includes dynamical modeling, system identification, and control law synthesis.

The first step of this process is the nonlinear dynamic modeling using MATLAB and SIMULINK of the parafoil and payload system. This nonlinear model will serve as a tool for validating the effectiveness of the control laws synthesized further in the research process, as well as a source of simulated flight measurement data which will be used to perform system identification. The second step is the elaboration of a system identification procedure to estimate model parameters from collected flight data. This will allow the creation of a numerical model of the real-world system, which will then be the basis for control law synthesis. The third step is the synthesis of control laws using the parafoil model and identified parameters. The scope of the control laws to be synthesized as part of this project is limited to stabilization, heading control and glide slope control, enabling waypoint-based tracking and setting the groundwork for future work focused on trajectory planning. Finally, the developed control laws are validated and their performance evaluated through a series of simulated trials.

Further details on the sub-objectives, as well as the methodology for each, are provided later in Section 2.2.

1.3 Master's thesis outline

Chapter 2 presents a review of the existing literature relevant to the current project. It first explores the existing types of aerial delivery methods and the metrics for measuring their effectiveness, with a comparative analysis of the available solutions. We then explore previous work in the area of parafoil and payload system modeling and efforts to identify parameters for these systems. Third, we review the literature pertaining to the synthesis of linear control laws for nonlinear dynamic systems. The chapter concludes with a detailed overview of the research objectives and associated methodology.

Chapter 3 covers the creation and implementation of a 6-degree-of-freedom (DOF) dynamic model of a parafoil and payload system, based primarily on Oleg Yakimenko's work on the subject [13], and a simplified 4-DOF version presented by Thomas Jann [14]. The resulting behavior of each model is analyzed and both models are compared to determine the accuracy and limitations of the simplified model.

Chapter 4 follows up with the application of an output-error-based systems identification procedure and its application to simulated measured flight data from the 6-DOF model.

Chapter 5 presents the synthesis of a Linear Quadratic Regulator and modal based controller for heading and glide ratio control, using the identified parameters of the 4-DOF model. The controller design process also includes the implementation of gain scheduling to account for the varying atmospheric conditions resulting from the wide range of altitudes at which the system is expected to operate.

Finally, chapter 6 synthesizes the findings of this thesis, and discusses perspectives for future research following the foundation laid therein.

CHAPTER 2 LITERATURE REVIEW AND RESEARCH OBJECTIVES

As a starting point, this chapter presents a review of the existing literature relevant to this research project. First, Section 2.1.1 presents an overview of the various types of precision aerial delivery systems that have been explored over the years, and their advantages and disadvantages relevant to the considered application. It concludes with the selection of the appropriate method based on the defined project requirements. Next, Section 2.1.2 explores the various efforts made to model the dynamic behavior of parafoil and payload systems. Section 2.1.3 covers parameter identification methods for aerial systems, to obtain the model characteristics from collected flight data. Section 2.1.4 considers the synthesis of control laws for the developed system, with a focusing on linear control through LQR and modal control techniques.

Finally, the chapter concludes with a detailed description of the project's research objectives and the methodology for each objective.

2.1 Literature review

2.1.1 Aerial payload delivery methods

First of all, it is necessary to review the various possible methods for autonomous targeted delivery of an aerial payload. This problem has been studied extensively in the past, but with notable distinction from the context of the problem considered in this thesis; the majority of studies were performed within a military context, related to the delivery of cargo delivered via airplanes. This is an important distinction to make, particularly when it comes to considerations of cost-effectiveness. When performing military cargo drops, numerous payloads are released simultaneously, with the lower bound being in the double digits, in contrast to high altitude ballooning payloads which are released one at a time. For the applications in which such systems have been considered, the main requirements to be met deal with the safety of the delivery aircraft (i.e., distance from release point to landing location), touchdown accuracy, and cost-effectiveness. The majority of systems have strict requirements on the moment and location of release, and make use of computed aerial released point (CARP) to both determine the optimal moment for payload release and initiate deployment.

Application requirements

In the context of the current application, the key factors considered in this review are as follows:

- **Flexibility on release point location.** The trajectory of a high-altitude balloon is subject to a number of factors, many of which cannot be predicted with high accuracy. While simulations can often give reasonably accurate predictions, this is dependent on the accuracy of available wind data, and these can vary significantly between the time of simulation and launch, as well as between launch and the time of the platform reaching the location in question. Furthermore, possible issues with the flight termination system, caused by incomplete cutting of the release wire or delays in reception of the release signal can result in significant variations between the desired release point and the true release point.

- **Glide ratio.** As a consequence of the previous point, a high glide ratio can maximize the achievable range of the system (the ground distance between the release point and the target landing location)

- **No wind measurement tools.** Due to the high altitude of operations and mass budget limitations, the system must be able to function adequately without the use of additional onboard wind measurment tool (e.g., a drop sonde) at the time of release. Available wind profile estimates are limited to publicly available wind data, which are limited in resolution (both in time and position)

- **Wind penetration capability.** Errors in estimating the wind profile and unfavorable wind conditions can be compensated for by adequate penetration capability, enabling the system to navigate and operate effectively in varying wind conditions.

- **Number of actuators.** The power available on the gondola is limited and flights are long. Consequently, the number of actuators required must be reduced to a minimum to simplify the complexity of the control laws and the actuation energy required during descent.

- **Touchdown error.** To allow the gondola to land in a safe, desirable area, and as close as possible to the available recovery team, the descent must be carefully planned, and so touchdown error minimized.

- **Level of modification** required to the design of the current gondola, which uses an uncontrolled cruciform parachute, should be kept to a minimum

Non-parachute-based systems

Rotorcraft, such as quadcopters, were considered by Lux for the project but were rejected on two fronts. Firstly, rotor-based designs use active propulsion, in the form of four propellers that must be constantly actuated throughout the flight. Due to the strict budgeting of power required in the application of high-altitude ballooning, the high power requirements of constant actuation of the propellers are not compatible with the limited power resources available onboard the considered system. Secondly, by operating within the regulator context of high-altitude balloons within Canada, Lux can significantly simplify its logistical requirements relating to reporting and safety certification of its systems. Adding active propulsion systems runs the risk of changing the platform's classification to that of a remotely piloted aircraft system, which has much stricter regulatory requirements than high-altitude ballooning.

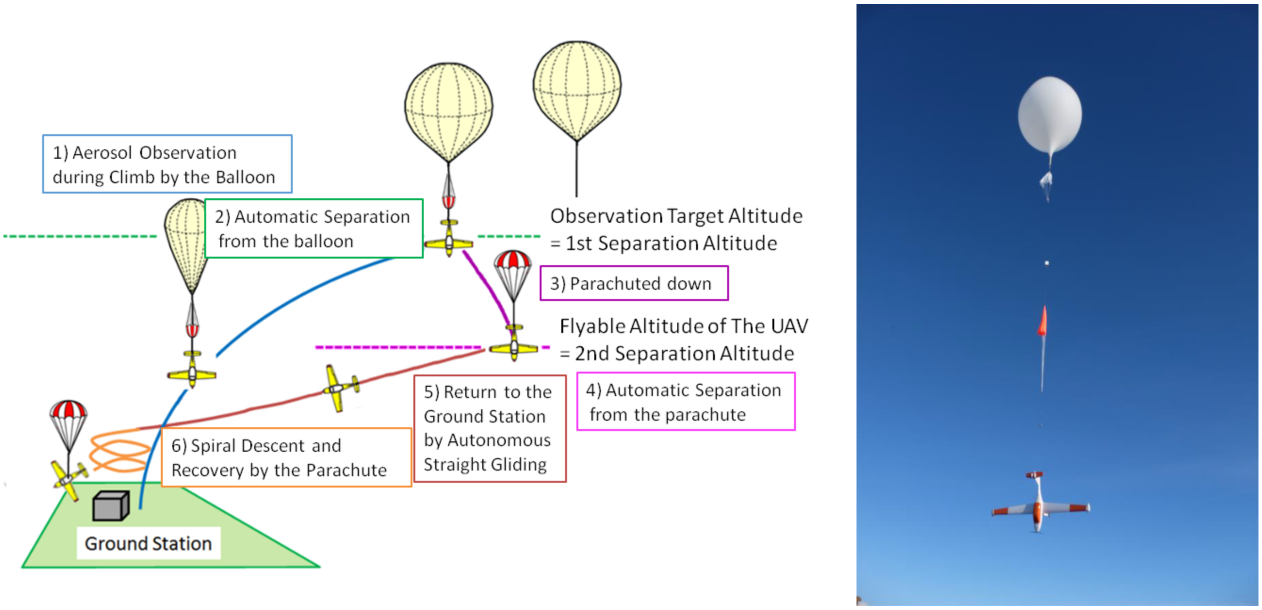

Figure 2.1 Glider-based recovery system, from [3]

Glider-based systems were also considered as in [3], where the gondola carried below the balloon is a UAV glider suspended with its nose down, which navigates to a ground station upon release from the lifting balloon (Fig. 2.1). The use of a glider offers significant advantages in terms of controllability and gliding capabilities. However, it would require a complete redesign of the gondola, as well as a significant quantity of added mass to the system in the form of the rigid airframe used in the glider. As with power, mass is tightly budgeted in the high-altitude platform, due to cost considerations (the heavier the system, the more costly helium gas must be used to gain and maintain altitude).

Parachute-based methods of recovery are therefore preferred to alternate methods due to their minimal effect on power and mass budget requirements for the complete system.

Circular parachute

Circular parachutes, due to their low cost and manufacturing complexity, have been the target of several studies on precision air delivery. Control is achieved through the use of actuators to deform the canopy and thus alter its aerodynamic characteristic, and the type of deformation used can be generally classified into two categories: asymmetric deformation and symmetric deformation.

In the first case, multiple actuators are used to obtain an asymmetric deformation of the canopy to induce a glide ratio to the parachute, as opposed to its uncontrolled ballistic trajectory. One such system, the Affordable Guided Airdrop System (AGAS) began development in the late 1990s in the context of precision military supply airdrops (Fig. 2.2). The concept was presented in [15] in 1999 and further explored in 2001 in [16]. It consists of a circular parachute attached to a payload with four pneumatic muscle actuators. Control is obtained by varying the actuator length through pressurization by onboard compressed nitrogen canisters. Circular parachutes have no forward direction, and therefore control can be exercised in four directions with no turning required. [15] estimates that the glide ratio of the uncontrolled chute is approximately 0.3, and a glide ratio of up to 0.5 can be achieved when control is exercised. [16] presents the results of flight testing of a scaled model with a 137 kg payload, which shows a nominal glide ratio of 0.4 to 0.5 during uncontrolled descent, and 0.5 to 1.0 during application of control inputs. Estimates of glide ratio in other studies of this type of system [4, 17, 18] provide similar values, ranging from 0.35 to 1.

Figure 2.2 The Affordable Guided Airdrop System, from [4]

In contrast, symmetric deformation of the canopy is achieved by incorporating a method of varying the canopy's drag during flight, usually through the use of a variable reefing mechanism (Fig. 2.3), as demonstrated in [19] and [20]. The resulting variable descent rate is used to take advantage of favorable winds. When an altitude is reached at which the wind is blowing towards the target, the descent rate is decreased to increase time spent in favorable

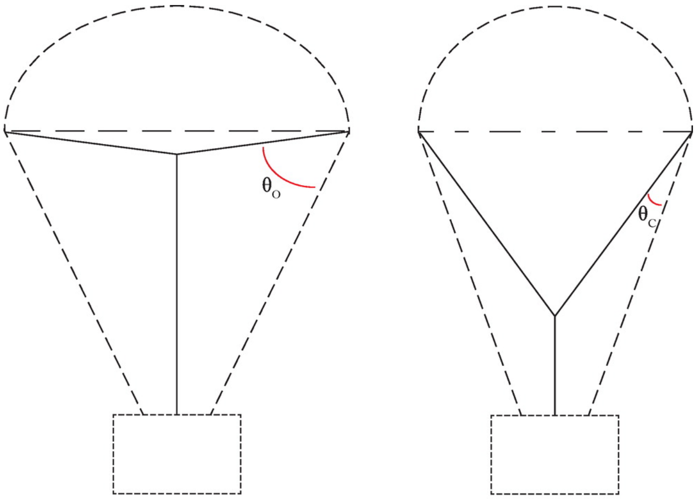

a) Fully Open

b) Fully Closed

Figure 2.3 Principle of a variable reefing mechanism, from [5]

wind conditions, and conversely the descent rate is increased in unfavorable wind conditions to limit the induced deviation from a desired trajectory. Notable disadvantages of this approach are twofold: such methods require accurate estimations of the wind profile during the descent to plan the sequence of reefing and disreefing of the chute, which is usually achieved through the use of drop sondes deployed along with the parachute; and the effectiveness of control is entirely dependent on the presence of favorable wind conditions. Since the system possesses no notable glide ratio or method of lateral control, flight conditions in which there is no wind, or if the wind profile along the descent is unfavorable, significantly diminish the effectiveness of the system.

Cruciform parachute

As an extension of the principle of asymmetric deformation described in the previous section, cruciform parachutes (Fig. 2.4) have also been studied for precision aerial delivery applications [6, 21–24]. This type of chute is generally composed of two identical rectangles of material sewn together perpendicularly in the middle, with risers attached on the ends of the rectangles, forming four distinct attachment points. Similarly to circular parachutes, their simple geometry and low control complexity make these systems a cost-effective method of achieving guided targeted descent of payloads.

While typical usage of this type of parachute – with all four risers set to a constant, equal length – will achieve similar ballistic, non-gliding trajectories to traditional circular parachutes, asymmetry introduced either through modification of the canopy geometry or the length of the risers can be used to induce a forward glide in the system. In the case of riser-based asymmetry, one of the suspension lines is statically shortened, and the adjacent suspension line is equipped with an actuator allowing dynamic variation of its length. When the controllable line is set to the same length as the static one, a forward glide is achieved. Varying the length to make the riser shorter or longer causes the system to rotate in one direction or another, enabling steering capabilities.

Figure 2.4 Cruciform parachute, from [6]

Notable advantages of this method are the low cost and minimal complexity of the system: in contrast to the AGAS, control can be achieved using as little as a single actuator. It also enables a purely vertical descent not achievable by high glide systems (such as parafoils) by entering a spin in which the forward glide is almost entirely neglected. However, current iterations of the system offer limited heading control accuracy, with [6] reporting a heading error of approximately 20 degrees. Glide ratio performance is also unsatisfactory, with [22] reporting glide ratios of $0.23 - 0.34$, and [6] obtaining realized glide ratios of $0.16 - 0.23$. In the second case, it is noted that the true glide ratio of the system is in fact in the range of $0.29 - 0.41$, but oscillations in trajectory resulting from the limited heading control account for a lower realized glide ratio than the theoretical maximum. As a consequence of this low glide ratio, as with the circular parachutes, effective control is dependent on accurate wind profile estimations, and wind penetration is limited to the average forward airspeed of such systems, with [6] stating that wind velocities higher than 2.2 m/s severely affect landing accuracy.

Parafoil

Parafoils (Fig. 2.5) have been extensively studied in the context of guided recovery, and remain the most widespread method used in the literature for guided recovery applications [25–27].

Parafoils offer several advantages compared to traditional unguided parachutes, the most notable being the introduction of a significant horizontal component to the velocity of the system. This forward component means that the parachute can be steered by adjusting the length of brake lines attached to the back of the canopy, which changes the shape and therefore the aerodynamic properties of the inflated wing. As a consequence, parafoils have a distinct forward direction inherent to their design, meaning that changes in direction can only be accomplished by inducing a yawing moment with asymmetric canopy deflection, in contrast to the multi-directional capabilities of a system such as the AGAS. Control is performed through asymmetric and symmetric deformation of the canopy, which is achieved by deflection of the left and right trailing edges of the inflated wing, thus requiring a total of two actuators. Parafoil-based systems also have the capability to perform a flare maneuver to shed forward velocity during the last moments of the flight, just prior to touchdown.

Figure 2.5 NASA's Spacewedge, an example of a parafoil-based recovery system, from [7]

Glide ratios demonstrated in the literature range from 1 to 4, and with appropriate control laws, reported touchdown accuracy can reach as high as 55 feet circular error probable [27].

Studies have also been performed on the performance of parafoil-based systems at high altitudes, with [25] performing tests at a deployment altitude of 57,000 feet to study the feasibility and stability of parafoils in low air density conditions. It was demonstrated that the parafoil could reliably deploy within such conditions, and that flight at these altitudes proved both stable and controllable.

Two notable disadvantages emerge from the literature. Firstly, due to added complexity in manufacturing, parafoils are less cost-effective than simpler designs like cruciform and circular parachutes. Secondly, they have slightly less flexible immediate control authority due to their changes in direction requiring a reorientation of the whole system. However, these are outweighed by the advantages brought about by the elimination of the need for accurate wind profile estimations and the high glide ratio, allowing for significantly more flexibility concerning the moment of deployment and range for the system.

Retained method

Following this analysis, the method retained for the guided recovery system is that of the parafoil. As it makes use of a flexible canopy, it provides key advantages in terms of mass and space requirements and requires the least modification to the gondola design for its integration into existing systems. Actuation is limited to two servomotors achieving left and right brake deflections, meaning limited power requirements and minimal added mass to enable control. Parafoils offer a high glide ratio, which allows a long range of possible landing locations, as well as wind penetration that makes it possible to navigate in adverse wind conditions, without the need to estimate the wind profile with great precision before the flight. The high glide ratio also means that there is considerable allowable error on the exact point of deployment of the system.

2.1.2 Mathematical modeling of the parafoil and payload system

Mathematical modeling of parafoil and payload systems has been the subject of a number of studies throughout the years, with the bulk of research work beginning in the late 1990s.

Most of these studies have been carried out for military applications, for the autonomous and targeted delivery of cargo payloads airdropped from planes in situations where accurate delivery, as well as safety of the delivering aircraft (achieved by maximizing the distance from release point to target landing area), were the primary considerations [28]. Other contexts have also been considered, however, such as the guided recovery of spacecraft payloads [29] and even the currently considered context of high-altitude ballooning [26].

Various levels of model fidelity can be achieved, depending on the required accuracy of the model for the considered application. In cases where only the system trajectory is considered, reasonable accuracy can be achieved using 3-DOF or 4-DOF models [14]. A 6-DOF model, which considers the payload and canopy as one rigid body, is required to adequately model both the longitudinal and lateral dynamics, and thus obtain further accuracy, especially when the system's attitude needs to be modeled [27,30,31]. Even further accuracy can be achieved with higher order models, going up to 12-DOF [32–35], to model the effects of relative motion (Fig. 2.6) between the payload and the canopy.

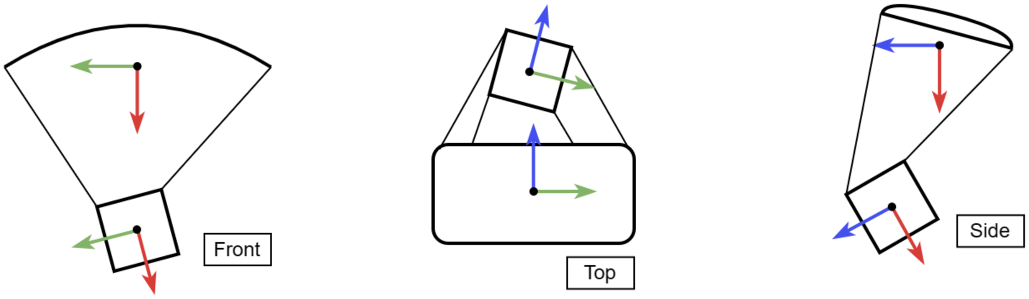

(a) Roll **(b)** Yaw **(c)** Pitch

Figure 2.6 Relative motion in the parafoil-payload system

A 6-DOF model is generally sufficient for accurate modeling of system behaviors for synthesis and validation of control laws, and higher fidelity modeling is helpful in cases where system identification is performed with sensing instrumentation directly on the payload, where the effects of relative motion induce errors in evaluating the state of the canopy [13].

Existing models that have been developed are distinguished by various features. Some models [14] focus only on the inertial position and flight trajectory. Others [27, 30–35] study both the flight path and local dynamics (roll, pitch, and yaw responses). Differences also occur when modeling the aerodynamic forces impacting the model, with different models including the effect of different state variables (angle of attack, sideslip angle, angular rates) when calculating the effect of the system state on the aerodynamic coefficients used for determining the resulting forces on the system. Another distinction emerges notably in lower fidelity 3-DOF and 4-DOF models [14] where certain system responses, particularly lateral response, are modeled through direct approximations of the kinetic effect of system inputs, rather than passing through the intermediate step of first calculating the induced forces followed by their impact on the system, through classical flight dynamics equations.

The forces impacting the dynamics of a parafoil and payload model are, at the most basic level, a combination of gravity and aerodynamic forces on the canopy and payload. Further accuracy is achieved by including apparent mass and inertia forces, which can be significant in the low mass-to-surface-area ratio context of a parafoil system, and these forces are typically included in models with 6 DOF and higher [13].

For control, the physical inputs considered are left and right brake deflection, which are then translated into the model inputs of symmetric and asymmetric deflections. Some models, such as the one presented in [36], also include the variation of the canopy angle of incidence[1] as an additional control input to obtain further control on the glide slope of the system.

Instrumentation used for data collection during flight testing includes GPS systems for inertial position and velocities, and accelerometers and gyroscopes to measure local linear accelerations and angular rates, respectively . Brake actuation is generally performed using servomotors, which provide positional feedback information, giving precise data on the state of the actuators at every point during the flight.

The two models of particular interest for this thesis are the 6-DOF model provided by Slegers and Yakimenko in [27], as well as the 4-DOF model outlined by Jann and Thomas in [14]. The 6-DOF model offers a relatively high-fidelity approximation of the behavior of the parafoil system while properly accounting for all the aerodynamic, gravitational, and apparent mass

---

[1] The relative angle between the payload and the canopy, which is a function of the relative length of the front and rear suspension lines.

forces and moments acting upon the system. This will allow for the generation – through simulation – of accurate flight data for analysis and provide a platform for validation of synthesized control laws. The simplified 4-DOF model offers a model with fewer parameters, facilitating system identification efforts, and eliminating the need for measurement and calculation of the inertia characteristics as a preliminary requisite for system identification. It has been shown to allow for accurate reproduction of the trajectory of the system, and its inclusion of roll angle as a system state is key, as this will be one of the measured values used in the synthesis of a controller for the system.

2.1.3 System identification

The effective elaboration of control laws for a given system requires accurate knowledge of the model's parameters. For this reason, the process of system identification, whose objective is to determine the numerical values of the model parameters from measured output responses to a series of known inputs, is an essential part of control law synthesis for real-world systems. These efforts are made more difficult by the presence of process and measurement noises, and the fact that not all system states are directly measurable. Figure 2.7 illustrates the factors at play when measuring the response of such a system.

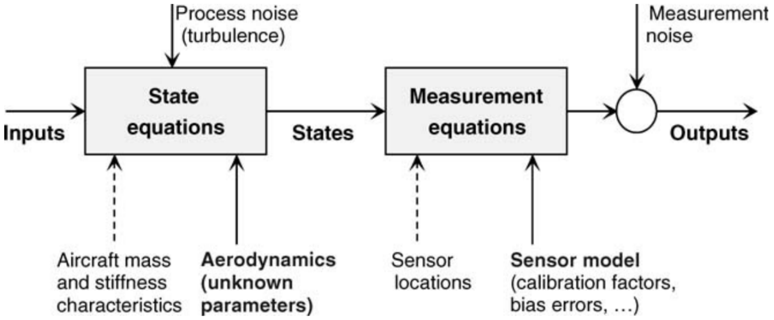

Figure 2.7 Block schematic of the system model for aircraft parameter estimation, from [8]

For the specific case of system identification of parafoil systems, [14] describes the effective use of the output-error method for identification of 3-DOF and 4-DOF parafoil models. Reference [37] further supports these results, by indicating that the two most suitable methods for identifying these types of systems are the output-error method, for the case where there is only measurement noise, and the filter-error method, which makes additional use of an extended Kalman filter for the case where process noise (e.g., wind turbulence) is also present.

Both of these methods belong to a class of methods known as response curve fitting, also known as output error. In this approach, an iterative process is used to optimize the model parameters to minimize the error between the measured variables (the system output) and the predicted responses (model output), leading to a nonlinear optimization problem. The method of weighted least squares is the simplest in this class of techniques, with the caveat that it requires prior knowledge of the weights to be applied. A more effective approach, based on probability theory, was presented by Fisher [38–40] and is known as the maximum likelihood method. Its general formulation can handle both process and measurement noises and reduces to the so-called output-error method in the case where only measurement noise is considered, i.e., when process noise is considered negligible. Figure 2.8 shows a block diagram of the general principle of this latter method.

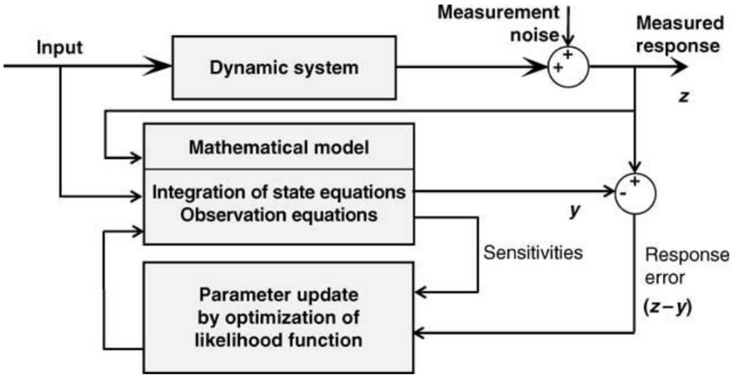

Figure 2.8 Block schematic of the output-error method, from [8]

The output-error method has been widely utilized for aircraft system identification since its introduction in the 1970s. While its application was initially limited to linear systems due to practical limitations of the time, this constraint was overcome through the use of a numerical approach, allowing for the generalization of the method to nonlinear systems of arbitrary complexity [41]. Jategaonkar [8] provides a detailed description of the theoretical foundation as well as the practical implementation of the output-error method.

2.1.4 Control strategies for parafoil-based systems

As the scope of the present research centers mainly around the modeling and identification of the parafoil system, the implementation of a control algorithm in this case serves primarily as a means of validating the usefulness and relevance of using a simplified model for control synthesis. Therefore we focus our study of the literature on inner loop control algorithms that enable the local tracking of heading and glide ratio setpoints. As such, we explore methods used to follow a generated trajectory (control), without overly dwelling on the way this trajectory was generated (guidance).

Early efforts for heading control include the work of Thomas Jann on the ALEX parafoil system in 2001 [14]. Using 3-DOF and 4-DOF models for simulation, it was determined that since the vehicle remains naturally stable for the large majority of its considered flight envelope, a very simple control law was an apt starting point for the task. Jann's research demonstrates the use of a saturation limited proportional controller, calculating a heading error from a commanded azimuth and the vehicles measured orientation. The resulting control input activates a single brake at a time, depending on the direction of the required turn. Using a waypoint-based trajectory, the approach proved viable during flight tests reaching altitudes of up to 450 m.

In an article published in 2005, Nathan Slegers [42] presents a model predictive control strategy for the control of a parafoil aircraft. He outlines a 6-DOF parafoil model which is then used as the basis for a reduced state 4-DOF linear model used by the predictive algorithm. Control inputs are determined by referencing a desired trajectory and using the known model to compute the estimated error over a finite future time horizon, and minimizing a quadratic cost function incorporating the estimated error and associated control efforts to determine the optimal inputs to be provided to the system. This strategy proved effective during a series of three autonomous flight tests at altitudes of up to 400 ft.

For the specific case of stratospheric applications, relevant research from the Guided Parafoil High Altitude Research Program provides insight on control considerations when operating at the much lower air densities present at high altitudes. In an article published in 2015 [25], the results from a test flight deployed from $57,122$ ft are presented. The test flight consisted of a first flight segment using a series of scripted left and right turn inputs, followed by fully autonomous flight starting from $12,000$ ft. While the publication does not provide a detailed explanation of the control strategy used, it highlight a number of considerations not yet mentioned in other, lower altitude research. Notably, the authors highlight that stable control is possible at high altitudes, but due to heightened lateral sensitivity input sequences must be much more conservative to avoid loss of control. An input scaling law based on current air density is proposed and demonstrated, and validated by the successful test flight.

Throughout the literature, it is commonly recognized that influence over glide ratio is largely limited when control inputs are restricted to simple brake deflection. Longitudinal control usually mainly consists of regulating forward velocity and performing flare maneuvers prior to landing. When the glide ratio is too high relative to the distance of a target, altitude is typically regulated through altitude dumping maneuvers, consisting of additional turns to extend the trajectory and avoid overshooting a given waypoint. This relegates managing the effective glide ratio of the system to a problem of trajectory selection rather than control.

More direct and effective glide slope control generally involves modifications to actuator configuration or parafoil geometry, leading to better landing accuracy at the cost of increased mechanical complexity. Examples of this include adding the means to vary the rigging angle of the canopy [36, 43] and introducing adjustable spoilers to the upper or lower surface of the canopy [44].

2.2 Research objectives

In light of the preceding literature review and the context established in Chapter 1, the main research objective of this research project can be summarized as follows:

Establish a framework for the modeling, system identification, and control of a parafoil-based autonomous return-to-point vehicle

This overarching goal can be separated into a set of four (4) specific sub-objectives, detailed in the following.

2.2.1 Sub-objective 1 – Create a dynamic model of a parafoil and payload system

Obtaining a nonlinear dynamic model of the parafoil system and its environment is a key step in synthesizing and validating control laws. With accurate modeling of the controlled system, the behavior of the system can be studied, control laws can be synthesized and validated in a realistic simulation environment. The simulation data thus obtained can also be used as a source of measurements for system identification.

Methodology

For this step, both the system and its environment must be modeled to obtain accurate data. Modeling includes inherent system properties such as inertia and mass values, gravitational and aerodynamic forces, and system reactions to control inputs. Modeling must also include the environment in which the system operates, notably the variable air density due to varying altitude and atmospheric wind conditions. Two models will be implemented: a 6-DOF model from [27] and a 4-DOF model from [14]. The 6-DOF model will be used for general analysis of system behavior and stability, and later for validation of the synthesized control laws. The 4-DOF model will be used to perform system identification and will be the basis for the control laws synthesized in later sections. Both models will be implemented in SIMULINK, with the aerodynamic coefficients used being those provided in their respective sources.

2.2.2 Sub-objective 2 – Perform system identification on simulated flight data

Being able to identify the system's aerodynamic characteristics from collected flight data is essential to provide a basis for the calculation of optimal gains during later control law synthesis. The method used must be able to obtain an accurate representation of the system's behavior from sensor data.

Methodology

System identification will be performed using the output-error method, as alluded to in [14] and detailed in [8], on simulated sensor data obtained from both models. First, a series of exciting maneuvers will be elaborated to obtain adequate data on the system's reaction to both symmetric and asymmetric deflection. Next, data will be collected from the simulation of the 4-DOF model, and identification performed on it. Using known parameters of the 4-DOF model will allow for simple validation of the accuracy of the identification. Thirdly, system identification will be performed using data collected from the 6-DOF model, to obtain the parameters of the 4-DOF approximation of the model. Validation will then be performed by comparing trajectory and attitude results in simulation. In both cases, various wind conditions will be considered to determine the limits of the method and the optimal exciting maneuvers.

2.2.3 Sub-objective 3 – Synthesize control laws for trajectory control of the parafoil system

An important requirement for an autonomous guided descent system is the ability to establish and follow a descent trajectory to eventually reach a desired landing point. Following such a trajectory requires regulating two key elements of the system's state: heading angle and glide ratio. With the variations in air density inherent to changes in operating altitude, which are further amplified by the wide range of operating altitudes, the controller must be able to remain stable and performant in spite of continually changing open loop dynamics.

Methodology

Synthesis of the control law will be performed in three main steps. First, using the parameters obtained through **SO2**, the 4-DOF model will be linearized about a steady glide at a chosen altitude, and LQR methods will be used to determine the positions of the closed-loop poles that will provide adequate system performance. This will be followed by performing eigenvalue assignment to calculate the required gains to obtain closed-loop dynamics that are as close as possible to their optimally calculated values while also decoupling lateral and longitudinal motion. Finally, these two steps will be repeated for a range of operating altitudes within the desired envelope, providing a basis for dynamically adjusting the controller through gain scheduling based on altitude. These adjustments will be key in ensuring stability and performance are retained for all possible altitudes.

2.2.4 Sub-objective 4 – Validate the performance of developed control laws through simulated trials in various atmospheric conditions

Finally, the control laws synthesized as a result of **SO3** from the 4-DOF model identified in **SO2** need to be validated on the more accurate 6-DOF model. This will allow analysis of the performance and robustness of the controller, as well as its feasibility in practical application.

Methodology

The control law established at the completion of **SO3** will first be applied to the 4-DOF simulated model to validate its performance on a perfectly-identified system. Next, the same controller will be applied to the full 6-DOF model to evaluate the resulting performance and the controller's robustness to modeling errors resulting from using a simplified model. Finally, the control law will be applied to the 6-DOF model with slightly modified parameters (aerodynamic coefficients and mass) to assess the algorithm's robustness. These parameters will be varied and tested multiple times using the Monte-Carlo approach, in order to obtain an overview of the robustness of the algorithm across a range of variations and to establish the limits of the control law obtained. Tests will also be carried out under variable wind conditions. Each validating simulation will go through a number of the established operating conditions to further validate the effectiveness of the gain-scheduling applied to the controller.

CHAPTER 3 NONLINEAR MODELING OF THE PARAFOIL AND PAYLOAD SYSTEM

This chapter covers the non-linear modeling of a parafoil and payload system. First, the working principle of a parafoil is explained. This is followed by the introduction of a 6-DOF non-linear model, based on rigid body flight dynamics, and the resulting system equations as described in the literature. Analysis is then performed, chiefly through simulation, on the behavior and stability of the model. Next, a simplified 4-DOF model is built from the 6-DOF model by applying a series of simplifying assumptions, with the objective of reducing the computational complexity of both the systems identification and control law computations, while maintaining accuracy. Finally, the accuracy of the 4-DOF model is validated through simulations comparing behavior of the simplified model to that of the 6-DOF model.

3.1 Ram-air chutes

Originally developed by Domina Jalbert in 1964, ram-air chutes, also commonly known as parafoils, are an alternative form of parachute that make use of air pressure to inflate an airfoil-shaped canopy. Ram-air chutes offer several advantages compared to traditional unguided parachutes. Most notable is the introduction of a significant forward horizontal velocity to the system, with the resulting glide ratio making it possible to traverse large horizontal distances as the parafoil makes its way back to Earth. Another important addition is the ability to control rotation about the vertical axis. Together these characteristics enable an operator to steer the payload towards a desired landing zone that can be located a significant distance away from the initial deployment point.

Structurally, the parafoil contains no rigid components, just like a traditional parachute. It can therefore be packed and stored in a small volume until needed. Once inflated, the canopy takes on an airfoil shape and behaves in a manner similar to that of a low aspect ratio wing. This profile is achieved with evenly spaced, airfoil-shaped ribs sewn longitudinally between the upper and lower surfaces of the canopy, forming individual cells between them. Openings along the leading edge allow air to enter and inflate the wing during flight, and apertures in the ribs ensure pressure equalization between the cells for uniform inflation. Suspension and control lines connect the canopy to the payload. Figure 3.1 highlights the typical components of a ram-air parachute system.

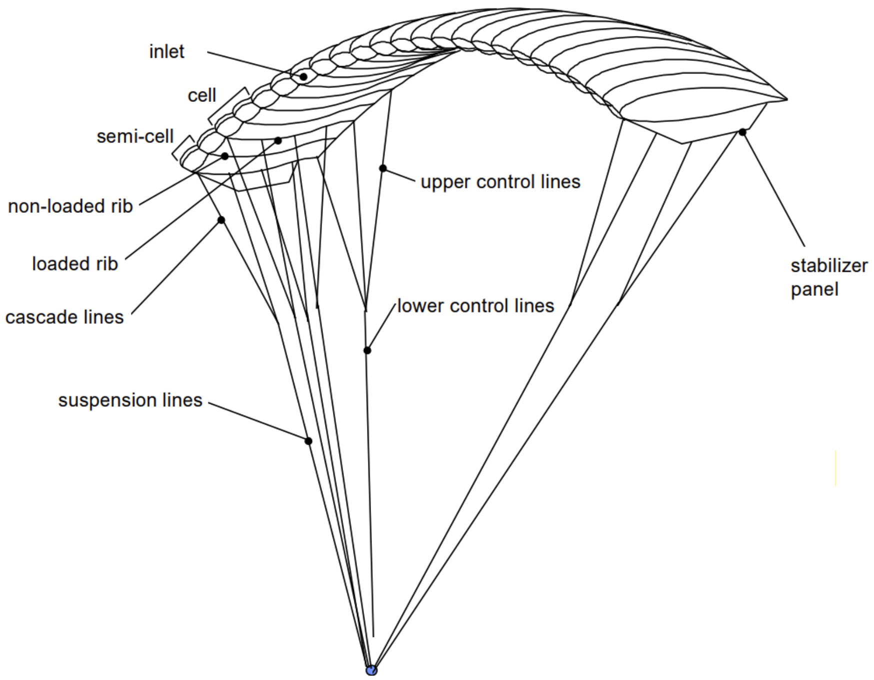

Figure 3.1 Elements of a ram-air parachute, taken from [9]

Control is achieved by adjusting the length of the two lower control lines to deform the trailing edge of the canopy. Asymmetric deflection provides lateral control and allows for steering. Symmetric deflection can be used to perform longitudinal maneuvers such as flares, and to vary the glide ratio. The two elementary quantities used as control inputs for the system are the length by which each of the control lines have been shortened, henceforth referred to as left and right brake deflection.

3.2 Notes on model fidelity

Several different levels of fidelity can be expressed by the model, reflected in the number of degrees of freedom it entails. For instance, 3-DOF and 4-DOF models offer the lowest computational cost and complexity, but each omits some level of information about the orientation of the system, which can limit the capabilities of controllers based on these models. A 6-DOF model provides further attitude information while considering the payload and canopy to be one rigid body, neglecting any relative rotation between the two bodies (Fig. 3.2). Accounting for this relative motion, higher fidelity models using up to 9 degrees of freedom have also been developed, as detailed in [13]. Table 3.1 provides a summary of the different levels of fidelity and the associated simplifications. Each entry describes an additional assumption, with the associated model also including the assumptions above it.

Fidelity	Description
9-DOF	The connection point between the canopy and payload is allowed full 3D linear movement, and both bodies can rotate relative to one another.
8-DOF	Relative rolling between the canopy and payload is neglected.
7-DOF	Relative pitching between the canopy and payload is neglected.
6-DOF	All relative motion between the canopy and payload is neglected: the system behaves as a single rigid body.
4-DOF	Rigid-body pitching and lateral velocity are neglected.
3-DOF	Rolling is neglected, leaving only forward velocity, sink rate, and yaw angle.

Table 3.1 Description of various possible levels of fidelity for a parafoil and payload model

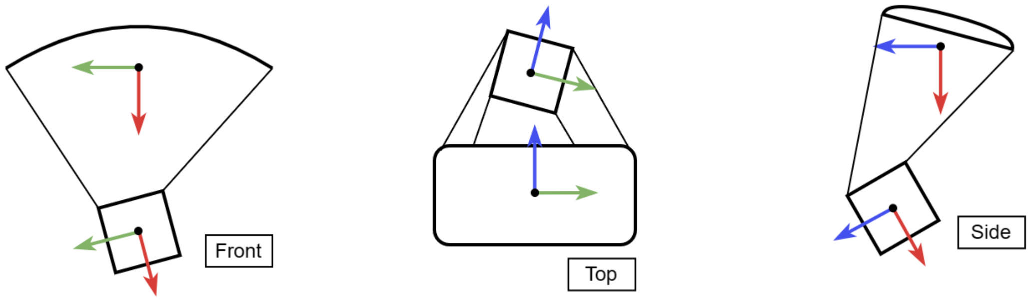

(a) Roll **(b)** Yaw **(c)** Pitch

Figure 3.2 Relative motion in the parafoil-payload system

This chapter will outline the equations of motion for both a 6-DOF model and a simplified 4-DOF model. The system identification algorithms detailed in Chapter 4 and the control law synthesis procedure in Chapter 5 will be applied to the 4-DOF model, with the resulting reduction in computational complexity rendering more feasible the implementation of these algorithms in onboard flight computers with limited processing power. The 6-DOF model will serve both as a source of simulated flight data to be used as the input for system identification and as a platform on which to validate the performance of the controller synthesized using the simplified model. Using two separate models with varying levels of fidelity allows for an approximation of the effect of using an imperfect mathematical model as a basis for developing a control strategy for a real-world system.

A number of simplifying assumptions have been applied in modeling the dynamics of the parafoil itself and the atmospheric conditions surrounding it. These assumptions will be laid out progressively in the relevant sections, and a full list of simplfying assumptions can be found in Appendix A.

3.3 Frames of reference and rotation matrices

Before diving into the equations of motion for the system, we must first establish the frames of reference upon which the various position, velocity, and acceleration vectors will be expressed. Four different frames of reference are used in the modeling of the behavior of the parafoil.

1. **Inertial (NED) frame** $\mathcal{F}_o = \{O_o,\ \mathbf{x}_o,\ \mathbf{y}_o,\ \mathbf{z}_o\}$
   The inertial frame, labeled $\mathcal{F}_o$, is a fixed frame with an arbitrary origin O_o. To facilitate atmospheric modeling, the origin along the z-axis is set to sea level. The x-y origin can be selected freely, with useful positions being the deployment point of the parafoil or the desired landing location. The convention followed by this frame is known as *North-East-Down* (NED). In other words, the $\mathbf{x}_o$ axis points North, $\mathbf{y}_o$ points East, and $\mathbf{z}_o$ points down, towards the center of the Earth.

2. **Body frame** $\mathcal{F}_b = \{O_b,\ \mathbf{x}_b,\ \mathbf{y}_b,\ \mathbf{z}_b\}$
   The body frame, labeled $\mathcal{F}_b$, is fixed to the body of the parafoil system, with its origin O_b positioned at the center of mass. This frame follows the *Front-Right-Down* convention. The $\mathbf{x}_b$ axis points towards the front of the vehicle, parallel to the payload. The $\mathbf{z}_b$ axis points downwards, perpendicular to $\mathbf{x}_b$, and the right-hand coordinate system is completed with the $\mathbf{y}_b$ axis pointing towards the right.

3. **Canopy frame** $\mathcal{F}_p = \{O_p,\ \mathbf{x}_p,\ \mathbf{y}_p,\ \mathbf{z}_p\}$
   The canopy frame, represented with $\mathcal{F}_p$, is used to model the difference in orientation between the canopy and the payload of the system, due to the rigging angle μ. Its origin O_p is placed at the aerodynamic center of the parafoil wing. Like the body frame, the canopy frame follows the *Front-Right-Down* convention, with the $\mathbf{x}_p$ axis pointing forward along the longitudinal axis of symmetry of the wing, the $\mathbf{y}_p$ axis pointing right and $\mathbf{z}_p$ pointing down.

4. **Stability frame** $\mathcal{F}_s = \{O_s,\ \mathbf{x}_s,\ \mathbf{y}_s,\ \mathbf{z}_s\}$
   The stability frame, represented with $\mathcal{F}_s$, is tied to the projection of the aerodynamic velocity vector onto the longitudinal axis of the vehicle. Its origin O_s is the center of mass. The $\mathbf{x}_s$ axis is oriented along the projection of the airspeed vector on the longitudinal plane of the body frame. The $\mathbf{y}_s$ axis is equivalent to the $\mathbf{y}_b$ axis, and the $\mathbf{z}_s$ axis completes the right-handed coordinate set.

Figure 3.3 shows the relative position and orientation of the non-inertial frames of reference $\mathcal{F}_b$, $\mathcal{F}_p$, and $\mathcal{F}_s$ overlaid with the parafoil and payload.

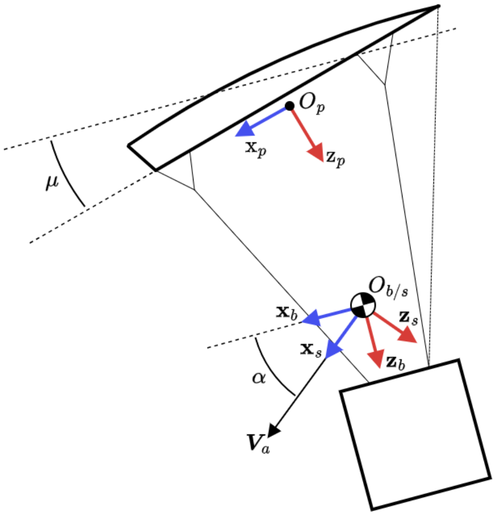

Figure 3.3 Non-inertial frames of reference on the parafoil

From a given frame of reference $\mathcal{F}_j$, a vector $\mathbf{x}^j$ expressed in this frame can be converted to its projection $\mathbf{x}^k$ in a destination frame of reference $\mathcal{F}_k$ by using the corresponding rotation matrix $\mathbf{R}_{k/j}$ which denotes the relative orientation of the two frames. Conversion in the opposite direction is achieved by inverting this rotation matrix.

$$\mathbf{x}^k = \mathbf{R}_{k/j}\mathbf{x}^j \Rightarrow \mathbf{x}^j = (\mathbf{R}_{k/j})^{-1}\mathbf{x}^k = \mathbf{R}_{j/k}\mathbf{x}^k \tag{3.1}$$

Furthermore, rotation matrices are orthogonal, and so their inverse is equal to their transpose.

$$\mathbf{R}_{j/k} = (\mathbf{R}_{k/j})^{-1} = \mathbf{R}_{k/j}^{\top} \tag{3.2}$$

To pass from the inertial frame to the body frame, three consecutive rotations are needed, by the Euler angles yaw, pitch, and roll. The convention followed is known as Z-Y-X Euler angles, from the order of the axes used for the consecutive rotations.

1. Rotation about the $\mathbf{z}_o$ axis by the yaw angle ψ. The resulting frame of reference is noted $\mathcal{F}_1 = \{O_1,\ \mathbf{x}_1,\ \mathbf{y}_1,\ \mathbf{z}_1\}$

2. Rotation about the $\mathbf{y}_1$ axis by the pitch angle θ. The resulting frame of reference is noted $\mathcal{F}_2 = \{O_2,\ \mathbf{x}_2,\ \mathbf{y}_2,\ \mathbf{z}_2\}$

3. Rotation about the $\mathbf{x}_2$ axis by the roll angle ϕ. The resulting frame of reference is the body frame $\mathcal{F}_b$

The three Euler angles are assembled into the vector $\mathbf{\Phi} \triangleq \begin{bmatrix}\phi & \theta & \psi\end{bmatrix}^\top$, with the corresponding rotation matrices being:

$$\mathbf{R}_\psi = \begin{bmatrix}\cos\psi & \sin\psi & 0\\ -\sin\psi & \cos\psi & 0\\ 0 & 0 & 1\end{bmatrix}, \mathbf{R}_\theta = \begin{bmatrix}\cos\theta & 0 & -\sin\theta\\ 0 & 1 & 0\\ \sin\theta & 0 & \cos\theta\end{bmatrix}, \mathbf{R}_\phi = \begin{bmatrix}1 & 0 & 0\\ 0 & \cos\phi & \sin\phi\\ 0 & -\sin\phi & \cos\phi\end{bmatrix} \tag{3.3}$$

They are combined to obtain the rotation matrix from the NED frame to the body frame, known as the Euler rotation matrix:

$$\begin{aligned}\mathbf{R}_{b/o} &= \mathbf{R}_\phi\mathbf{R}_\theta\mathbf{R}_\psi\\ &= \begin{bmatrix}\cos\theta\cos\psi & \cos\theta\sin\psi & -\sin\theta\\ \sin\phi\sin\theta\cos\psi - \cos\phi\sin\psi & \sin\phi\sin\theta\sin\psi + \cos\phi\cos\psi & \sin\phi\cos\theta\\ \cos\phi\sin\theta\cos\psi + \sin\phi\sin\psi & \cos\phi\sin\theta\sin\psi - \sin\phi\cos\psi & \cos\phi\cos\theta\end{bmatrix}\end{aligned} \tag{3.4}$$

Conversion from the stability frame to the body frame requires a rotation by the angle of attack α about their common $\mathbf{y}_s = \mathbf{y}_p$ axis:

$$\mathbf{R}_{b/s} = \mathbf{R}_\alpha = \begin{bmatrix}\cos\alpha & 0 & -\sin\alpha\\ 0 & 1 & 0\\ \sin\alpha & 0 & \cos\alpha\end{bmatrix} \tag{3.5}$$

Finally, the rotation matrix from the body frame to the canopy frame is a single rotation by the rigging angle μ about the $\mathbf{y}_b$ axis and is given by:

$$\mathbf{R}_{p/b} = \begin{bmatrix}\cos\mu & 0 & -\sin\mu\\ 0 & 1 & 0\\ \sin\mu & 0 & \cos\mu\end{bmatrix} \tag{3.6}$$

3.4 Modeling of atmospheric conditions

To accurately represent the behavior of the parafoil system, two external factors related to the atmosphere must also be modeled: airborne winds and the variation of atmospheric density with altitude. The latter is important to model as the parafoil, by its very nature, is constantly losing altitude, and over the course of its flight will operate in a range of air densities. This is especially true in the case of a recovery vehicle deployed from a stratospheric balloon, with operational altitudes reaching up to 20 km. As shown in section 3.9, these varations have a significant effect on the magnitude of the aerodynamic forces acting upon the system.

3.4.1 ISA atmosphere model

To model the variation of atmospheric density with altitude, we rely on the ISA atmosphere model, which is based on four elementary assumptions:

ASM–A1. Atmospheric conditions are constant in time.

ASM–A2. Air behaves as an ideal gas.

ASM–A3. The atmosphere has mass, and this mass induces a vertical pressure gradient that can be calculated through hydrostatic equilibrium.

ASM–A4. Temperature evolves linearly with altitude within a series of altitude segments.

From these assumptions, we can derive equations for obtaining the temperature T, air pressure P, and air density ρ as functions of altitude.

Altitude

We distinguish between two types of altitude for calculation of atmospheric conditions: geometric altitude h_G, which is the altitude from sea level, and geopotential altitude h which is obtained from the hydrostatic equation. Geopotential altitude can be determined from geometric altitude through the relationship

$$h = \frac{R_E}{R_E + h_G} h_G \tag{3.7}$$

with R_E the radius of the Earth at the position considered.

Air density

Per Assumption A2, air density can be calculated for a given temperature and pressure using the ideal gas law:

$$P = \rho R_s T \iff \rho = \frac{P}{R_s T} \tag{3.8}$$

where $R_s = 287$ J/(kg·K) is the specific gas constant for air.

Temperature

From Assumption A4, temperature is modeled as a constant gradient for each altitude segment, per the equation

$$T = T_1 + T_h(h - h_1) \tag{3.9}$$

where $T_h = \mathrm{d}T/\mathrm{d}h$ is the temperature gradient for the given segment. The subscript $\square_1$ indicates the value of a given atmospheric variable at the start of the current altitude segment. Table 3.2 shows the boundaries of the different altitude segments and the resulting equations for determining temperature within each segment.

Altitude h (km)	Gradient T_h (K/km)	Temperature T (Kelvin)
$0 < h < 11$	-6.5	$T_{0-11} = 288.15 - 6.5h$
$11 < h < 20$	0	$T_{11-20} = 216.65$
$20 < h < 32$	1.0	$T_{20-32} = 216.65 + (h - 20)$
$32 < h < 47$	2.8	$T_{32-47} = 228.65 + 2.8(h - 32)$
$47 < h < 52$	0	$T_{47-52} = 270.65$
$52 < h < 61$	-2.0	$T_{52-61} = 270.65 - 2(h - 52)$
$61 < h < 79$	-4.0	$T_{61-79} = 252.65 - 4(h - 61)$

Table 3.2 Variation of temperature with altitude in the ISA model

Atmospheric Pressure

Assumption A3 results in the equation

$$\frac{\mathrm{d}P}{\mathrm{d}h} = -\rho g_0 \tag{3.10}$$

where $g_0 \approx 9.81\mathrm{m/s}^2$ is the gravitational acceleration at sea level.

By combining Equations 3.8 and 3.10, we get:

$$\frac{\mathrm{d}P}{P} = -\frac{g_0}{R_s}\frac{\mathrm{d}h}{T} \tag{3.11}$$

Equation 3.11 can then be integrated to determine the pressure at a given altitude. For a segment with linearly varying temperature, this results in:

$$\int_{P_1}^{P} \frac{\mathrm{d}P}{P} = -\frac{g_0}{R_s}\int_{h_1}^{h} \frac{\mathrm{d}h}{T_1 + T_h(h - h_1)} \implies \frac{P}{P_1} = \left(\frac{T}{T_1}\right)^{-\frac{g_0}{R_s T_h}} \tag{3.12}$$

When considering an isothermic segment, the equation becomes:

$$\int_{P_1}^{P} \frac{\mathrm{d}P}{P} = \frac{g_0}{R_s T_1} \int_{h_1}^{h} \mathrm{d}h \implies \frac{P}{P_1} = e^{-\frac{g_0(h-h_1)}{R_s T_1}} \tag{3.13}$$

3.4.2 Wind

Airborne winds are modeled through a wind velocity vector $\mathbf{W}^o$ expressed in the NED frame. Two simplifying assumptions are made with regard to wind conditions:

ASM–A5. Wind velocities are constant over the duration of a flight segment.

ASM–A6. The wind has no vertical component.

From these assumptions, the wind vector is defined as

$$\mathbf{W}^o = \begin{bmatrix} w_N \\ w_E \\ 0 \end{bmatrix} \tag{3.14}$$

3.5 Kinematic equations

Two kinematic equations are necessary for modeling the behavior of a rigid body: the navigation equation and the Euler equation. The first establishes the relationship between the body-frame velocity and the NED frame velocity, and the second establishes the relationship between the body-frame angular velocity and the rates of the Euler angles.

Navigation equation

We denote $\mathbf{v}^b_{cm/o} \triangleq \begin{bmatrix} u & v & w \end{bmatrix}^\top$ the projection in the body frame $\mathcal{F}_b$ of the velocity of the center of mass relative to the inertial frame $\mathcal{F}_o$. We also define $\mathbf{p}^o \triangleq \begin{bmatrix} p_N & p_E & p_D \end{bmatrix}^\top$ the position of the center of mass expressed in the NED frame. By taking the derivative of $\mathbf{p}^o$ in the inertial frame, we obtain the NED frame velocity $\mathbf{v}^o_{cm/o} \triangleq \begin{bmatrix} v_N & v_E & v_D \end{bmatrix}^\top$ through the navigation equation:

$${}^o\dot{\mathbf{p}}^o = \mathbf{v}^o_{cm/o} = \mathbf{R}_{o/b}\mathbf{v}^b_{cm/o} \tag{3.15}$$

Euler rates equations

We define $\boldsymbol{\omega}^b_{b/o} \triangleq \begin{bmatrix} p & q & r \end{bmatrix}^\top$ the angular velocity vector of $\mathcal{F}_b$ relative to $\mathcal{F}_o$, expressed in the body frame. The relationship between $\boldsymbol{\omega}^b_{b/o}$ and the variation of the Euler angles $\dot{\boldsymbol{\Phi}}$ is as follows:

$$\boldsymbol{\omega}^b_{b/o} = \begin{bmatrix}\dot{\phi}\\0\\0\end{bmatrix} + \mathbf{R}_\phi\left(\begin{bmatrix}0\\\dot{\theta}\\0\end{bmatrix} + \mathbf{R}_\theta\begin{bmatrix}0\\0\\\dot{\psi}\end{bmatrix}\right) \Rightarrow \begin{bmatrix}p\\q\\r\end{bmatrix} = \begin{bmatrix}1 & 0 & -\sin\theta\\0 & \cos\phi & \sin\phi\cos\theta\\0 & -\sin\phi & \cos\phi\cos\theta\end{bmatrix}\begin{bmatrix}\dot{\phi}\\\dot{\theta}\\\dot{\psi}\end{bmatrix} \tag{3.16}$$

The inverse relation is then:

$$\begin{bmatrix}\dot{\phi}\\\dot{\theta}\\\dot{\psi}\end{bmatrix} = \begin{bmatrix}1 & \sin\phi\tan\theta & \cos\phi\tan\theta\\0 & \cos\phi & -\sin\phi\\0 & \sin\phi/\cos\theta & \cos\phi/\cos\theta\end{bmatrix}\begin{bmatrix}p\\q\\r\end{bmatrix} \tag{3.17}$$

3.6 Generic rigid body flight dynamics

To model the dynamics of the system, we first establish the general equations governing the relationships between angular and linear accelerations and the applied forces and moments for a typical 6-DOF rigid body. Two additional simplifying assumptions relating to the dynamics are introduced here.

ASM–D1. The parafoil operates on a flat, non-rotating Earth with constant gravitational acceleration.

ASM–D2. The payload and canopy act as a single rigid body.

3.6.1 Linear dynamics

Applying Newton's second law in an inertial frame of reference gives us the relation:

$$m\,{}^o\mathbf{a}_{cm/o} = m\,{}^o\dot{\mathbf{v}}_{cm/o} = \sum \mathbf{F} \tag{3.18}$$

where m is the mass of the parafoil system, $\mathbf{a}^o_{cm/o} = \dot{\mathbf{v}}^o_{cm/o}$ is the linear acceleration of the center of mass in the inertial frame, and $\mathbf{F}$ is the total sum of external forces acting upon the system. However, since the forces considered will be applied to the non-inertial frame of reference $\mathcal{F}_b$, the Coriolis equation must be applied when describing the relationship between the inertial acceleration and the body-frame acceleration, requiring the reintroduction of the angular velocity vector $\boldsymbol{\omega}_{b/o}$;

$${}^o\dot{\mathbf{v}}_{cm/o} = {}^b\dot{\mathbf{v}}_{cm/o} + \boldsymbol{\omega}_{b/o} \times \mathbf{v}_{cm/o} \tag{3.19}$$

The linear dynamics equations expressed in the body frame therefore become:

$$m({}^{b}\dot{\mathbf{v}}^{b}_{cm/o} + \boldsymbol{\omega}^{b}_{b/o} \times \mathbf{v}^{b}_{cm/o}) = \mathbf{F}^{b} \tag{3.20}$$

where $\mathbf{F}^{b} = \begin{bmatrix} X & Y & Z \end{bmatrix}^{\top}$ is the sum of forces applied expressed in the body frame. Isolating the accelerations, we obtain the equation:

$$\begin{bmatrix} \dot{u} \\ \dot{v} \\ \dot{w} \end{bmatrix} = \frac{1}{m}\begin{bmatrix} X \\ Y \\ Z \end{bmatrix} - \begin{bmatrix} p \\ q \\ r \end{bmatrix} \times \begin{bmatrix} u \\ v \\ w \end{bmatrix} \tag{3.21}$$

3.6.2 Rotational dynamics

For rotational dynamics, we establish the relationship between applied moments and the rate of change of angular momentum $\dot{\mathbf{h}}_{cm}$ of a system. In an inertial frame, we have:

$${}^{o}\dot{\mathbf{h}}_{cm} = \sum \mathbf{M}_{cm} \tag{3.22}$$

As with linear acceleration, Coriolis is applied to transition to the non-inertial body frame:

$${}^{o}\dot{\mathbf{h}}_{cm} = {}^{b}\dot{\mathbf{h}}_{cm} + \boldsymbol{\omega}_{b/o} \times \mathbf{h}_{cm} = \sum \mathbf{M}_{cm} \tag{3.23}$$

Converting to the body frame, we use the relation between angular momentum $\mathbf{h}_{cm}$, the inertia matrix $\mathbf{I}$ and angular velocity:

$$\mathbf{h}^{b}_{cm} = \mathbf{I}^{b}\boldsymbol{\omega}^{b}_{b/o} \tag{3.24}$$

which results in the equation:

$$\mathbf{I}^{b}\,{}^{b}\dot{\boldsymbol{\omega}}^{b}_{b/o} + \boldsymbol{\omega}^{b}_{b/o} \times \mathbf{I}^{b}\boldsymbol{\omega}^{b}_{b/o} = \mathbf{M}^{b} \tag{3.25}$$

where $\mathbf{M}^{b} = \begin{bmatrix} L & M & N \end{bmatrix}^{\top}$ is the sum of forces applied expressed in the body frame. Isolating the angular accelerations, we get:

$$\begin{bmatrix} \dot{p} \\ \dot{q} \\ \dot{r} \end{bmatrix} = (\mathbf{I}^b)^{-1} \left(\begin{bmatrix} L \\ M \\ N \end{bmatrix} - \begin{bmatrix} p \\ q \\ r \end{bmatrix} \times \mathbf{I}^b \begin{bmatrix} p \\ q \\ r \end{bmatrix} \right) \tag{3.26}$$

3.7 6-DOF parafoil model

3.7.1 Forces and moments

The total forces and moments acting on the parafoil are a sum of aerodynamic forces and moments, gravitational forces, and apparent mass and inertia effects.

$$\mathbf{F}^b = \mathbf{F}_a^b + \mathbf{F}_g^b + \mathbf{F}_{am}^b \tag{3.27}$$

$$\mathbf{M}^b = \mathbf{M}_a^b + \mathbf{M}_{ai}^b \tag{3.28}$$

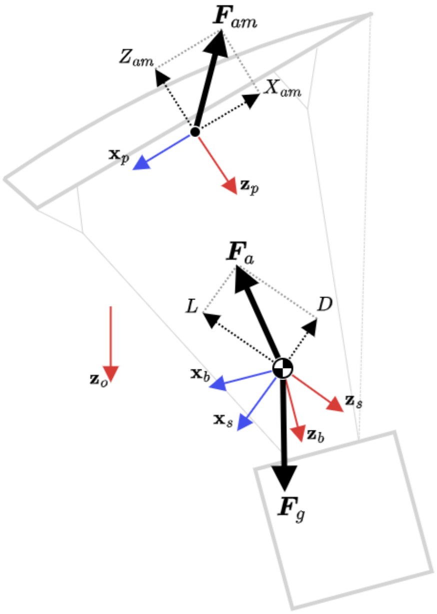

Figure 3.4 Side view of the forces acting on the parafoil

3.7.2 Gravitational forces

The gravitational force vector is obtained from the projection of the weight vector into the body frame.

$$\mathbf{F}_g^b = \mathbf{R}_{b/o}\begin{bmatrix}0\\0\\mg_0\end{bmatrix}^o = mg_0\begin{bmatrix}-\sin\theta\\ \sin\phi\cos\theta\\ \cos\phi\cos\theta\end{bmatrix} \tag{3.29}$$

3.7.3 Aerodynamic forces and moments

Calculation of aerodynamic forces and moments first requires the definition of an airspeed vector $\mathbf{v}_a^b$, expressed in the body frame, which is calculated by combining the inertial velocity and wind vectors. This vector represents the velocity of the system relative to the air surrounding it:

$$\mathbf{v}_a^b = \mathbf{v}_{cm/o}^b - \mathbf{R}_{b/o}\mathbf{W}^o \Rightarrow \begin{bmatrix}u_a\\v_a\\w_a\end{bmatrix} = \begin{bmatrix}u\\v\\w\end{bmatrix} - \mathbf{R}_{b/o}\begin{bmatrix}w_N\\w_E\\0\end{bmatrix} \tag{3.30}$$

We can use this to define total airspeed V_T, angle of attack α, and sideslip angle β:

$$\alpha = \arctan\frac{w_a}{u_a} \tag{3.31a}$$

$$V_T = ||\mathbf{v}_a^b|| = \sqrt{u_a^2 + v_a^2 + w_a^2} \tag{3.31b}$$

$$\beta = \arcsin\frac{v_a}{V_T} \tag{3.31c}$$

From the total airspeed and air density, we can calculate dynamic pressure $\bar{q}$, which represents the total kinetic energy per unit of fluid:

$$\bar{q} = \frac{1}{2}\rho V_T^2 \tag{3.32}$$

To calculate the total aerodynamic forces, we multiply the dynamic pressure and canopy surface area S by the aerodynamic force coefficients C_D, C_Y, and C_L, which represent the lift coefficient, side force coefficient, and drag coefficient respectively. Since the lift and drag forces act opposite to the airspeed vector, their coefficients appear as negative. The resulting forces are given in the stability frame and must be projected into the body frame using $\mathbf{R}_{b/s}$.

$$\mathbf{F}_a^b = \begin{bmatrix} X_a \\ Y_a \\ Z_a \end{bmatrix} = \bar{q}S\mathbf{R}_{b/s} \begin{bmatrix} -C_D \\ C_Y \\ -C_L \end{bmatrix} \tag{3.33}$$

Similarly, we calculate the aerodynamic moments using the canopy span b, canopy chord c, rolling coefficient C_l, pitching coefficient C_m, and yawing coefficient C_n:

$$\mathbf{M_a} = \begin{bmatrix} L_a \\ M_a \\ N_a \end{bmatrix} = \bar{q}S \begin{bmatrix} bC_l \\ cC_m \\ bC_n \end{bmatrix} \tag{3.34}$$

The force and moment aerodynamic coefficients are modeled using the relevant partial derivatives, geometric parameters and system states. Also included are the control inputs δ_a and δ_s, representing asymmetric and symmetric brake deflection. As outlined in [27], the coefficients are calculated as follows:

$$C_D = C_{D0} + C_{D\alpha 2}\alpha^2 + C_{D\delta s}\delta_s \tag{3.35a}$$

$$C_Y = C_{Y\beta}\beta \tag{3.35b}$$

$$C_L = C_{L0} + C_{L\alpha}\alpha + C_{L\delta s}\delta_s \tag{3.35c}$$

$$C_l = C_{l\beta}\beta + C_{l\delta a}\delta_a + \frac{b}{2V_T}(C_{lp}p + C_{lr}r) \tag{3.35d}$$

$$C_m = C_{m0} + C_{m\alpha}\alpha + \frac{c}{2V_T}C_{mq}q \tag{3.35e}$$

$$C_n = C_{n\beta}\beta + C_{n\delta a}\delta_a + \frac{b}{2V_T}(C_{np}p + C_{nr}r) \tag{3.35f}$$

3.7.4 Apparent mass and inertia

Apparent mass and inertia forces originate from the effect of induced pressure forces resulting from the inertia of the air which is displaced by the airborne system during flight. Their effect is inversely proportional to the ratio of system mass to the displaced air mass. In most airborne systems, such as aircraft, this ratio is low enough to be neglected, but in the case of parafoil systems, it is significant enough to have a marked effect on system dynamics.

To model these forces, we first define the apparent mass and apparent inertia matrices. The components of these matrices can be estimated through geometric calculations and then refined through systems identification methods, as further detailed in [13].

$$\mathbf{I}_{am} = \begin{bmatrix} A & 0 & 0 \\ 0 & B & 0 \\ 0 & 0 & C \end{bmatrix} \qquad \mathbf{I}_{ai} = \begin{bmatrix} I_A & 0 & 0 \\ 0 & I_B & 0 \\ 0 & 0 & I_C \end{bmatrix} \tag{3.36}$$

Apparent mass and inertia depend principally on the mass of air displaced by the canopy. We therefore first express the forces in the canopy frame $\mathcal{F}_p$, which is distinct from the body frame due to the non-zero rigging angle μ. The forces are also applied at the apparent mass center (defined in this case to be coincident with the origin of $\mathcal{F}_p$) which means that the aerodynamic velocity vector must be adjusted to include the effect of the system rotating about its center of mass.

For this purpose, we first define the vector from the system mass center to the apparent mass center,

$$\mathbf{r}^b_{BP} = \begin{bmatrix} x_{BP} & y_{BP} & z_{BP} \end{bmatrix}^\top \tag{3.37}$$

then establish the relevant equations for the airspeed and angular velocity at the apparent mass center, in the canopy frame.

$$\tilde{\mathbf{v}}_a = \begin{bmatrix} \tilde{u}_a \\ \tilde{v}_a \\ \tilde{w}_a \end{bmatrix} = \mathbf{R}_{p/b} \left(\begin{bmatrix} u \\ v \\ w \end{bmatrix} + \begin{bmatrix} p \\ q \\ r \end{bmatrix} \times \begin{bmatrix} x_{BP} \\ y_{BP} \\ z_{BP} \end{bmatrix} - \mathbf{R}_{b/o}\mathbf{W} \right) \tag{3.38}$$

$$\tilde{\boldsymbol{\omega}} = \begin{bmatrix} \tilde{p} \\ \tilde{q} \\ \tilde{r} \end{bmatrix} = \mathbf{R}_{p/b} \begin{bmatrix} p \\ q \\ r \end{bmatrix}, \quad \dot{\tilde{\boldsymbol{\omega}}} = \begin{bmatrix} \dot{\tilde{p}} \\ \dot{\tilde{q}} \\ \dot{\tilde{r}} \end{bmatrix} = \mathbf{R}_{p/b} \begin{bmatrix} \dot{p} \\ \dot{q} \\ \dot{r} \end{bmatrix} \tag{3.39}$$

We can then express the apparent mass and inertia forces in the canopy frame. Note that the apparent mass and inertia coefficients given in the literature follow the convention $\rho = 1\ \text{kg/m}^3$ and vary proportionally to air density. Due to the large variations in air density present in the range of considered altitudes, the matrices are multiplied by ρ when calculating the relevant forces:

$$\mathbf{F}^p_{am} = -\rho\Big(\mathbf{I}_{am}\dot{\tilde{\mathbf{v}}}_a + \tilde{\boldsymbol{\omega}}_{b/o} \times \mathbf{I}_{am}\tilde{\mathbf{v}}_a\Big) \tag{3.40}$$

$$\mathbf{M}^p_{ai} = -\rho\Big(\mathbf{I}_{ai}\dot{\tilde{\boldsymbol{\omega}}}_{b/o} + \tilde{\boldsymbol{\omega}}_{b/o} \times \mathbf{I}_{ai}\tilde{\boldsymbol{\omega}}_{b/o} + \tilde{\mathbf{v}}_a \times \mathbf{I}_{am}\tilde{\mathbf{v}}_a\Big) \tag{3.41}$$

In the interest of readability, we define two intermediate inertia matrices before projecting the above equation into the body frame:

$$\mathbf{I}'_{am} = (\mathbf{R}_{p/b})^\top \mathbf{I}_{am} \mathbf{R}_{p/b} \tag{3.42}$$

$$\mathbf{I}'_{ai} = (\mathbf{R}_{p/b})^\top \mathbf{I}_{ai} \mathbf{R}_{p/b} \tag{3.43}$$

To finally obtain the apparent mass and inertia forces and moments equations expressed in the body frame:

$$\mathbf{F}^b_{am} = -\rho\Big(\boldsymbol{\omega}^b_{b/o} \times \mathbf{I}'_{am}(\mathbf{v}^b_a - \mathbf{r}^b_{BP} \times \boldsymbol{\omega}^b_{b/o}) + \mathbf{I}'_{am}(\dot{\mathbf{v}}^b_{cm/o} - \mathbf{r}^b_{BP} \times \dot{\boldsymbol{\omega}}^b_{b/o})\Big) \tag{3.44}$$

$$\mathbf{M}^b_{ai} = \mathbf{r}^b_{BP} \times \mathbf{F}^b_{am} - \rho(\mathbf{I}'_{ai}\dot{\boldsymbol{\omega}}^b_{b/o} + \boldsymbol{\omega}^b_{b/o} \times \mathbf{I}'_{ai}\boldsymbol{\omega}^b_{b/o}) \tag{3.45}$$

3.7.5 Brake actuation dynamics

Relationship between model inputs and brake deflection

The normalized/relative left and right brake deflection $\bar{\delta}_l$ and $\bar{\delta}_r$ can be calculated by dividing the total deflection (the physical shortening of the brake line) of a given side by the maximum deflection Δ_{max}.

$$\bar{\delta} \triangleq \frac{\Delta_{brake}}{\Delta_{max}} \tag{3.46}$$

The model inputs δ_s and δ_a are defined as a function of these normalized values.

$$\delta_a \triangleq \bar{\delta}_r - \bar{\delta}_l \tag{3.47}$$

$$\delta_s \triangleq \min(\bar{\delta}_l, \bar{\delta}_r) \tag{3.48}$$

The given definitions result in the following constraints on $\bar{\delta}$ and δ:

$$0 \leq \bar{\delta} \leq 1 \tag{3.49a}$$

$$0 \leq \delta_s \leq 1 \tag{3.49b}$$

$$-1 \leq \delta_a \leq 1 \tag{3.49c}$$

$$\delta_s \leq 1 - |\delta_a| \tag{3.49d}$$

Finally, the inverse relationship can also be derived to translate model inputs into normalized brake deflection:

$$\bar{\delta}_r = \begin{cases} \delta_s + \delta_a & if\ \delta_a > 0 \\ \delta_s & if\ \delta_a \leq 0 \end{cases} \qquad \bar{\delta}_l = \begin{cases} \delta_s & if\ \delta_a \geq 0 \\ \delta_s - \delta_a & if\ \delta_a < 0 \end{cases} \tag{3.50}$$

Actuator dynamics

To represent the dynamics of a servomotor as is typically used for brake actuation, the brake position is modeled as a rate-limited first order system:

$$\dot{\bar{\delta}} = (\bar{\delta}_{des} - \bar{\delta})/T_\delta, \quad |\dot{\bar{\delta}}| \leq \dot{\bar{\delta}}_{max} \tag{3.51}$$

Figure 3.5 shows the Simulink implementation of the brake dynamics. δ_a and δ_s setpoints are converted to brake deflection setpoints, and brake dynamics are applied. The resulting actual brake positions are converted back to actual δ_a and δ_s values, which are then used as model inputs. The implementation shown also detects when the δ_s input is saturated, defined as when the given setpoint is outside the range of valid values resulting from the constraints in Equations 3.49c and 3.49d.

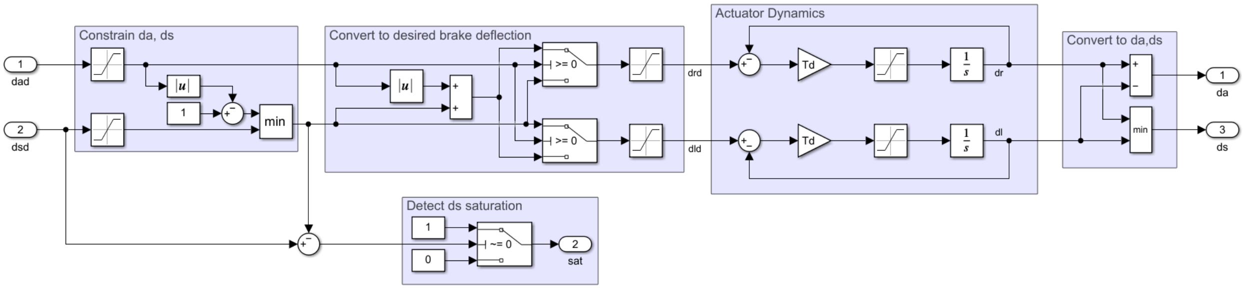

Figure 3.5 Simulink implementation of the actuator dynamics

3.8 Full nonlinear model of the system

The kinematic and dynamic equations obtained (Eqs. 3.15, 3.17, 3.21, 3.26), as well as the force and moment equations (Eqs. 3.29, 3.33, 3.34, 3.44, 3.45), allow us to build the full nonlinear model of the parafoil and payload system. The full system of equations is represented as a state-space model:

$$\dot{\mathbf{x}} = \mathbf{f}(\mathbf{x}, \mathbf{u}) \tag{3.52a}$$

$$\mathbf{y} = \mathbf{g}(\mathbf{x}, \mathbf{u}) \tag{3.52b}$$

where $\mathbf{x}$, $\mathbf{y}$, and $\mathbf{u}$ are vectors representing the state, output and input variables, and $\mathbf{f}$ and $\mathbf{g}$ are nonlinear functions. The state and input vectors, as detailed previously, are as follows:

$$\mathbf{x} = \begin{bmatrix} u & v & w & p & q & r & \phi & \theta & \psi & p_N & p_E & p_D \end{bmatrix}^\top \tag{3.53}$$

$$\mathbf{u} = \begin{bmatrix} \delta_a & \delta_s \end{bmatrix}^\top \tag{3.54}$$

The output vector, meanwhile, represents the data obtained through GPS, altimeter, and IMU measurements, and is thus composed of position and velocity and Euler angles:

$$\mathbf{y} = \begin{bmatrix} p_N & p_E & p_D & \dot{p}_N & \dot{p}_E & \dot{p}_D & \phi & \theta & \psi \end{bmatrix}^\top \tag{3.55}$$

3.9 Validation and analysis of the 6-DOF model

Having established the mathematical basis for the dynamics of the parafoil system, this section presents an analysis of the behavior of the 6-DOF model using data collected from numerical simulations. All simulations were performed without the inclusion of actuator dynamics.

This analysis has the following objectives:

- Observe and quantify the general behavior of the system in reaction to control inputs and variations in atmospheric conditions.
- Provide a basis to justify the simplifying assumptions used by the 4-DOF model presented later in Section 3.10.
- Validate the implementation of the model through comparison with data provided in the literature.

Firstly, the Simulink model and the parameters used for simulation are presented. This is followed by an analysis of the transient and steady-state response to control inputs. Next, the effect of altitude and air density on system behavior is studied. We conclude the linearization of the full model about a steady-state operating point, and an analysis of the dynamic modes of the system.

3.9.1 Simulink implementation

Simulations using the model were performed using Simulink. Figure 3.6 shows the Simulink model implementing the 6-DOF model dynamics. Further detail on the custom blocks contained within the model can be found in Appendix B.

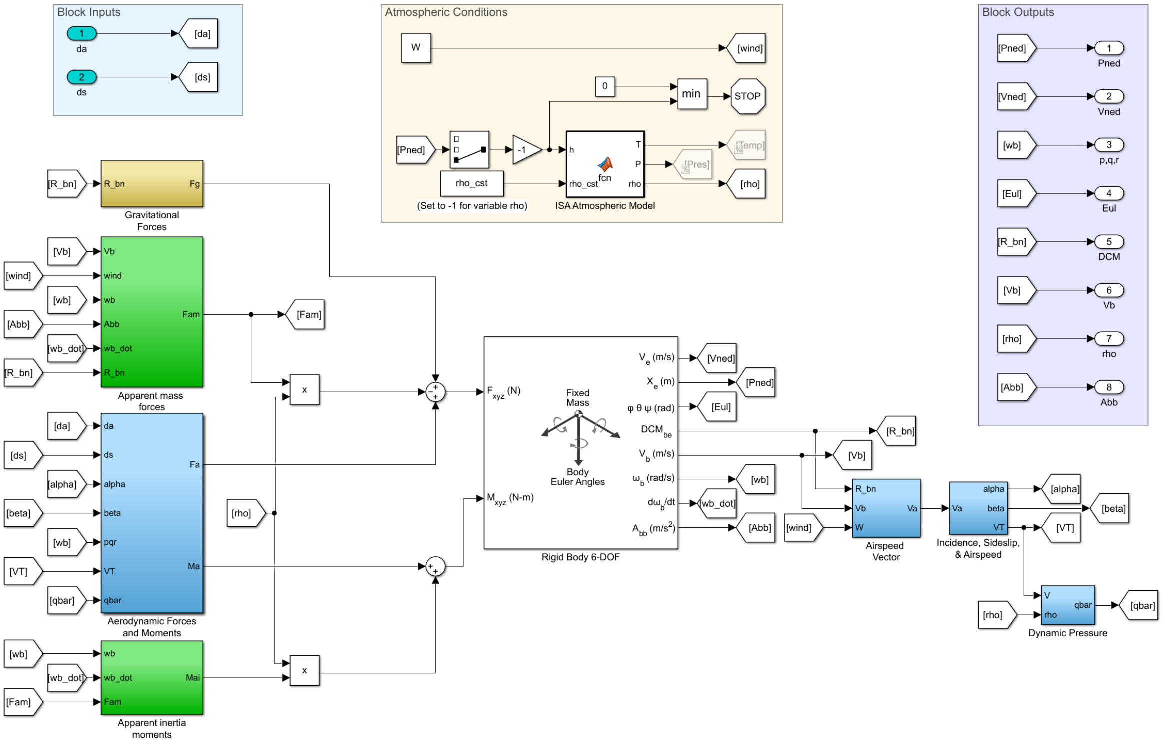

Figure 3.6 Simulink Implementation of the 6-DOF model

The implementation features δ_a and δ_s as block inputs, and the block outputs include the formal outputs $\mathbf{p}^o$, $\dot{\mathbf{p}}^o$ and $\mathbf{\Phi}$ as well as additional outputs which were used for debugging and development purposes. For air density, the model implementation supports both a constant ρ (for linearization and steady-state simulations) or the value calculated from the ISA model and current altitude. The simulation is automatically halted when the vehicle reaches an altitude of 0 m.

3.9.2 Model parameters

Tables 3.3 and 3.4 present the parameters and coefficients used for the simulations in this section, assembled from [27] and [45], which model the Snowflake precision aerial delivery system.

Parameter	Description	Value	Unit
m	System Mass	2.4	kg
b	Canopy Span	1.35	m
c	Canopy Chord	0.75	m
t	Canopy Thickness	0.075	m
S	Canopy Surface Area	1	m^2
μ	Rigging Angle	-12	deg
$\mathbf{I}$	Inertia Matrix	$\begin{bmatrix} 0.42 & 0 & 0.03 \\ 0 & 0.40 & 0 \\ 0.03 & 0 & 0.053 \end{bmatrix}$	$\mathrm{kg} \cdot \mathrm{m}^2$
$\mathbf{I_{am}}$	Apparent Mass Matrix	$\begin{bmatrix} 0.012 & 0 & 0 \\ 0 & 0.032 & 0 \\ 0 & 0 & 0.42 \end{bmatrix}$	m^3
$\mathbf{I_{ai}}$	Apparent Inertia Matrix	$\begin{bmatrix} 0.054 & 0 & 0 \\ 0 & 0.14 & 0 \\ 0 & 0 & 0.0024 \end{bmatrix}$	m^5
$\mathbf{r_{BP}}$	Vector from CM to Apparent CM	$\begin{bmatrix} 0.046 & 0 & -1.11 \end{bmatrix}^\top$	m

Table 3.3 Model parameters used in the 6-DOF simulation

Coefficient	Description	Parameters
C_D	Drag	$C_{D0} = 0.15$, $C_{D\alpha^2} = 0.9$, $C_{D\delta s} = 0.25$
C_Y	Side force	$C_{Y\beta} = -0.35$
C_L	Lift	$C_{L0} = 0.25$, $C_{L\alpha} = 0.68$, $C_{L\delta s} = 0.25$
C_l	Rolling	$C_{l\beta} = -0.09$, $C_{lp} = -0.4$, $C_{lr} = -0.005$, $C_{l\delta a} = -0.0005$
C_m	Pitching	$C_{m0} = 0.2275$, $C_{m\alpha} = -0.648$, $C_{mq} = -1.192$
C_n	Yawing	$C_{n\beta} = 0.015$, $C_{np} = -0.0388$, $C_{nr} = -0.02$, $C_{n\delta a} = 0.0006$

Table 3.4 Aerodynamic coefficients used in the 6-DOF simulation

3.9.3 Step response

We first consider the system responses to an individual step input in asymmetric and symmetric deflection, starting from a steady glide at an altitude of 500 m (Figs 3.7 and 3.8).

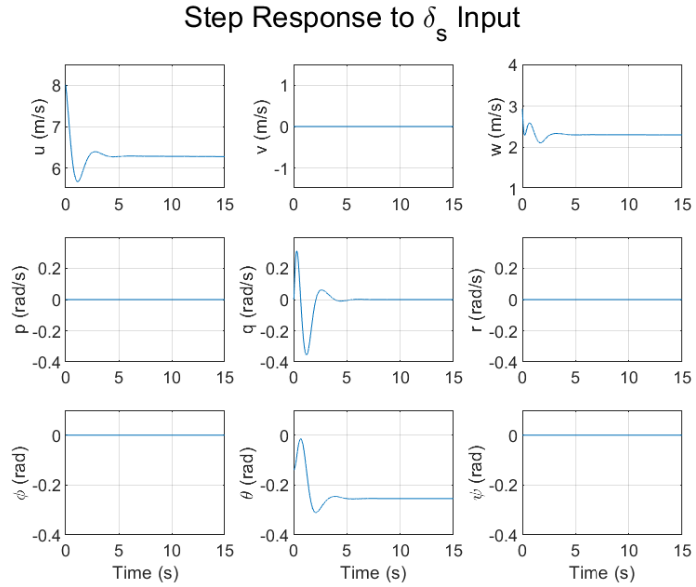

Figure 3.7 Symmetric deflection

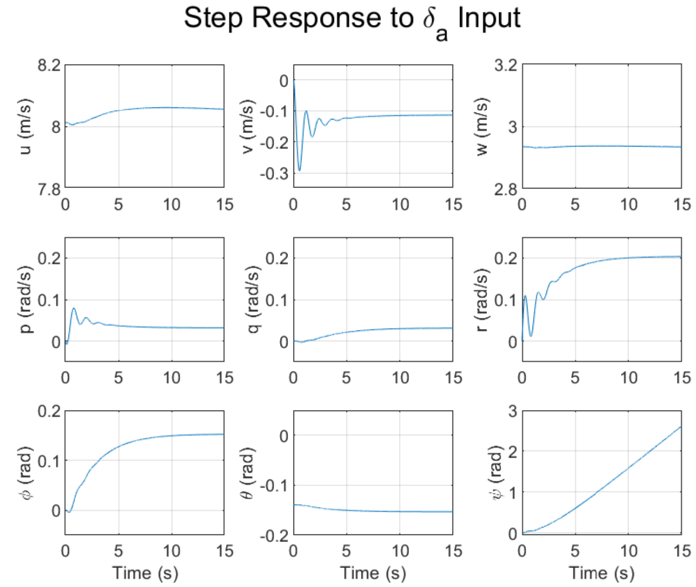

Figure 3.8 Asymmetric deflection

The transient response for the system states is consistently under 10 seconds, for both inputs. From the δ_s step response (Fig. 3.7), it can be seen that the vehicle initially pitches up before settling at a lower pitch angle, which is consistent with the known flaring behavior of parafoil systems. When timed correctly, this can be used to shed forward velocity just before landing. In the δ_a step response (Fig. 3.8), the evolution of the roll angle closely resembles the response of a first order system, and the yaw angle settles into a constant yaw rate around the time the roll angle reaches a steady state.

The two responses show a general decoupling between longitudinal inputs and lateral response, and vice versa, when considering individual inputs, i.e., using only symmetric or only asymmetric deflection. Symmetric deflection has no effect on v, p, r, ϕ, and ψ, while asymmetric deflection has a limited impact on u, w, q and θ. However, when considering combined inputs, the presence of symmetric deflection affects the asymmetric step response, as shown in figure 3.9.

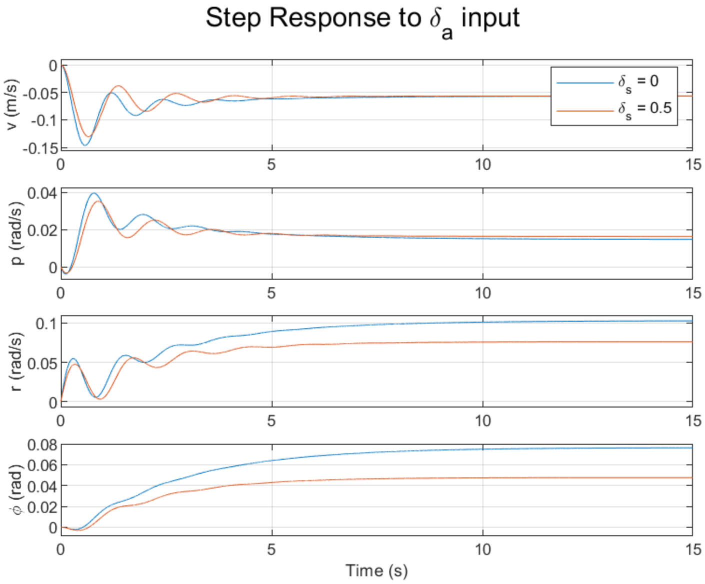

Figure 3.9 Effect of δ_s on asymmetric step response

Symmetric deflection increases lift and drag and consequently reduces the total airspeed. This results in a decreased lateral responsiveness, since the aerodynamic forces and moments are proportional to dynamic pressure and thus V_T^2 (Eqs. 3.33 and 3.34). There is a negligible effect on the responses of v and p, but this significantly affects both the transient and steady-state response of the roll angle and yaw rate. Both the steady-state value and settling time are reduced with an increase in symmetric deflection and the resulting reduction in airspeed.

3.9.4 Steady-state response to control inputs

We now present an analysis of the steady-state response of the 6-DOF parafoil model over the range of possible symmetric and asymmetric input values. It should be noted that in practice, the inherent downwards velocity of the parafoil system means that a steady-state velocity is never reached, due to the continuous variation of air density that results from the loss of altitude. For this reason, all simulations were performed with a constant air density $\rho = 1.17$ kg/m^3, corresponding to a flight altitude of 500 m. In the case of asymmetric deflection, steady-state is determined using yaw rate rather than yaw angle.

Asymmetric deflection

Figure 3.10 shows the steady turn response over the range of possible values of $\delta_a \in [-1, 1]$, for $\delta_s = 0$. The results highlight a linear relationship from asymmetric deflection to turn rate and roll angle, while the effect on pitch angle, linear velocities, and glide ratio is negligible. The maximum body-frame lateral velocity v induced by a turn is approximately 0.11 m/s, which with the corresponding total airspeed $V_T = 8.6$ m/s results in a sideslip angle β of less than 1°.

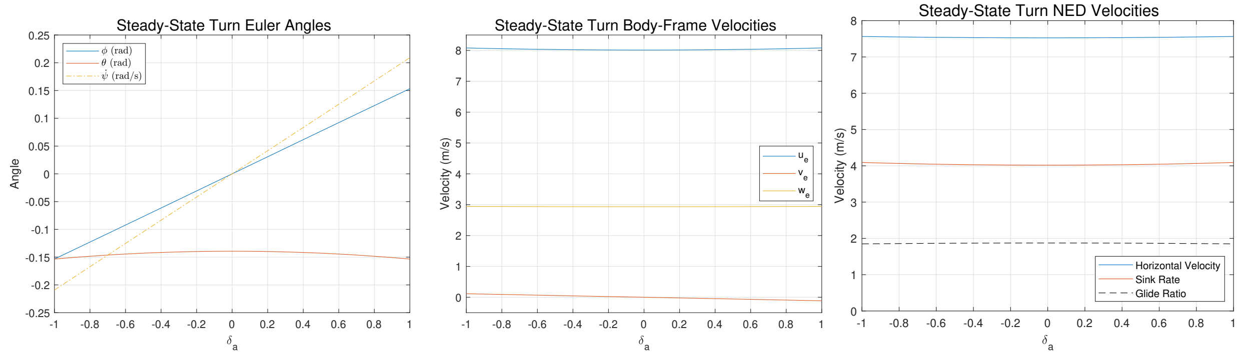

(a) Euler Angles and turn rate **(b)** Body-frame velocities **(c)** NED velocities and glide ratio

Figure 3.10 Steady-state response to asymmetric deflection

Symmetric deflection

Figure 3.11 shows the steady-state longitudinal response of the system given a constant symmetric input $\delta_s \in [0, 1]$, for $\delta_a = 0$. During a steady glide with no control inputs, the system maintains a pitch angle of approximately 8°, with a total airspeed of 8.53 m/s and a glide ratio of 1.9. An increase in δ_s results in the vehicle equilibrium pitching forward (Fig. 3.11c), and a decrease in both total airspeed and glide ratio (Fig. 3.11b), . Since the ratio of forward to vertical velocity in the body frame remains constant at $u/w = 2.73$ (Fig. 3.11a), the reduction in glide ratio is caused entirely by the changing pitch angle of the vehicle.

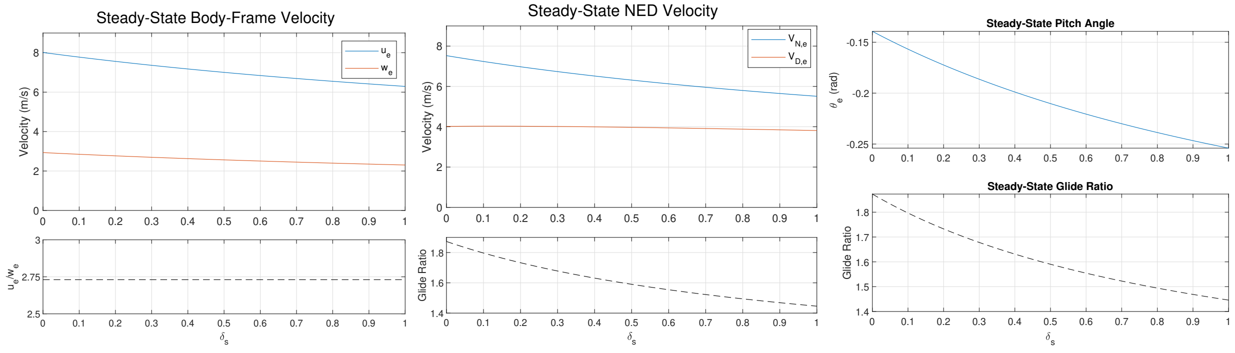

(a) Body-frame velocities **(b)** NED velocities and glide ratio **(c)** Pitch angle

Figure 3.11 Steady-state response to symmetric deflection

Combined deflection

As pointed out in Section 3.9.3, the effect of δ_a on the lateral behavior of the system is influenced by the δ_s input. Hence, it is of interest to study the system's steady-state response to combined symmetrical and asymmetrical inputs. Specifically, we consider here the evolution of the steady-state roll angle and side velocity for the full range of combined inputs. The result is a triangular surface, a consequence of equation 3.49d limiting the range of δ_a for a given δ_s.

In figure 3.12, we can see that increasing δ_s reduces the steady-state roll angle for a given δ_a, with the effect being more pronounced for higher values of δ_a. For example, when $\delta_s = 0$, an asymmetric deflection $\delta_s = 0.5$ results in a roll angle of 0.1 rad. When $\delta_s = 0.3$, to achieve the same roll angle the asymmetric input needs to be increased to $\delta_a = 0.7$. As mentioned previously, this is mainly due to the reduction in total airspeed caused by symmetrically engaging the brakes.

Lateral velocity, however, is not influenced by δ_s, whether considering individual or combined inputs. As seen in figure 3.13, v remains constant for a given δ_a even as δ_s increases. While this is accompanied by an increase in sideslip angle as the total airspeed decreases, the effect is minimal, and the maximum sideslip angle of $\beta = 0.7°$ is achieved with $\delta_s = 0$, $\delta_a = 1$ and $v = 0.11$ m/s.

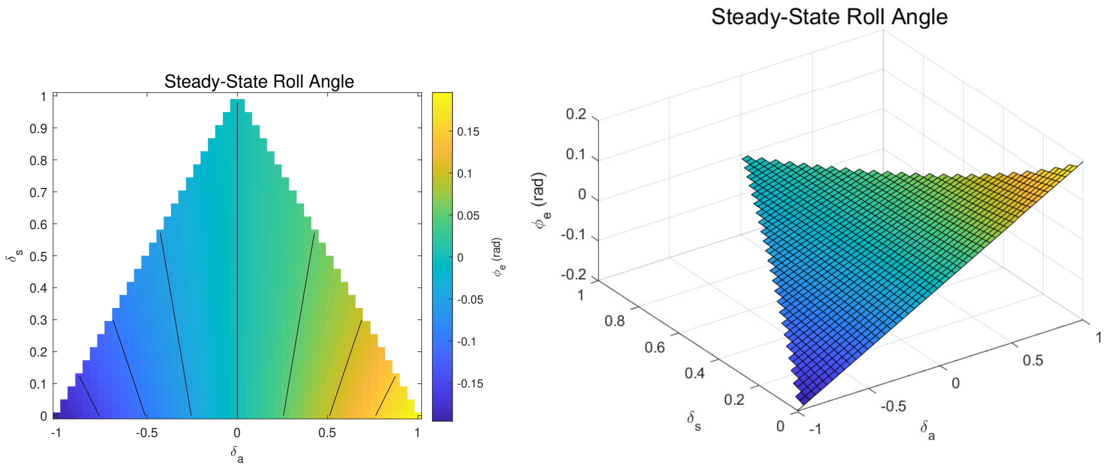

Figure 3.12 Steady-state roll angle for combined inputs

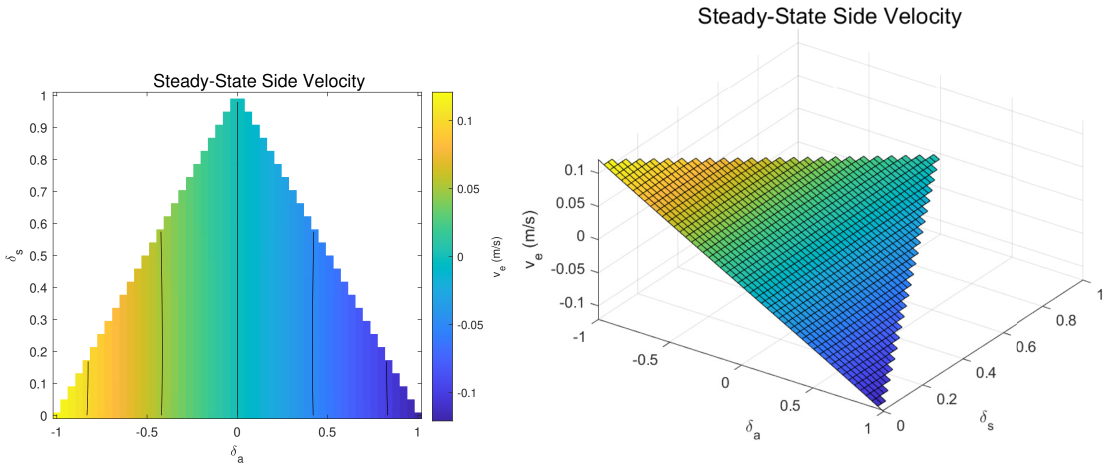

Figure 3.13 Steady-state lateral velocity for combined inputs

3.9.5 Linearized model

Stability analysis, and extraction of the lateral and longitudinal dynamic modes, require a linear approximation of the parafoil system. Therefore, given the nonlinear state equations

$$\dot{\mathbf{x}} = \mathbf{f}(\mathbf{x}, \mathbf{u}) \tag{3.56a}$$

$$\mathbf{y} = \mathbf{g}(\mathbf{x}, \mathbf{u}) \tag{3.56b}$$

the system must be linearized around a point of equilibrium to obtain the linear system

$$\boldsymbol{\Delta}\dot{\mathbf{x}} = \mathbf{A}\boldsymbol{\Delta}\mathbf{x} + \mathbf{B}\boldsymbol{\Delta}\mathbf{u} \tag{3.57a}$$

$$\boldsymbol{\Delta}\dot{\mathbf{y}} = \mathbf{C}\boldsymbol{\Delta}\mathbf{x} + \mathbf{D}\boldsymbol{\Delta}\mathbf{u} \tag{3.57b}$$

The linearized system will be a valid approximation of the parafoil for small variations $\mathbf{\Delta x}$ and $\mathbf{\Delta u}$ around a given equilibrium. This equilibrium can be found by solving the state equation with the left hand side set to zero:

$$\mathbf{0} = \mathbf{f}(\mathbf{x}_e, \mathbf{u}_e) \tag{3.58a}$$

$$\mathbf{y}_e = \mathbf{g}(\mathbf{x}_e, \mathbf{u}_e) \tag{3.58b}$$

The state and output equations are then linearized using a first order Taylor expansion about the equilibrium:

$$\dot{\mathbf{x}} = \frac{\mathrm{d}}{\mathrm{d}t}(\mathbf{x}_e + \mathbf{\Delta x}) = \mathbf{\Delta}\dot{\mathbf{x}} \tag{3.59a}$$

$$\mathbf{f}(\mathbf{x}, \mathbf{u}) = \mathbf{f}(\mathbf{x}_\mathbf{e} + \mathbf{\Delta x}, \mathbf{u}_e + \mathbf{\Delta u}) \tag{3.59b}$$

$$\approx \underbrace{\mathbf{f}(\mathbf{x}_e, \mathbf{u}_e)}_{=0} + \left.\frac{\partial \mathbf{f}}{\partial \mathbf{x}}\right|_{\mathbf{x}_e, \mathbf{u}_e} \mathbf{\Delta x} + \left.\frac{\partial \mathbf{f}}{\partial \mathbf{u}}\right|_{\mathbf{x}_e, \mathbf{u}_e} \mathbf{\Delta u} \tag{3.59c}$$

$$\mathbf{\Delta y} = \mathbf{y}_e + \mathbf{\Delta y} \tag{3.60a}$$

$$\mathbf{g}(\mathbf{x}, \mathbf{u}) = \mathbf{g}(\mathbf{x}_\mathbf{e} + \mathbf{\Delta x}, \mathbf{u}_e + \mathbf{\Delta u}) \tag{3.60b}$$

$$\approx \underbrace{\mathbf{g}(\mathbf{x}_e, \mathbf{u}_e)}_{=\mathbf{y_e}} + \left.\frac{\partial \mathbf{g}}{\partial \mathbf{x}}\right|_{\mathbf{x}_e, \mathbf{u}_e} \mathbf{\Delta x} + \left.\frac{\partial \mathbf{g}}{\partial \mathbf{u}}\right|_{\mathbf{x}_e, \mathbf{u}_e} \mathbf{\Delta u} \tag{3.60c}$$

Given a system with n states, m inputs and p outputs, the definitions for the **A**, **B**, **C** and **D** matrices are thus:

$$A \triangleq \left.\frac{\partial \mathbf{f}}{\partial \mathbf{x}}\right|_{\mathbf{x}_e, \mathbf{u}_e} = \begin{bmatrix} \frac{\partial f_1}{\partial x_1} & \cdots & \frac{\partial f_1}{\partial x_n} \\ \vdots & \ddots & \vdots \\ \frac{\partial f_n}{\partial x_1} & \cdots & \frac{\partial f_n}{\partial x_n} \end{bmatrix}, \quad B \triangleq \left.\frac{\partial \mathbf{f}}{\partial \mathbf{u}}\right|_{\mathbf{x}_e, \mathbf{u}_e} = \begin{bmatrix} \frac{\partial f_1}{\partial u_1} & \cdots & \frac{\partial f_1}{\partial u_m} \\ \vdots & \ddots & \vdots \\ \frac{\partial f_n}{\partial u_1} & \cdots & \frac{\partial f_n}{\partial u_m} \end{bmatrix} \tag{3.61a}$$

$$C \triangleq \left.\frac{\partial \mathbf{g}}{\partial \mathbf{x}}\right|_{\mathbf{x}_e, \mathbf{u}_e} = \begin{bmatrix} \frac{\partial g_1}{\partial x_1} & \cdots & \frac{\partial g_1}{\partial x_n} \\ \vdots & \ddots & \vdots \\ \frac{\partial g_p}{\partial x_1} & \cdots & \frac{\partial g_p}{\partial x_n} \end{bmatrix}, \quad D \triangleq \left.\frac{\partial \mathbf{g}}{\partial \mathbf{u}}\right|_{\mathbf{x}_e, \mathbf{u}_e} = \begin{bmatrix} \frac{\partial g_1}{\partial u_1} & \cdots & \frac{\partial g_1}{\partial u_m} \\ \vdots & \ddots & \vdots \\ \frac{\partial g_p}{\partial u_1} & \cdots & \frac{\partial g_p}{\partial u_m} \end{bmatrix} \tag{3.61b}$$

Linearized state equation

The chosen equilibrium is a steady glide with no control inputs at 500 m ($\rho = 1.17$). All state derivatives are zero, with the exception of NED positions which are omitted in the linearized model:

$$\dot{u} = \dot{v} = \dot{w} = \dot{p} = \dot{q} = \dot{r} = \dot{\phi} = \dot{\theta} = \dot{\psi} = 0 \tag{3.62}$$

The resulting equilibrium values are:

$$\begin{bmatrix} \delta_{a,e} \\ \delta_{s,e} \end{bmatrix} = \begin{bmatrix} 0 \\ 0 \end{bmatrix}, \quad \begin{bmatrix} u_e \\ v_e \\ w_E \end{bmatrix} = \begin{bmatrix} 8.01 \\ 0 \\ 2.93 \end{bmatrix} \text{m/s}, \quad \begin{bmatrix} p_e \\ q_e \\ r_e \end{bmatrix} = \begin{bmatrix} 0 \\ 0 \\ 0 \end{bmatrix} \text{rad/s}, \quad \begin{bmatrix} \phi_e \\ \theta_e \\ \psi_e \end{bmatrix} = \begin{bmatrix} 0 \\ -0.139 \\ 0 \end{bmatrix} \text{rad} \tag{3.63}$$

Because the output variables are simply a subset of the system state, only the state equation was linearized. Linearization about this equilibrium was performed using MATLAB's `linmod` function, resulting in the matrices:

$$\mathbf{A} = \begin{bmatrix} -0.435 & 0 & 0.259 & 0 & -2.934 & 0 & 0 & -9.715 & 0 \\ 0 & -0.726 & 0 & 2.934 & 0 & -8.012 & 9.715 & 0 & 0 \\ -1.473 & 0 & -2.601 & 0 & 8.012 & 0 & 0 & 1.362 & 0 \\ 0 & -1.643 & 0 & -4.258 & 0 & 0.071 & 0 & 0 & 0 \\ 2.081 & 0 & -5.682 & 0 & -4.174 & 0 & 0 & 0 & 0 \\ 0 & 2.833 & 0 & -0.908 & 0 & -1.753 & 0 & 0 & 0 \\ 0 & 0 & 0 & 1.000 & 0 & -0.140 & 0 & 0 & 0 \\ 0 & 0 & 0 & 0 & 1.000 & 0 & 0 & 0 & 0 \\ 0 & 0 & 0 & 0 & 0 & 1.010 & 0 & 0 & 0 \end{bmatrix} \tag{3.64}$$

$$\mathbf{B} = \begin{bmatrix} 0 & 0 & 0 & -0.120 & 0 & 0.717 & 0 & 0 & 0 \\ -2.634 & 0 & -5.679 & 0 & 0 & 0 & 0 & 0 & 0 \end{bmatrix}^{\top} \tag{3.65}$$

Having obtained the full linearized state equation, it is then separated into the linearized longitudinal and lateral dynamics.

Linearized longitudinal dynamics

The longitudinal model is composed of forward and vertical velocity, resp. Δu and Δw, pitch rate Δq and pitch angle $\Delta\theta$. Longitudinal dynamics are only affected by the symmetric input.

$$\begin{bmatrix} \Delta\dot{u} \\ \Delta\dot{w} \\ \Delta\dot{q} \\ \Delta\dot{\theta} \end{bmatrix} = \underbrace{\begin{bmatrix} -0.435 & 0.259 & -2.934 & -9.715 \\ -1.473 & -2.601 & 8.012 & 1.362 \\ 2.081 & -5.682 & -4.174 & 0 \\ 0 & 0 & 1 & 0 \end{bmatrix}}_{\mathbf{A}_{\mathbf{lon}}} \underbrace{\begin{bmatrix} \Delta u \\ \Delta w \\ \Delta q \\ \Delta \theta \end{bmatrix}}_{\mathbf{x}_{\mathbf{lon}}} + \underbrace{\begin{bmatrix} -2.634 \\ -5.679 \\ 0 \\ 0 \end{bmatrix}}_{\mathbf{B}_{\mathbf{lon}}} \Delta\delta_s \tag{3.66}$$

Linearized lateral dynamics

The lateral dynamics include side velocity Δv, roll rate Δp, yaw rate Δr and roll angle $\Delta\phi$. In the linearized system, only asymmetric deflection affects the lateral dynamics.

$$\begin{bmatrix} \Delta\dot{v} \\ \Delta\dot{p} \\ \Delta\dot{r} \\ \Delta\dot{\phi} \end{bmatrix} = \underbrace{\begin{bmatrix} -0.726 & 2.934 & -8.012 & 9.715 \\ -1.643 & -4.258 & 0.071 & 0 \\ 2.833 & -0.908 & -1.753 & 0 \\ 0 & 1 & -0.140 & 0 \end{bmatrix}}_{\mathbf{A}_{\mathbf{lat}}} \underbrace{\begin{bmatrix} \Delta v \\ \Delta p \\ \Delta r \\ \Delta \phi \end{bmatrix}}_{\mathbf{x}_{\mathbf{lat}}} + \underbrace{\begin{bmatrix} 0 \\ -0.120 \\ 0.717 \\ 0 \end{bmatrix}}_{\mathbf{B}_{\mathbf{lat}}} \Delta\delta_a \tag{3.67}$$

3.9.6 Stability analysis

Figure 3.14 illustrates the lateral and longitudinal modes of the 6-DOF model, obtained from the matrices $\mathbf{A}_{\mathbf{lat}}$ and $\mathbf{A}_{\mathbf{lon}}$.

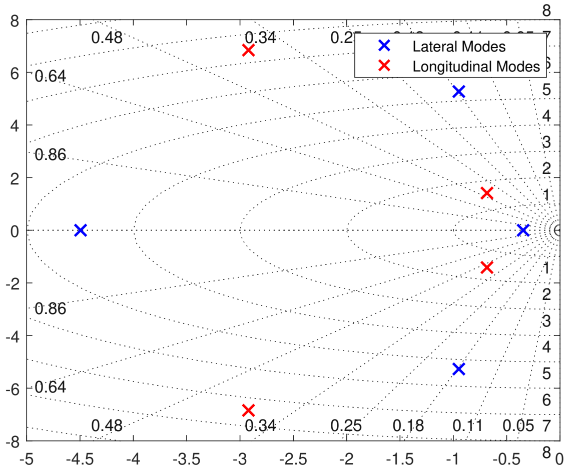

Figure 3.14 Dynamic modes of the linearized 6-DOF model

The modes found are coherent with those found in typical flight dynamics, with phugoid and short-period visible in the longitudinal model, and spiral, pure roll, and Dutch roll found in the lateral model. It should be noted that the spiral mode of the parafoil is stable, whereas this mode is usually slightly unstable for most aircraft. This is attributed to the self-stabilizing effect of the payload mass acting as a pendulum below the canopy.

Tables 3.5 and 3.6 show the characteristics of identified lateral and longitudinal modes along with those found in [45] for a 6-DOF model of the Snowflake PADS. Figure 3.15 shows this same comparison graphically with the poles plotted on the complex plane.

	Literature		**Linearized Model**	
Mode	**Eigenvalues**	**Damping**	**Eigenvalues**	**Damping**
Short Period	$-2.65 \pm 6.95i$	0.36	$-2.92 \pm 6.84i$	0.39
Phugoid	$-0.59 \pm 1.12i$	0.47	$-0.68 \pm 1.41i$	0.44

Table 3.5 Longitudinal Dynamic Modes

	Literature		**Linearized Model**	
Mode	**Eigenvalues**	**Damping**	**Eigenvalues**	**Damping**
Spiral	-0.38	–	-0.35	–
Roll Subsidence	-4.49	–	-4.49	–
Dutch Roll	$-0.97 \pm 5.65i$	0.17	$-0.95 \pm 5.27i$	0.18

Table 3.6 Lateral Dynamic Modes

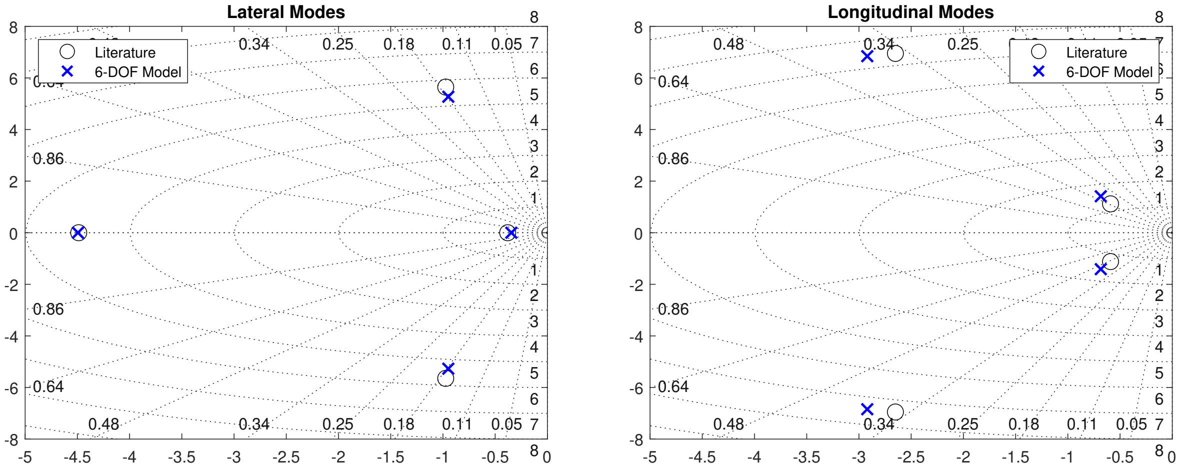

(a) Lateral Modes

(b) Longitudinal Modes

Figure 3.15 Modal Comparison to the Literature

The identified modes are found to be coherent with those available in the literature, with slight discrepancies attributed to minor differences in parameters obtained during system identification, as the model coefficients and dynamic modes were obtained from different papers describing the same system.

3.9.7 Effect of altitude and variable air density

Taking into account the variation in air density brought about by a change in altitude brings out interesting features in the longitudinal and lateral behavior of the system. This can be seen in both the evolution of the dynamic modes and the response to constant inputs over the duration of a flight.

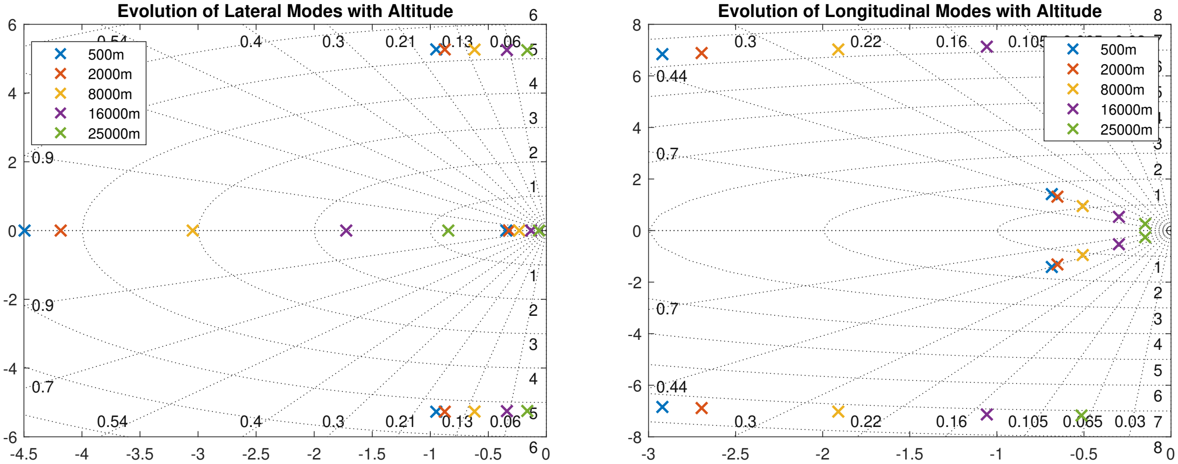

(a) Lateral Modes **(b)** Longitudinal Modes

Figure 3.16 Evolution of system stability with altitude

As seen in Figure 3.16a, notable changes in lateral stability occur as altitude increases. While the spiral mode remains mostly unaffected, roll response becomes slower with the gradual displacement towards the imaginary axis of the roll subsidence mode. The Dutch roll response becomes progressively less damped at higher altitudes, as the system inertia gradually overtakes the stabilizing aerodynamic forces acting on the system, the magnitude of which is reduced with the decrease in air density. A similar effect can be noticed in the evolution of longitudinal stability (Fig 3.16b), where the short-period mode also shows progressively diminishing damping. The phugoid mode maintains a consistent damping ratio, but the response becomes slower as altitude increases, similar to the roll subsidence mode.

Figure 3.17a illustrates the gradual reduction in steady-state velocity (both vertical and horizontal) as air density and its resulting forces increase. Since lift and drag are both directly proportional to air density, the glide ratio is maintained throughout the flight. Figure 3.17b shows the evolution of the effect of asymmetric deflection over varying altitudes. As altitude decreases and air density increases, the total airspeed decreases, and both the roll angle and turn rate decrease in amplitude. As such, the increased system stability brought about by lower altitudes is accompanied by a general decrease in the system's lateral responsiveness.

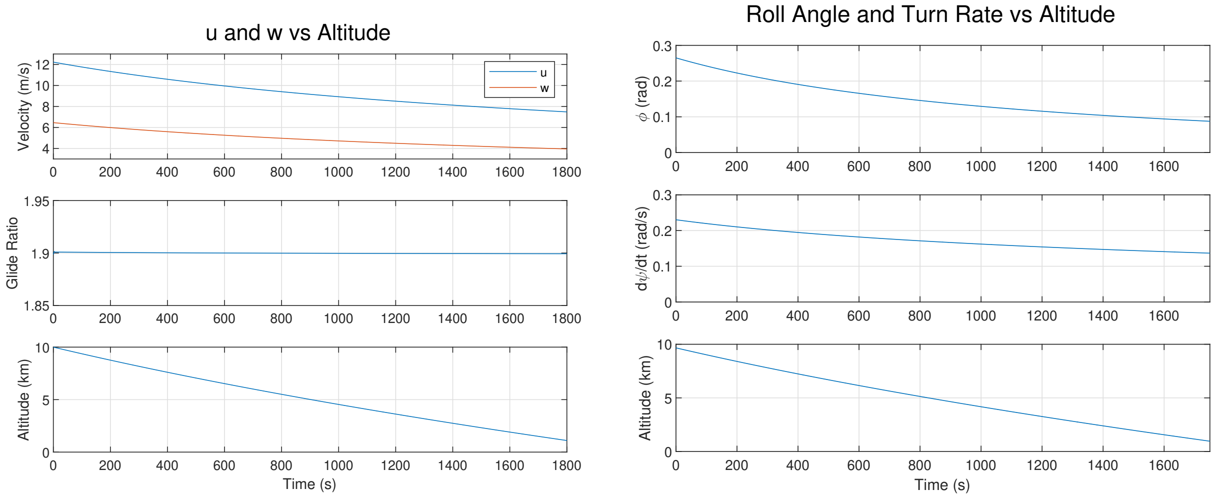

(a) Longitudinal evolution, no inputs

(b) Lateral evolution, $\delta_a = 0.25$

Figure 3.17 Evolution of lateral and longitudinal equilibria with altitude

3.10 Simplified 4-DOF model

An important aspect to consider when using a dynamic model is the procedure and computational complexity of determining the numerical values of the various system parameters and coefficients present in the model. Certain parameters can be directly determined from physical measurements of the system, without the need for flight data. These include the canopy geometry and the system mass. Other parameters are more challenging, and impractical, to determine analytically or numerically without flight tests: notably the inertia matrix, apparent mass matrices, and aerodynamic coefficients. Instead, we must collect flight data from a sufficient number of carefully chosen maneuvers and make use of system identification algorithms to extract the relevant parameters. In the 6-DOF Model, 29 of these parameters need to be identified through system identification methods. In contrast, a 4-DOF model requires identification of only 6 parameters.

The main element of interest when performing modeling and control of the parafoil system is its trajectory: we seek to control glide ratio (in a limited manner) and heading to allow the vehicle to follow a desired trajectory. As such, it is not always necessary to accurately model all of the specific internal states of the model if they can be approximated well enough that a controller designed using a simplified model gives adequate performance. With fewer system states and parameters present in the model, the computational load of the identification algorithm, the required number of identification maneuvers, the required instrumentation, and the complexity of the control law can all be reduced. Furthermore, reducing the processing load for identification allows for the possibility of performing these calculations directly onboard the flight computer. With the ability to perform these computations during flight, it also becomes possible to periodically update the identified parameters throughout the mission as new data is collected.

For these reasons, it becomes relevant to consider a lower fidelity model and evaluate its effectiveness when used to design control laws for the system. We therefore now detail a second, 4-DOF model, obtained by applying additional simplifying assumptions to the previously defined 6-DOF model.

3.10.1 Simplifying assumptions

Three additional hypotheses are made concerning the kinematics of the system :

ASM–K1. Pitching is neglected ($\theta = \dot{\theta} = 0$)

ASM–K2. The system has no lateral aerodynamic velocity ($v_a = \dot{v}_a = 0$)

ASM–K3. Sideslip is neglected ($\beta = 0$)

Five other assumptions concern system dynamics :

ASM–D3. Aerodynamic side-force is neglected. ($Y = 0$)

ASM–D4. Lift and drag coefficients are linearly dependent on symmetric brake deflection.

ASM–D5. Aerodynamic forces are independent of the angle of attack.

ASM–D6. The relationship between asymmetric brake deflection on roll angle can be modeled as a first-order transfer function.

ASM–D7. Aerodynamic moments are implicitly handled by the roll angle model.

3.10.2 Resulting model

By first applying assumption K1 to equation 3.16, we obtain the new relationship between angular rates $\boldsymbol{\omega}^b$ and Euler rates $\dot{\boldsymbol{\Phi}}$:

$$\begin{bmatrix} p \\ q \\ r \end{bmatrix} = \begin{bmatrix} 1 & 0 & 0 \\ 0 & \cos\phi & \sin\phi \\ 0 & -\sin\phi & \cos\phi \end{bmatrix} \begin{bmatrix} \dot{\phi} \\ 0 \\ \dot{\psi} \end{bmatrix} \tag{3.68}$$

$$\begin{bmatrix} p \\ q \\ r \end{bmatrix} = \begin{bmatrix} \dot{\phi} \\ \dot{\psi}\sin\phi \\ \dot{\psi}\cos\phi \end{bmatrix} \tag{3.69}$$

Applying K1 and K2 to equation (3.15), we obtain the NED position kinematics

$$\begin{bmatrix} v_n \\ v_e \\ v_d \end{bmatrix} = \begin{bmatrix} \cos\psi & -\cos\phi\sin\psi & \sin\phi\sin\psi \\ \sin\psi & \cos\phi\cos\psi & -\sin\phi\cos\psi \\ 0 & \sin\phi & \cos\phi \end{bmatrix} \begin{bmatrix} u \\ 0 \\ w \end{bmatrix} \tag{3.70}$$

Next, we can determine the new gravitational force vector, from equation (3.29)

$$\mathbf{F}_g^b = mg_0 \begin{bmatrix} 0 \\ \sin\phi \\ \cos\phi \end{bmatrix} \tag{3.71}$$

Aerodynamic drag and lift forces are modeled following assumptions D4 and D5

$$D = \frac{1}{2}\rho V_T^2 S \left(C_{D0} + C_{D\delta s}\delta_s\right) \tag{3.72}$$

$$L = \frac{1}{2}\rho V_T^2 S \left(C_{L0} + C_{L\delta s}\delta_s\right) \tag{3.73}$$

where, due to assumption K2, equation 3.31b becomes

$$V_T = \sqrt{u_a^2 + w_a^2} \tag{3.74}$$

The full aerodynamic force vector, taking into account assumption D3, is then once again projected into the body frame:

$$\mathbf{F}_a^b = \begin{bmatrix} X_a \\ Y_a \\ Z_a \end{bmatrix} = \begin{bmatrix} L\sin\alpha - D\cos\alpha \\ 0 \\ -L\cos\alpha - D\sin\alpha \end{bmatrix} \tag{3.75}$$

Aerodynamic moments are modeled by defining a first-order delay relationship between the roll angle and asymmetric brake deflection. In contrast with [14], which supposed the lateral dynamics to remain constant over the duration of the flight, the terms K_ϕ and T_ϕ are further multiplied by V_T^2 and V_T respectively to model the effect of varying airspeed (resulting from variations in δ_s or ρ) on the lateral behavior of the system.

$$\underbrace{T_\phi V_T}_{T'_\phi}\dot{\phi} + \phi = \underbrace{K_\phi V_T^2}_{K'_\phi}\delta_a \tag{3.76}$$

Finally, we return to the linear acceleration (3.20), once again applying K2:

$$\begin{bmatrix}\dot{u}_a\\ \dot{v}_a\\ \dot{w}_a\end{bmatrix} = \frac{1}{m}\left(\mathbf{F}_a^b + \mathbf{F}_g^b\right) - \begin{bmatrix}p\\ q\\ r\end{bmatrix} \times \begin{bmatrix}u_a\\ v_a\\ w_a\end{bmatrix} \tag{3.77}$$

$$\begin{bmatrix}\dot{u}_a\\ 0\\ \dot{w}_a\end{bmatrix} = \frac{1}{m}\left(\mathbf{F}_a^b + \mathbf{F}_g^b\right) - \begin{bmatrix}qw_a\\ ru_a - pw_a\\ -qu_a\end{bmatrix} \tag{3.78}$$

$$\begin{bmatrix}\dot{u}_a\\ 0\\ \dot{w}_a\end{bmatrix} = \frac{1}{m}\left(\begin{bmatrix}L\sin\alpha - D\cos\alpha\\ 0\\ -L\cos\alpha - D\sin\alpha\end{bmatrix} + \begin{bmatrix}0\\ mg_0\sin\phi\\ mg_0\cos\phi\end{bmatrix}\right) - \begin{bmatrix}\dot{\psi}\sin(\phi)w_a\\ \dot{\psi}\cos(\phi)u_a - \dot{\phi}w_a\\ -\dot{\psi}\sin(\phi)u_a\end{bmatrix} \tag{3.79}$$

This results in the full set of state equations for the simplified model:

$$\dot{u}_a = \frac{1}{m}\left(L\sin(\alpha) - D\cos(\alpha)\right) - \dot{\psi}\sin(\phi)w_a \tag{3.80a}$$

$$\dot{\psi} = \frac{g_0\tan(\phi)}{u_a} + \frac{\dot{\phi}w_a}{\cos(\phi)u_a} \tag{3.80b}$$

$$\dot{w}_a = \frac{1}{m}\left(-L\cos(\alpha) - D\sin(\alpha)\right) + g_0\cos(\phi) + \dot{\psi}\sin(\phi)u_a \tag{3.80c}$$

$$\dot{\phi} = \frac{K_\phi V_T^2\delta_a - \phi}{T_\phi V_T} \tag{3.80d}$$

Finally, combining equation 3.70 with the wind vector yields the NED velocity equations:

$$v_N = \cos(\psi)u_a + \sin(\phi)\sin(\psi)w_a + w_N \tag{3.81a}$$

$$v_E = \sin(\psi)u_a - \sin(\phi)\cos(\psi)w_a + w_E \tag{3.81b}$$

$$v_D = \cos(\phi)w_a \tag{3.81c}$$

3.11 Validation of the 4-DOF model

3.11.1 Simulink implementation

In order to generate data to compare the behaviour of the 4-DOF model with that of the 6-DOF model, the 4-DOF model was also implemented in Simulink. (Fig. 3.18). Further detail on the custom blocks contained within the model can be found in Appendix C.

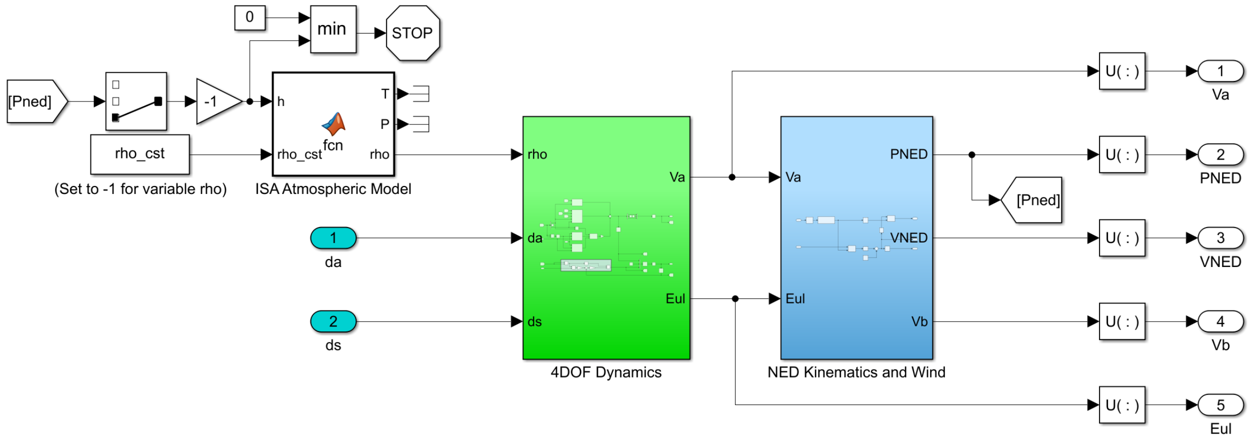

Figure 3.18 Simulink Implementation of the 4-DOF model

3.11.2 Model parameters

Tables 3.7 lists the parameters used with the 4-DOF model to obtain simulated data for comparison with the 6-DOF model. These parameters were obtained using the system identification procedure which will be detailed in Chapter 4 on simulated data from the 6-DOF model operating in windless conditions.

Parameter	Value	Unit	Parameter	Value	Unit
m	2.4	kg	C_{D0}	0.260	–
S	1	m^2	$C_{D\delta s}$	0.257	–
K_ϕ	0.0022	$\mathrm{rad{\cdot}s^2{\cdot}m^{-2}}$	C_{L0}	0.486	–
T_ϕ	0.284	$\mathrm{s^2{\cdot}m^{-1}}$	$C_{L\delta s}$	0.260	–

Table 3.7 4-DOF Model parameters used for comparison

3.11.3 Linearized model

To compare the dynamic modes of both models, the 4-DOF model was also linearized at an altitude of 500 m with no wind, resulting in a new set of equilibrium values and linear state equation:

$$u_e = 7.54 \text{ m/s}, \quad \psi_e = 0 \text{ rad}, \quad w_e = 4.03 \text{ m/s}, \quad \phi_e = 0 \text{ rad} \tag{3.82}$$

$$\begin{bmatrix} \Delta\dot{u} \\ \Delta\dot{\psi} \\ \Delta\dot{w} \\ \Delta\dot{\phi} \end{bmatrix} = \begin{bmatrix} -0.54 & 0 & 1.01 & 0 \\ 0 & 0 & 0 & 1.08 \\ -2.02 & 0 & -1.08 & 0 \\ 0 & 0 & 0 & -0.41 \end{bmatrix} \begin{bmatrix} \Delta u \\ \Delta\psi \\ \Delta w \\ \Delta\phi \end{bmatrix} + \begin{bmatrix} 0 & -1.86 \\ 0.035 & 0 \\ 0 & -6.23 \\ 0.067 & 0 \end{bmatrix} \begin{bmatrix} \Delta\delta_a \\ \Delta\delta_s \end{bmatrix} \tag{3.83}$$

3.11.4 Dynamic modes

Figure 3.19a shows that the 4-DOF model removes all but the slowest lateral and longitudinal modes of the system. The Dutch Roll, roll subsidence and short period modes are eliminated, leaving only the phugoid and spiral modes. This is as expected, as the slowest modes are the ones that have the most impact on the temporal response of the system. This is further explained by considering the states that were removed through simplification: all three of the missing modes involve the angular rates vector $\boldsymbol{\omega}^b$, which is no longer present in the 4-DOF model. The remaining phugoid mode involves an exchange between kinetic and potential energy, namely through variations in altitude and airspeed, both of which are still present in the simplified model. It is, however, slightly more damped due to the absence of the degree of freedom in pitch angle. The spiral mode appears in the yaw rate, which is still indirectly present as a system state due to the coupling of roll angle and yaw rate in the 4-DOF model.

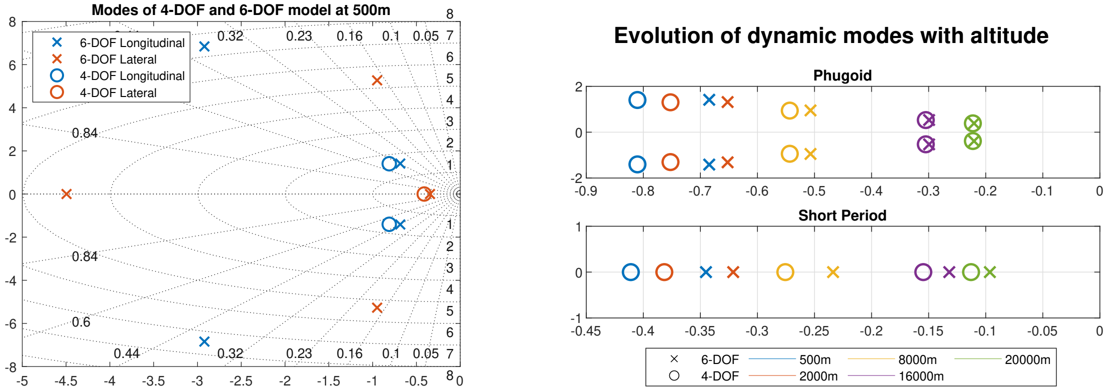

(a) Comparison of the dynamic modes of the linearized 4- and 6-DOF models

(b) Evolution of the linearized 4- and 6-DOF dynamic modes with altitude

When looking at the effect of altitude on the remaining modes (Fig. 3.19b), we can see that both models have a similar evolution, with the 4-DOF model presenting the same gradual reduction in stability and increase in responsiveness with increasing altitude.

These results provide an initial validation of the accuracy of the 4-DOF model, which will be further supported by comparing their trajectories during system identification.

CHAPTER 4 SYSTEMS IDENTIFICATION OF THE 4-DOF MODEL

Establishing the structure of the dynamic model of the system, as presented in the previous chapter, is a necessary step in developing control laws and being able to simulate its behavior for analysis and prediction purposes. However, before anything further can be done, one must have on hand the numerical values of the various parameters present in the model. It is therefore necessary to devise a method to estimate the model parameters of a given system from collected flight data. These collected measurements are necessarily imperfect, with inaccuracies stemming both from sensor errors and model simplifications. System identification techniques provide the tools needed to overcome this challenge.

This chapter describes the application of Maximum-Likelihood Estimation (MLE) and the Output-Error Method (OEM) to reconstruct an estimate of the system parameters of the 4-DOF model from experimental data. In this chapter, the measurements used are obtained from simulating the 6-DOF model and applying realistic errors to the system outputs to model imperfect sensors.

This method requires knowledge of system inputs and output measurements for an observed flight segment and assumes system noise is limited to the output measurements (as opposed to also including process noise). The application described is a form of *a posteriori* identification, meant to be performed after the fact (on previously collected data) rather than in real-time during flight.

Section 4.1 lays out the general theory behind Maximum-Likelihood Estimation techniques, and the application of the Output-Error Method to flight vehicle identification. Section 4.2 details the specifics of applying OEM methods to the parafoil system in the context of this project. Section 4.4 covers the exciting maneuvers required to obtain adequate data for proper identification. Section 4.5 shows the results of this method when applied to simulated measurements obtained from the 6-DOF model.

4.1 Maximum Likelihood Estimation and the Output Error Method

Before delving into the specifics of identification for the parafoil, this section provides a brief overview of the theory behind Maximum-Likelihood Estimation and the Output-Error Method, as well as detailing one of the possible optimization algorithms (Gauss-Newton). A more detailed and in-depth explanation can be found in [8].

Maximum likelihood estimation begins with the working assumption that we have in our

Variable	Description	Domain
N	Number of recorded observations	$\mathbb{N}$
n_y	Number of outputs in observation vector	$\mathbb{N}$
n_u	Number of system inputs	$\mathbb{N}$
n_p	Number of parameters to be determined	$\mathbb{N}$
$\mathbf{z}$	Observation vector	$\mathbb{R}^{n_y}$
$\mathbf{y}$	Expected outcome vector	$\mathbb{R}^{n_y}$
$\mathbf{u}$	Input vector	$\mathbb{R}^{n_u}$
$\mathbf{R}$	Measurement Noise Covariance Matrix	$\mathbb{R}^{n_y \times n_y}$
$\boldsymbol{\Theta}$	Parameter vector	$\mathbb{R}^{n_p}$

Table 4.1 List of variables used in OEM systems identification

possession a deterministic mathematical model that depends on some unknown parameters assembled in a vector $\boldsymbol{\Theta}$, and a set of N real-world observations $\{z_1, z_2, ..., z_N\}$. It follows that from this model and a given estimate of $\boldsymbol{\Theta}$, it is possible to compute a set of expected outcomes $\{y_1, y_2, ..., y_N\}$, one for each corresponding observation.

The given observations are not perfect: they contain noise or other sources of error. Consequently, they are considered to be sampled from a probability distribution around the expected outcome for that observation. Each observation is assumed to be independent and identically distributed (i.i.d.) to the others.

From the deterministic model and the known distribution, it is then possible to calculate the likelihood of obtaining these observations given a particular value of $\boldsymbol{\Theta}$. The final step is then to apply one of many existing optimization techniques to find the value of $\boldsymbol{\Theta}$ that maximizes this likelihood function, resulting in a Maximum Likelihood Estimate for the parameter vector $\boldsymbol{\Theta}$.

Following the assumption that the N random observations z_k in the sample are independent, the likelihood function is defined as:

$$\begin{aligned} p(z|\boldsymbol{\Theta}) &= p(z_1|\boldsymbol{\Theta}) \cdot p(z_2|\boldsymbol{\Theta}) \dots p(z_N|\boldsymbol{\Theta}) \\ &= \prod_{k=1}^{N} p(z_k|\boldsymbol{\Theta}) \end{aligned} \tag{4.1}$$

in which $p(z|\boldsymbol{\Theta})$ is the probability of obtaining a set of observations z given a parameter vector $\boldsymbol{\Theta}$.

4.1.1 The Output Error Method

The Output Error Method is an application of MLE where we take $\mathbf{\Theta}$ to be the set of unknown parameters in our dynamic model (which can also include properties of the sensors used, such as biases). The set of expected values becomes the expected output vector at each point in time $\{\mathbf{y}(t_0), .., \mathbf{y}(t_k)\}$ and can be calculated from the following:

- An initial state $\mathbf{x}_0$
- An estimated parameter vector $\mathbf{\Theta}$
- A sequence of inputs $\{\mathbf{u}(t_0), ..., \mathbf{u}(t_f)\}$
- The system state equation $\dot{\mathbf{x}} = \mathbf{f}(\mathbf{x}, \mathbf{u}, \mathbf{\Theta})$
- The system output equation $\mathbf{y} = \mathbf{g}(\mathbf{x}, \mathbf{u}, \mathbf{\Theta})$

This means that for each new estimate of $\mathbf{\Theta}$, a new set of expected outputs can be calculated through successive integration of the state equations and application of the observation equations. From these generated predictions, numerical optimization methods can be applied to iteratively adjust $\mathbf{\Theta}$ until a maximum likelihood estimate is obtained. Figure 4.1 shows a visualization of the working principle of this method.

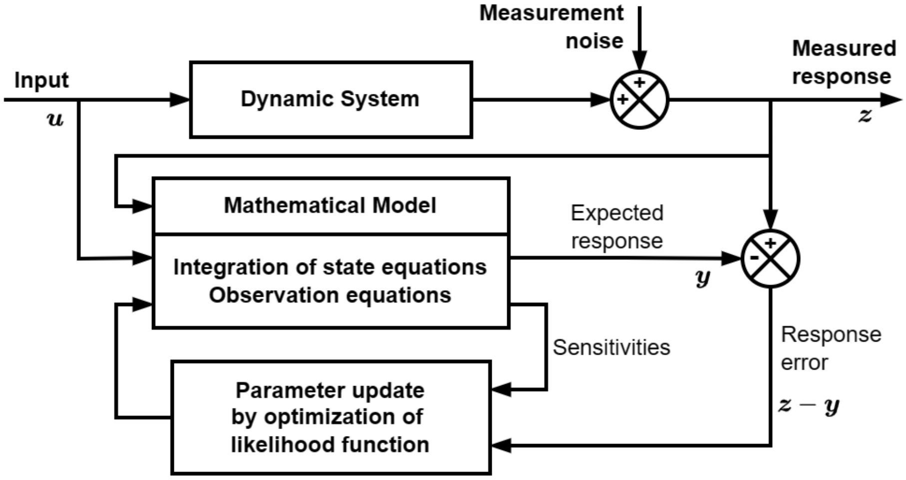

Figure 4.1 Block diagram of the Output Error Method, adapted from [8]

4.1.2 Cost Function

Maximizing the likelihood of an observation amounts to maximizing the probability density at the measurement z. Furthermore, the non-degenerate multivariate normal distribution for a vector of measurements is, for a given covariance matrix $\mathbf{R}$:

$$f_{\mathbf{z}}(z_1, ..., z_{n_y}) = \{(2\pi)^{n_y} \det(\mathbf{R})\}^{-\frac{1}{2}} \exp\left[-\frac{1}{2}(\mathbf{z}-\mathbf{y})^\top \mathbf{R}^{-1}(\mathbf{z}-\mathbf{y})\right] \tag{4.2}$$

Therefore, for a sample of measurements taken at N points in time, and assuming a normal distribution, the likelihood function becomes:

$$\begin{aligned} p[\mathbf{z}(t_1), ..., \mathbf{z}(t_N)|\mathbf{\Theta}, \mathbf{R}] &= \prod_{k=1}^{N} p[\mathbf{z}(t_k)|\mathbf{\Theta}, \mathbf{R}] \\ &= \{(2\pi)^{n_y} \det(\mathbf{R})\}^{-\frac{N}{2}} \exp\left[-\frac{1}{2}\sum_{k=1}^{N}[\mathbf{z}(t_k)-\mathbf{y}(t_k)]^\top \mathbf{R}^{-1}[\mathbf{z}(t_k)-\mathbf{y}(t_k)]\right] \end{aligned} \tag{4.3}$$

We could seek to directly maximize equation 4.3 to obtain the maximum likelihood estimate of $\mathbf{\Theta}$, but it turns out to be more practical to solve an equivalent problem, that of minimizing the negative logarithm of the likelihood function.

$$\hat{\mathbf{\Theta}}_{ML} = \arg\left\{\max_{\mathbf{\Theta}} p(\mathbf{z}|\mathbf{\Theta})\right\} = \arg\left\{\min_{\mathbf{\Theta}}[-\ln p(\mathbf{z}|\mathbf{\Theta})]\right\} \tag{4.4}$$

The resulting function, known as the *negative log-likelihood function*, is as follows:

$$L(\mathbf{z}|\mathbf{\Theta}, \mathbf{R}) = \frac{1}{2}\sum_{k=1}^{N}[\mathbf{z}(t_k)-\mathbf{y}(t_k)]^\top \mathbf{R}^{-1}[\mathbf{z}(t_k)-\mathbf{y}(t_k)] + \frac{N}{2}\ln[\det(\mathbf{R})] + \frac{Nn_y}{2}\ln(2\pi) \tag{4.5}$$

This likelihood function requires the knowledge of a covariance matrix $\mathbf{R}$, which in this case is the measurement noise covariance matrix. Assuming no prior knowledge of this matrix[1], it must be estimated before we can calculate the likelihood cost.

When the random measurement z is taken to be known to be normally distributed about the predicted value y, the maximum likelihood estimate of the covariance matrix is:

$$\mathbf{R} = \frac{1}{N}\sum_{k=1}^{N}[\mathbf{z}(t_k)-\mathbf{y}(t_k)][\mathbf{z}(t_k)-\mathbf{y}(t_k)]^\top \tag{4.6}$$

Substituting equation 4.6 into 4.5, we obtain:

$$J(\mathbf{\Theta}) = \frac{1}{2}n_y N + \frac{N}{2}\ln[\det(\mathbf{R})] + \frac{Nn_y}{2}\ln(2\pi) \tag{4.7}$$

---

[1] If the error sources were purely from sensor noise, it could be obtained from the characteristics of the sensors used, but in this case, there are other sources of error.

Since N (number of sample points) and n_y (size of the output vector) are taken to be fixed for a given dataset being analyzed, the first and last terms of equation 4.7 are constant and can be ignored during optimization efforts without affecting the found optimum. The final cost function thus simplifies to:

$$J(\mathbf{\Theta}) = \det(\mathbf{R}) \tag{4.8}$$

This new cost function is much simpler and less computationally intensive to implement than the original cost function described in equation 4.5.

4.1.3 Gauss-Newton Optimization of the parameter vector

Now that the relevant cost function and the method of computing it have been established, we move on to optimization techniques. In this case, optimization is performed using the Gauss-Newton method, but several viable alternate methods exist, including but not limited to Levenberg–Marquardt and direct search methods.

As with any optimization problem, minimizing the cost function in relation to $\mathbf{\Theta}$ amounts to finding a parameter vector such that:

$$\frac{\partial J(\mathbf{\Theta})}{\partial \mathbf{\Theta}} = 0 \tag{4.9}$$

We take an iterative numerical approach, where $\mathbf{\Theta}_i$ indicates the estimate of $\mathbf{\Theta}$ obtained on the ith iteration. The Taylor series expansion of $\frac{\partial J}{\partial \mathbf{\Theta}}$ about the ith value of $\mathbf{\Theta}$, truncated after two terms is:

$$\left(\frac{\partial J}{\partial \mathbf{\Theta}}\right)_{i+1} \approx \left(\frac{\partial J}{\partial \mathbf{\Theta}}\right)_i + \left(\frac{\partial^2 J}{\partial \mathbf{\Theta}^2}\right)_i \Delta\mathbf{\Theta} \tag{4.10}$$

Applying 4.9 to the left hand side of 4.10 and isolating $\Delta\mathbf{\Theta}$ yields:

$$\Delta\mathbf{\Theta} = -\left[\left(\frac{\partial^2 J}{\partial \mathbf{\Theta}^2}\right)_i\right]^{-1} \left(\frac{\partial J}{\partial \mathbf{\Theta}}\right)_i \tag{4.11}$$

This gives us the increment for obtaining the next iteration $\mathbf{\Theta}$ vector :

$$\mathbf{\Theta}_{i+1} = \mathbf{\Theta}_i + \Delta\mathbf{\Theta} \tag{4.12}$$

This process is repeated successively until either convergence or a maximum number of iterations is reached. Such a process is referred to as the Newton-Raphson method.

Per [8], the first and second derivatives of the cost function evaluate to the following:

$$\frac{\partial J}{\partial \boldsymbol{\Theta}} = -\sum_{k=1}^{N} \left[\frac{\partial \mathbf{y}(t_k)}{\partial \boldsymbol{\Theta}}\right]^\top \mathbf{R}^{-1}[\mathbf{z}(t_k) - \mathbf{y}(t_k)] \tag{4.13}$$

$$\frac{\partial^2 J}{\partial \boldsymbol{\Theta}^2} = -\sum_{k=1}^{N} \left[\frac{\partial \mathbf{y}(t_k)}{\partial \boldsymbol{\Theta}}\right]^\top \mathbf{R}^{-1} \frac{\partial \mathbf{y}(t_k)}{\partial \boldsymbol{\Theta}} + \sum_{k=1}^{N} \left[\frac{\partial^2 \mathbf{y}(t_k)}{\partial \boldsymbol{\Theta}^2}\right]^\top \mathbf{R}^{-1}[\mathbf{z}(t_k) - \mathbf{y}(t_k)] \tag{4.14}$$

Eq. 4.14 is overly computationally intensive due to the required calculation of second derivative $\left[\partial^2 \mathbf{y}(t_k)/\partial \boldsymbol{\Theta}^2\right]$, but it can be simplified because second term contains $[\mathbf{z}(t_k) - \mathbf{y}(t_k)]$ which eventually converges to zero and so can be neglected. With this simplification applied, the resulting optimization process is commonly known as the Newton-Balakrishnan or Gauss-Newton method.

$$\frac{\partial^2 J}{\partial \boldsymbol{\Theta}^2} = \sum_{k=1}^{N} \left[\frac{\partial \mathbf{y}(t_k)}{\partial \boldsymbol{\Theta}}\right]^\top \mathbf{R}^{-1} \left[\frac{\partial \mathbf{y}(t_k)}{\partial \boldsymbol{\Theta}}\right] \tag{4.15}$$

4.1.4 Calculating the Sensitivity Coefficients

The application of the Gauss-Newton method requires the computation, for the current parameter estimate vector $\boldsymbol{\Theta}$, of:

1. The system response $\mathbf{y}(t)$
2. The system response gradients $\partial \mathbf{y}(t_k)/\partial \boldsymbol{\Theta}$ for each time step

The system response is easily obtained through integration of the system state equations and subsequent application of the observation equations. The response gradients (referred to as "sensitivities" in Fig. 4.1) are calculated numerically through small perturbations in the elements of $\boldsymbol{\Theta}$. Using a first-order forward approximation, the resulting equation is:

$$\begin{aligned}\left[\frac{\partial \mathbf{y}(t_k)}{\partial \boldsymbol{\Theta}}\right]_{ij} &\approx \frac{\mathbf{y}_i^p(t_k) - \mathbf{y}_i(t_k)}{\delta \boldsymbol{\Theta}_j}; \quad i = 1, ..., n_y;\ j = 1, ..., n_p \\ &\approx \frac{\mathbf{g}_i[\mathbf{x}^p(t_k), \mathbf{u}(t_k), \boldsymbol{\Theta}^p] - \mathbf{g}_i[\mathbf{x}(t_k), \mathbf{u}(t_k), \boldsymbol{\Theta}]}{\delta \boldsymbol{\Theta}_j}\end{aligned} \tag{4.16}$$

Note that this requires recomputing the system response for a perturbation of each element of $\boldsymbol{\Theta}$, resulting in a computation of the elements of N $n_p \times n_y$ matrices for each iteration of the algorithm. Typically, the perturbation is selected proportionally to the current value of the parameters (e.g. $\delta\boldsymbol{\Theta}_j = 10^{-6}\boldsymbol{\Theta}_j$). This requires a minimum perturbation size, to avoid the perturbation being 0 when $\boldsymbol{\Theta}_j = 0$.

4.1.5 Step size and intermediate divergence

If at any point during the optimization procedure, it is detected that the cost has gone up relative to the previously calculated value (i.e. $J(\boldsymbol{\theta}_{i+1}) > J(\boldsymbol{\theta}_i)$), intermediate divergence has occurred. The algorithm can attempt to correct this by reducing the step size (typically halving it until a lower cost is found) to avoid this overshoot (Fig. 4.2).

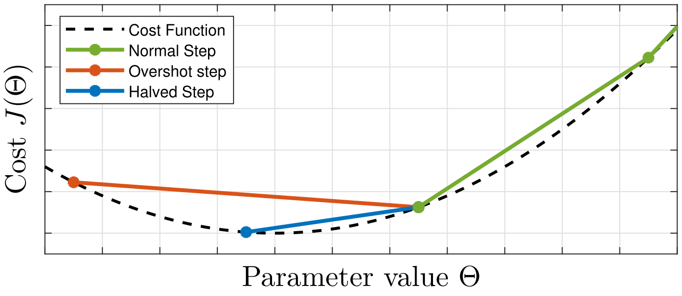

Figure 4.2 Illustration of intermediate divergence and its resolution by halving the step size

4.1.6 Using multiple flight segments

The OEM algorithm can also be used to analyze multiple flight segments simultaneously. This can be achieved by concatenating the input, output, and measurement values for each segment into global **u**, **y**, and **z** vectors.

$$\mathbf{u} = \begin{bmatrix} \mathbf{u}_1 & \mathbf{u}_2 & \dots & \mathbf{u}_n \end{bmatrix} \tag{4.17}$$

$$\mathbf{y} = \begin{bmatrix} \mathbf{y}_1 & \mathbf{y}_2 & \dots & \mathbf{y}_n \end{bmatrix} \tag{4.18}$$

$$\mathbf{z} = \begin{bmatrix} \mathbf{z}_1 & \mathbf{z}_2 & \dots & \mathbf{z}_n \end{bmatrix} \tag{4.19}$$

The rest of the algorithm can then be performed normally, using these global vectors and adjusting the initial conditions at the start of each segment.

4.1.7 Step-by-step summary of the OEM process

The general process for performing the output-error method, given input and measurement vectors **u** and **z**, and system state and output equations $\mathbf{f}(\mathbf{x}, \mathbf{u}, \boldsymbol{\Theta})$ and $\mathbf{g}(\mathbf{x}, \mathbf{u}, \boldsymbol{\Theta})$, is as follows:

1. Select initial values for $\mathbf{\Theta}$
2. Compute expected outputs $\mathbf{y}$ and residuals $\mathbf{z} - \mathbf{y}$ using the state and output equations
3. Estimate $\mathbf{R}$ (Eq. 4.6) and calculate $J(\mathbf{\Theta})$ (Eq. 4.7)
4. Minimize $J(\boldsymbol{\theta})$ with respect to $\mathbf{\Theta}$ using a nonlinear optimization method

   Using Gauss-Newton:

   (a) Compute gradient and Hessian matrices (Eqs. 4.13 and 4.15)
   (b) Compute parameter step $\Delta\mathbf{\Theta}$ (Eq. 4.11)
   (c) Compute new parameter vector $\mathbf{\Theta}_{i+1}$ (Eq. 4.12)
5. Repeat from step 2 until convergence or a maximum number of iterations is reached

4.2 Application to the 4-DOF parafoil model

Having established the general underlying principles behind the identification procedure, we can now delve into the specifics of applying this method to the parafoil model.

4.2.1 Instrumentation

The identification procedure requires information from four sensors :

1. Position encoders (one on each brake actuator)
2. GPS positioning module
3. 9-DOF inertial measurement unit (IMU)
4. Barometric altimeter

These sensors provide all the necessary data to derive the measurements detailed in Table 4.2. Commercially available flight computers such as the Pixhawk series and associated PX4 firmware typically support these sensors and have built-in functionality to take care of the requisite filtering and sensor fusion. As such, the values for each of the listed variables can be obtained directly through the logging capabilities provided by the flight computer.

Measurement	Description	Associated Sensor
ψ	Yaw angle	IMU
ϕ	Roll angle	IMU
v_N	Northbound velocity	GPS/IMU
v_E	Eastbound velocity	GPS/IMU
v_D	Sink rate	GPS/IMU/Altimeter
ρ	Air density	Altimeter
δ_l	Left brake deflection	Position encoder
δ_r	Right brake deflection	Position encoder

Table 4.2 Required measurements and associated sensors for identification

4.2.2 Known parameters

Model parameters that can be determined directly prior to flight tests are considered known prior to application of the identification algorithm. They are not considered part of the parameter vector $\mathbf{\Theta}$ and remain constant throughout the computation process. These include measureable physical characteristics of the system, actuator dynamics, and wind conditions. Table 4.3 summarizes these known parameters and their associated variables.

Category	Description	Parameter
Physical Characteristics	System mass	m
	Parafoil surface area	S
Actuator Dynamics	Time constant	T_δ
	Maximum slew rate	$\dot{\delta}_{max}$
Wind Conditions	Wind velocity	w_N, w_E

Table 4.3 Known parameters used during the identification procedure

4.2.3 Unknown parameters

The parameter vector gathers the system's lateral parameters and aerodynamic longitudinal coefficients:

$$\mathbf{\Theta} = \begin{bmatrix} K_\phi & T_\phi & C_{L0} & C_{L\delta s} & C_{D0} & C_{D\delta s} \end{bmatrix}^\top \tag{4.20}$$

4.2.4 State vector

The system state vector is the same as the one defined in Chapter 3, for the 4-DOF model:

$$\mathbf{x} = \begin{bmatrix} u_a & w_a & \phi & \psi \end{bmatrix}^\top \tag{4.21}$$

The state equations used are those previously defined (Eqs. 3.80a - 3.80d).

4.2.5 Input vector

The input vector consists principally, as in the model built in Chapter 3, of the symmetric and asymmetric brake deflections, resp. δ_s and δ_a. We also include the air density ρ.

$$\mathbf{u} = \begin{bmatrix} \delta_a & \delta_s & \rho \end{bmatrix}^\top \tag{4.22}$$

Using encoder measurements ensures that the inputs used for identification are the actual current deflections, instead of using the setpoints which do not take into account actuator dynamics. All input measurements are assumed to be adequately filtered and fully accurate for the purposes of the algorithm.

4.2.6 Output vector

In the majority of parafoil applications, it is much more feasible and convenient to install flight instrumentation on the gondola. As such, readings are susceptible to induced error from any existing relative motion between the canopy and payload, the most prominent of which is a discrepancy between the yaw angle of the gondola and the canopy. It is therefore more appropriate to use instead the heading angle, which more accurately describes the trajectory of the system, and happens to be implicitly included in the horizontal NED velocity readings. Combining GPS readings with known wind conditions thus provides all the necessary information related to the yaw angle of the vehicle, eliminating the need for explicit use of the yaw when calculating the difference between expected and measured outputs.

Following this reasoning, the measurement output vector used for identification is composed of the NED velocities and the roll angle:

$$\mathbf{y} = \begin{bmatrix} v_N & v_E & v_D & \phi \end{bmatrix}^\top \tag{4.23}$$

$$\mathbf{z} = \begin{bmatrix} \hat{v}_N & \hat{v}_E & \hat{v}_D & \hat{\phi} \end{bmatrix}^\top \tag{4.24}$$

The expected NED-frame velocity measurements are calculated from the system state and known wind conditions using equations 3.81a through 3.81c. The roll angle, already explicitly present in the system state, is used as is.

4.2.7 Initial state

The initial condition vector $\mathbf{x}_0 = \begin{bmatrix} u_a(t_0) & w_a(t_0) & \phi(t_0) & \psi(t_0) \end{bmatrix}^\top$ is calculated from the first entry in the measurement vector $\mathbf{z}$. Since all exciting maneuvers start with level flight, the initial roll angle is zero ($\phi(t_0) = 0$). Body-frame initial velocities are determined by rearranging equations 3.81a through 3.81c.

$$u_a(t_0) = \sqrt{(\hat{v}_N(t_0) - w_N)^2 + (\hat{v}_E(t_0) - w_E)^2} \tag{4.25a}$$

$$w_a(t_0) = \hat{v}_D(t_0) \tag{4.25b}$$

$$\phi(t_0) = 0 \tag{4.25c}$$

$$\psi(t_0) = \arccos\left(\frac{\hat{v}_N(t_0) - w_N}{u_a(t_0)}\right) \tag{4.25d}$$

4.3 Generation of simulated measurements

Simulated measurements were taken at a frequency of 25 Hz ($\Delta t = 0.04$s). Measurement errors were modeled through the addition of randomized Gaussian noise to the actual outputs of the 6-DOF simulation. For a given variable x and associated measurement $\hat{x}$:

$$\hat{x} = x + e \sim \mathcal{N}(0, \sigma_e) \tag{4.26}$$

The associated standard deviation for each measurement is listed in Table 4.4.

Measurements	$\sigma_\mathbf{e}$	**Unit**
v_N, v_E, v_D	0.5	m/s
p_N, p_E, p_D	2.5	m
ϕ, θ, ψ	0.025	rad

Table 4.4 Measurement noise parameters

4.4 Exciting maneuvers

In order to identify all the required coefficients, the exciting maneuver chosen for data collection must solicit both the lateral and longitudinal dynamics of the system. With the 4-DOF model, two such maneuvers are required: the first to identify longitudinal parameters C_{D0}, C_{L0}, $C_{D\delta s}$, and $C_{L\delta s}$, and another to identify lateral parameters K_ϕ and T_ϕ.

The longitudinal identification maneuver (Fig. 4.3a) consists of a steady-state glide with no control inputs followed by a constant symmetric deflection until a new steady-state is reached. The lateral identification maneuver (Fig. 4.3b) starts with a level glide, followed by the application of a constant asymmetric deflection until a steady turn is reached.

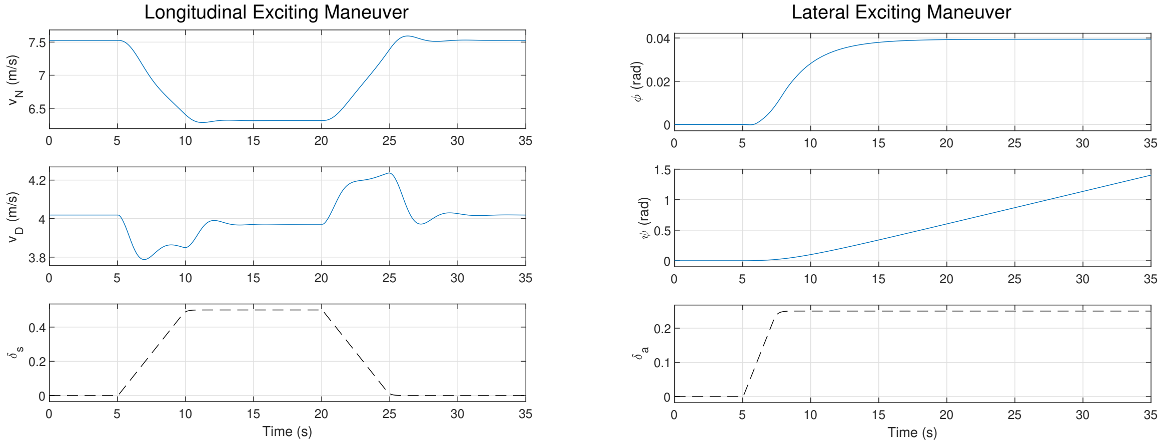

(a) Longitudinal

(b) Lateral

Figure 4.3 Exciting Maneuvers

For the results that follow, the longitudinal identification maneuver was performed once, followed by two instances of the lateral maneuver (one for each turn direction), resulting in a total of three flight segments to be analyzed.

4.5 Results

This section presents simulated results of the system identification procedure. Flight data was collected by executing a simulation using the 6-DOF model and the exciting maneuver inputs detailed in section 4.4. The resulting outputs were collected and simulated measurements were generated as per section 4.3. Table 4.5 shows the values for the parameters assumed known in the system, while table 4.6 shows the initial estimates used for the unknown parameters.

Parameter	**Value**	**Unit**
m	2.4	kg
S	1	m^2
T_δ	0.25	–
$\dot{\delta}_{max}$	0.1	s^{-1}

Table 4.5 Known parameters

Parameter	K_ϕ	T_ϕ	C_{L0}	$C_{L\delta s}$	C_{D0}	$C_{D\delta s}$
Initial Value	0.0025	0.25	0.25	0.25	0.25	0.25

Table 4.6 Initial estimates for unknown parameters

The identification procedure was performed at an altitude of 500 m. Three different scenarios, each with its own wind conditions, were tested: an ideal case with no wind ($|\mathbf{W}| = 0$ m/s), an average case with wind amplitude set according to wind data from Environment Canada's Wind Atlas[2] ($|\mathbf{W}| = 5$ m/s), and a worst-case scenario with winds double that of the average case ($|\mathbf{W}| = 10$ m/s).

4.5.1 Ideal vehicle orientation for exciting maneuvers

To determine the ideal starting heading for the identification maneuvers, we first evaluate the effect of relative wind angle γ (Fig. 4.4) on the quality of the identification. Relative wind direction is defined here as the angle between the wind vector and the body-frame forward direction x_b at the start of the identification maneuver.

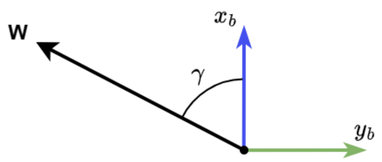

Figure 4.4 Definition of the relative wind angle γ

The identification algorithm was applied for data collected in the average and worst case wind scenarios, and its performance was evaluated over the full range of possible starting orientations. These results were compared to those obtained in the ideal case with negligible wind velocities. The results shown in Figure 4.5 indicate that the lowest final costs, and thus

---

[2] `http://www.windatlas.ca/index-en.php`

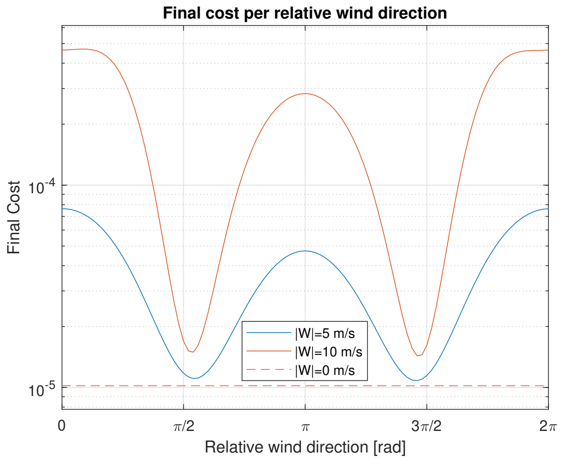

Figure 4.5 Effect of initial relative wind direction on final cost

the most accurate estimates, occur when identification is performed with the initial orientation of the vehicle being approximately perpendicular to the wind ($\gamma \approx \pm\frac{\pi}{2}$). Conversely, the highest costs are obtained when starting parallel to the wind, with a tailwind ($\gamma \approx 0$) giving slightly worse results than a headwind ($\gamma \approx \pi$).

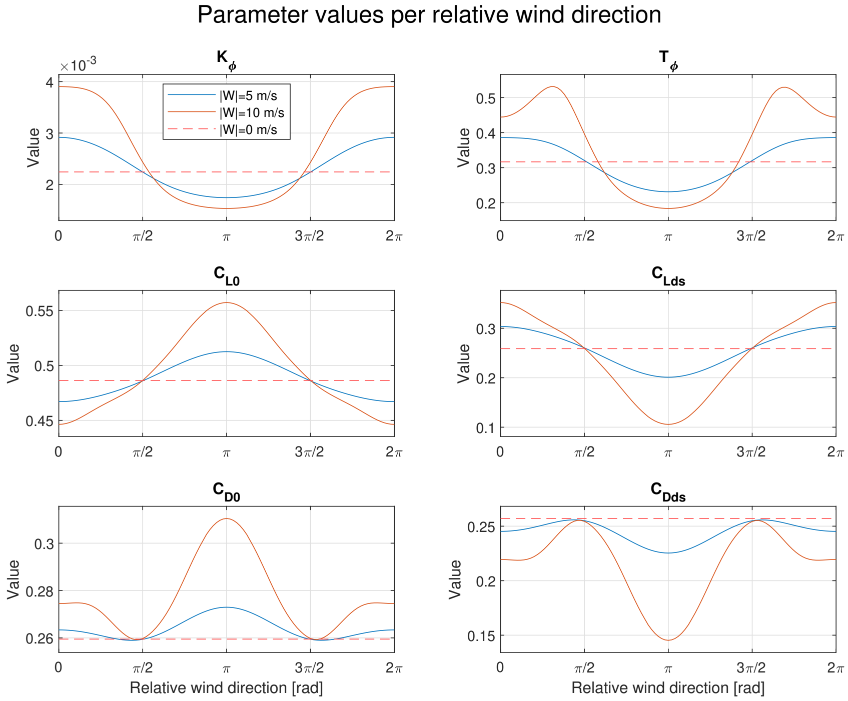

Figure 4.6 Effect of initial relative wind direction on resulting parameter estimates

The evolution of the resulting identified parameters presented in Figure 4.6 provides further insight into the source of these differences. In both wind scenarios, the longitudinal parameters converge to their ideal case values when $\gamma = \pm\frac{\pi}{2}$. The additional cost for the worst case scenario is due to errors in characterizing lateral dynamics, i.e., identifying parameters T_ϕ and K_ϕ.

Given these observations, an initial orientation $\gamma = \frac{\pi}{2}$ is used for subsequent results and analyses to ensure maximum accuracy.

4.5.2 Identified parameters

Table 4.7 displays the results from the parameter identification process in the different wind scenarios. The optimization algorithm converged within 5 iterations in all three cases.

Result	*Ideal case* $\lvert\mathbf{W}\rvert = 0$ m/s	*Average case* $\lvert\mathbf{W}\rvert = 5$ m/s	*Worst case* $\lvert\mathbf{W}\rvert = 10$ m/s	**Variation**
K_ϕ	2.20×10^{-3}	2.24×10^{-3}	2.41×10^{-3}	$+\ \mathbf{9.5}\%$
T_ϕ	2.84×10^{-1}	3.00×10^{-1}	3.64×10^{-1}	$+\mathbf{28.2}\%$
C_{L0}	4.86×10^{-1}	4.86×10^{-1}	4.86×10^{-1}	–
C_{Lds}	2.60×10^{-1}	2.59×10^{-1}	2.58×10^{-1}	$-\ \mathbf{0.8}\%$
C_{D0}	2.60×10^{-1}	2.60×10^{-1}	2.60×10^{-1}	–
C_{Dds}	2.57×10^{-1}	2.57×10^{-1}	2.56×10^{-1}	$-\ \mathbf{0.4}\%$
Final Cost	$\mathbf{1.02 \times 10^{-5}}$	$\mathbf{1.13 \times 10^{-5}}$	$\mathbf{1.60 \times 10^{-5}}$	$+\mathbf{56.9}\%$

Table 4.7 Parameter identification results

Analyzing the identified values across each case reveals that significant differences occur predominantly in the lateral coefficients, while the accuracy of the longitudinal coefficients is largely consistent. This consistency is coherent with the perpendicular orientation of the wind during the longitudinal maneuver, which given the previously posed assumption of negligeable lateral airspeed would not have any effect on the lift and drag forces. Additionally, since the longitudinal maneuver does not include any turns, the relative wind angle remains constant and its effect does not vary over the course of the maneuver.

In contrast, the lateral coefficients exhibit higher sensitivity to wind conditions. This arises because any lateral component of the wind relative to the body frame will have a small but non-negligeable effect on the steady state roll angle of the system. Additionally, during the turn, the relative orientation of the wind vector changes, and thus the effect will vary throughout the course of the manuever.

These findings are corroborated by the results obtained when determining the optimal relative wind direction comparison (Fig. 4.6). At $\gamma = \frac{\pi}{2}$, the longitudinal coefficients largely converge to the ideal case values, while the lateral coefficients present some error that increases with wind amplitude.

As such, we conclude that the chosen identification algorithm and exciting maneuvers, when combined with a carefully selected initial orientation, are effective at identifying system parameters even in reasonably high wind conditions.

4.5.3 Reconstructed trajectories

As a final validations step, a series of simulations were performed on the 4-DOF and 6-DOF models. Each model was subjected to the same sequence of inputs (Fig. 4.7) over a duration of 150 seconds, and the resulting trajectories were collected and compared. The objective of this comparison was to assess the performance of the simplified model and the effect of wind conditions during the identification procedure. To further confirm accuracy over the range of operating conditions, the tests were conducted twice: initially at low altitude of 500 m ($\rho = 1.17$ kg/m^3), followed by a high-altitude trial at 15000 m ($\rho = 0.19$ kg/m^3).

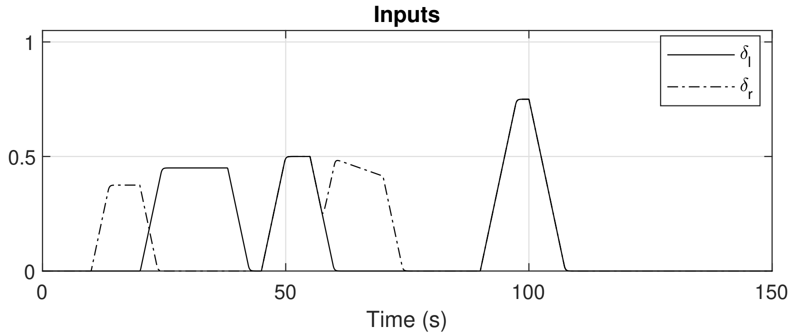

Figure 4.7 Input sequence used during validation

When reconstructing the trajectory at a low altitude, Figure 4.8 shows the reconstructed trajectories to be very accurate relative to the reference trajectory. Predictably, the quality of the reconstruction depends on the conditions under which the initial identification was performed; less optimal wind conditions lead to less accurate trajectory estimates. Despite this, even the worst case scenario presents minimal deviation from the 6-DOF reference.

Figure 4.9 repeats the exercise, but for a starting altitude of 15 km. It is immediately obvious that, despite using the same data, heading changes during turns are much more pronounced than at 500 m. This difference further highlights the effect of air density variation on lateral dynamics, and underlines the importance of the adjustments made to the 4-DOF model obtained from [14].

There is still a notable decline in trajectory accuracy with increasing altitude. This is due

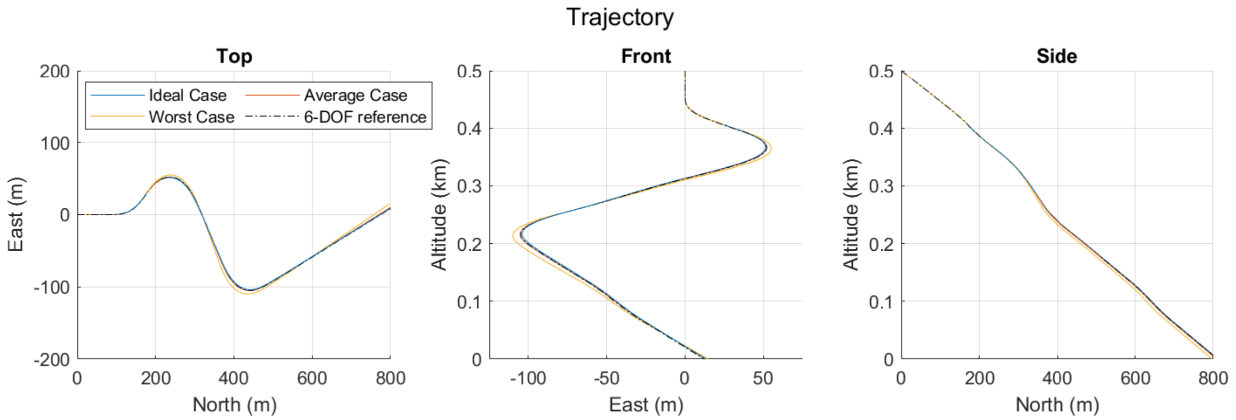

Figure 4.8 Reconstructed trajectories at 500 m

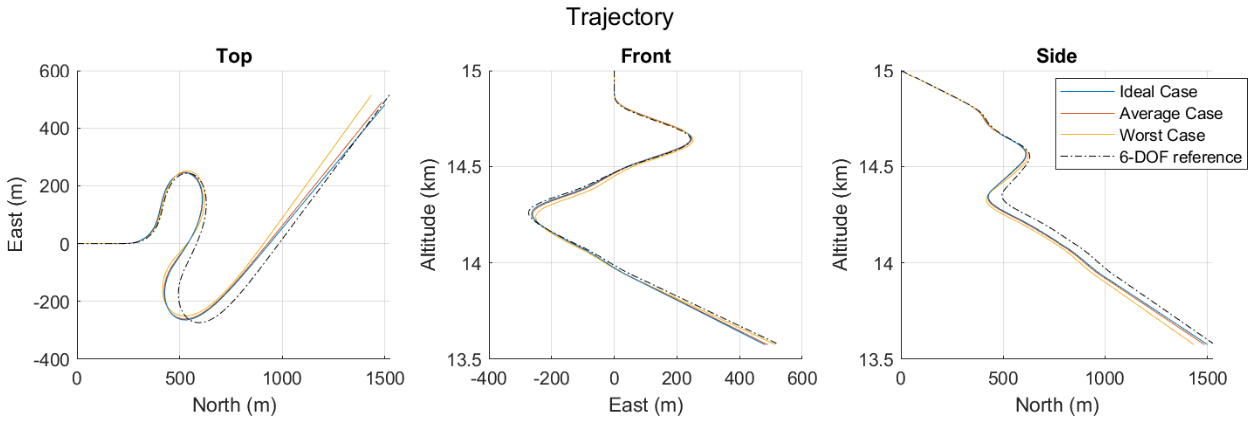

Figure 4.9 Reconstructed trajectories at 15000 m

to the static gain and time constant of the roll angle dynamics being represented as strictly proportional to the V_T^2 and V_T respectively (Eq. 3.76 : $K'_\phi = K_\phi V_T^2$, $T'_\phi = T_\phi V_T$). A more accurate approximation would be to use instead a linear relationship with nonzero intercept (e.g., $K'_\phi = K_\phi \left(V_T^2 + a\right)$). However, proper identification of the required parameters in this case would require an additional set of lateral identification maneuvers, performed at a second altitude that provides sufficient difference in steady-state airspeed. A compromise was made in opting for the slightly less accurate proportional relationship in order to maintain the feasibility of performing identification with a single low altitude flight, thus minimizing both the logistical complexity and associated risk of the procedure.

In both simulation scenarios, the reconstructed trajectories tend to gradually diverge from the reference as time goes on. Since the system outputs used for identification are velocity rather than position-based, small errors in velocity predictions are compounded by the continuous integration when calculating the resulting positions. While this would be an issue if using open-loop control, these minor discrepancies will be compensated with the addition of feedback control as detailed in the next chapter.

CHAPTER 5 CONTROL LAW SYNTHESIS

Following the system identification performed in Chapter 4, this chapter covers the synthesis of a control law based on the 4-DOF model. The control law is limited to the inner loop of a trajectory-based control method, following setpoints for the glide ratio and heading angle of the vehicle. This could be then combined with a generated trajectory in the form of a series of waypoints to be followed.

Section 5.1 provides a background on the linear methods used to synthesize the controller while Section 5.2.1 outlines the control objectives. Section 5.2.2 details the procedure of synthesizing gains over the envisioned flight envelope of the system. The remaining sections ared , and concludes with a validation through simulation of its performance when applied to the 6-DOF model (5.3.3).

5.1 Background

We begin with a brief overview of the linear control methods used in this chapter. First, we consider state feedback control and its application to regulate system outputs. We demonstrate how a feedback gain matrix can be used to alter the stability and dynamics of a linear system, and present two control architectures to ensure zero steady-state error. Eigenstructure assignment is the preferred method for achieving these gains, as it allows closed-loop poles to be assigned and decoupling constraints to be imposed. Finally, we cover optimal control using a linear quadratic regulator (LQR), in which the optimal system dynamics is determined by minimizing a weighted quadratic cost function encompassing system states and inputs.

5.1.1 Feedback control for linear systems

Our starting point is a linear time-invariant (LTI) multiple input, multiple output (MIMO) system with n states, m inputs, p outputs and q regulated outputs, represented by vectors $\mathbf{x} \in \mathbb{R}^n$, $\mathbf{u} \in \mathbb{R}^m$, $\mathbf{y} \in \mathbb{R}^p$, and $\mathbf{z} \in \mathbb{R}^q$ respectively. Given its classification as a MIMO system, we have $m \geq 2$ and $q \geq 2$.

The system dynamics can be expressed as the state-space model:

$$\dot{\mathbf{x}} = \mathbf{A}\mathbf{x} + \mathbf{B}\mathbf{u} \tag{5.1a}$$

$$\mathbf{y} = \mathbf{C}\mathbf{x} + \mathbf{D}\mathbf{u} \tag{5.1b}$$

$$\mathbf{z} = \mathbf{E}\mathbf{x} + \mathbf{F}\mathbf{u} \tag{5.1c}$$

with matrices of appropriate dimensions, i.e., $\mathbf{A} \in \mathbb{R}^{n\times n}$, $\mathbf{B} \in \mathbb{R}^{n\times m}$, $\mathbf{C} \in \mathbb{R}^{p\times n}$, $\mathbf{D} \in \mathbb{R}^{p\times m}$, $\mathbf{E} \in \mathbb{R}^{q\times n}$ et $\mathbf{F} \in \mathbb{R}^{q\times m}$.

The block diagram representation of this system is illustrated in Figure 5.1.

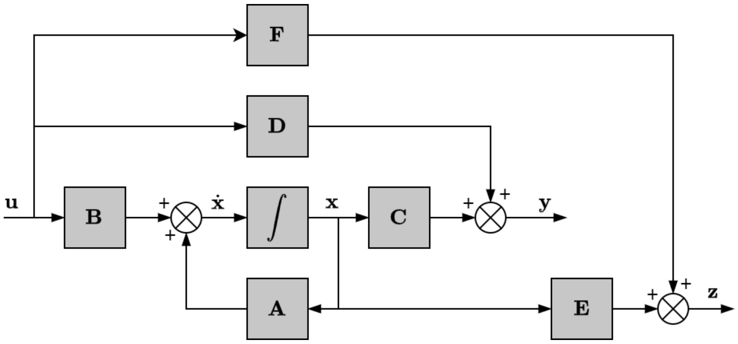

Figure 5.1 Open loop LTI system

Controllability and observability

Two important preliminary definitions are those of controllability and observability.

Definition 1 (Controllability): A system is **controllable** if for any time interval $[t_i, t_f]$, and for any $\mathbf{x}_i, \mathbf{x}_f \in \mathbb{R}^n$, there exists some sequence of inputs $\mathbf{u}(t)$ applied over $[t_i, t_f]$ that brings the system from an initial state $\mathbf{x}_i = \mathbf{x}(t_i)$ to the final state $\mathbf{x}_f = \mathbf{x}(t_f)$.

We can use the **A** and **B** matrices to calculate the controllability matrix $\mathbf{V} \in \mathbb{R}^{n\times nm}$:

$$\mathbf{V} \triangleq \begin{bmatrix} \mathbf{B} & \mathbf{A}\mathbf{B} & \cdots & \mathbf{A}^{n-1}\mathbf{B} \end{bmatrix} \tag{5.2}$$

The system is controllable if and only if **V** is of full row rank, i.e.

$$\text{rank}(\mathbf{V}) = n \tag{5.3}$$

meaning that all system states can be influenced by the system inputs.

Definition 2 (Observability): A system is **observable** if knowledge of the system inputs and outputs for a finite time interval $[t_i, t_f]$ is sufficient to determine the initial system state $\mathbf{x}(t_i)$, and by extension $\mathbf{x}(t)$ over $[t_i, t_f]$.

In a similar manner to controllability, we can use the state and output matrices **A** and **C** to assemble an observability matrix $\mathbf{U} \in \mathbb{R}^{np\times n}$:

$$\mathbf{U} \triangleq \begin{bmatrix} \mathbf{C} \\ \mathbf{CA} \\ \vdots \\ \mathbf{CA}^{n-1} \end{bmatrix} \tag{5.4}$$

The system is observable if and only if the **U** matrix is of full column rank, i.e.

$$\text{rank}(\mathbf{U}) = n \tag{5.5}$$

and thus the system outputs provide sufficient information to determine the full system state.

Stabilizability and Detectability

Two slightly weaker notions pertaining to controllability and observability are those of stabilizability and detectability. In the case where a system is not fully controllable or observable, stabilizability and detectability allow us to draw conclusions on the stability of the uncontrolled or unobserved dynamics of the system.

Definition 3 (Stabilizability): A system is **stabilizable** if all of its uncontrollable eigenvalues are asymptotically stable.

If the criteria

$$\text{rank}\left(\begin{bmatrix}\lambda_i \mathbf{I} - \mathbf{A} & \mathbf{B}\end{bmatrix}\right) = n \tag{5.6}$$

is respected for all eigenvalues λ_i of **A** with non-negative real part, the system is stabilizable.

Definition 4 (Detectability): A system is **detectable** if all of its unobservable eigenvalues are asymptotically stable.

Similarly, if the system respects the criteria

$$\operatorname{rank}\left(\begin{bmatrix} \lambda_i \mathbf{I} - \mathbf{A} \\ \mathbf{C} \end{bmatrix}\right) = n \tag{5.7}$$

for all eigenvalues λ_i of $\mathbf{A}$ with non-negative real part, the system is detectable.

State feedback control

In order to regulate the vector $\mathbf{z}$, we will use the architecture presented in Figure 5.2.

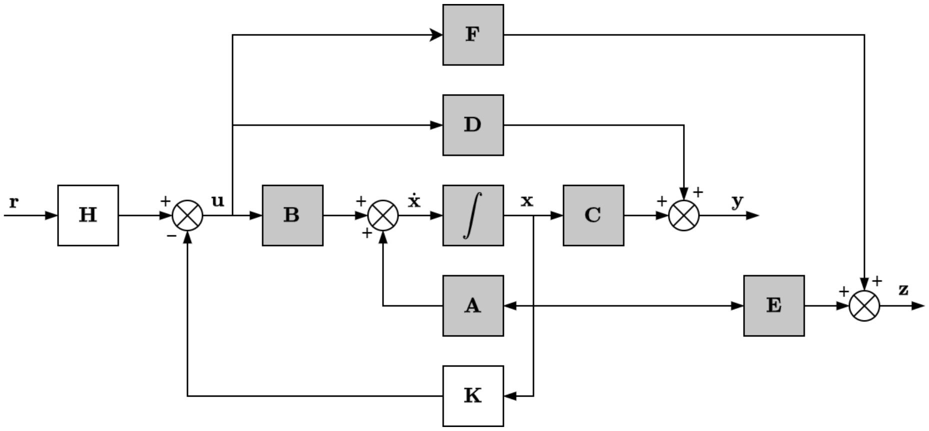

Figure 5.2 Regulator with state feedback and setpoint feedforward

The control law is then:

$$\mathbf{u} = -\mathbf{K}\mathbf{x} + \mathbf{H}\mathbf{r} \tag{5.8}$$

with $\mathbf{K} \in \mathbb{R}^{m \times n}$ and $\mathbf{H} \in \mathbb{R}^{m \times q}$ the state feedback and feedforward gain matrices respectfully, and $\mathbf{r} \in \mathbb{R}^q$ the setpoint vector which represents the desired value for the regulated output vector $\mathbf{z}$. By substituting the control law into Eqs. 5.1a and 5.1c, one obtains

$$\dot{\mathbf{x}} = \underbrace{(\mathbf{A} - \mathbf{B}\mathbf{K})}_{\tilde{\mathbf{A}}}\mathbf{x} + \mathbf{B}\mathbf{H}\mathbf{r} \tag{5.9a}$$

$$\mathbf{z} = \underbrace{(\mathbf{E} - \mathbf{F}\mathbf{K})}_{\tilde{\mathbf{E}}}\mathbf{x} + \mathbf{F}\mathbf{H}\mathbf{r} \tag{5.9b}$$

The eigenvalues of $\tilde{\mathbf{A}}$ determine the stability, and the transient response of the closed-loop system. If the system is fully controllable, these eigenvalues can be adjusted by the choice of $\mathbf{K}$. If the system is only partially controllable, only the controllable modes can be modified through state feedback. Various methods exist to calculate $\mathbf{K}$, such as eigenstructure assignment or LQR control. However, simple feedback control does not guarantee the elimination of steady state error, since the values of **K** that bring about the desired dynamics will generally result in a system with non-unitary DC gain.

The feedforward gain matrix **H** serves to compensate the DC gain of the closed loop system by scaling the setpoints appropriately. Additionally, when the number of inputs is different from the number of regulated outputs ($m \neq q$), the feedforward matrix performs control allocation of the various setpoint variables, mapping them to the available inputs.

Calculating the appropriate values for **H** after **K** has been selected requires analyzing the steady state response of the closed loop system. To solve for the steady state $\mathbf{x}_{ss}$, $\mathbf{z}_{ss}$ with a constant setpoint $\mathbf{r}(t) = \mathbf{z}_d$, we substitute these variables into Eq. 5.9 and set $\dot{\mathbf{x}} = 0$.

$$\mathbf{0} = \tilde{\mathbf{A}}\mathbf{x}_{ss} + \mathbf{B}\mathbf{H}\mathbf{z}_d \Rightarrow \mathbf{x}_{ss} = -\tilde{\mathbf{A}}^{-1}\mathbf{B}\mathbf{H}\mathbf{z}_d \tag{5.10a}$$

$$\mathbf{z}_{ss} = -\tilde{\mathbf{E}}\mathbf{x}_{ss} + \mathbf{F}\mathbf{H}\mathbf{z}_d \Rightarrow \mathbf{z}_{ss} = \left(-\tilde{\mathbf{E}}\tilde{\mathbf{A}}^{-1}\mathbf{B} + \mathbf{F}\right)\mathbf{H}\mathbf{z}_d \tag{5.10b}$$

From Eq. 5.10b, **H** can then be calculated such that $\mathbf{z}_{ss} = \mathbf{z}_{d,ss}$:

$$\mathbf{H} = \left(-\tilde{\mathbf{E}}\tilde{\mathbf{A}}^{-1}\mathbf{B} + \mathbf{F}\right)^{-1} \tag{5.11}$$

As an alternative to using a feedforward matrix, we can resort to integral control by integrating the regulated output error $\mathbf{e} = \mathbf{r} - \mathbf{z}$ as shown in Figure 5.3.

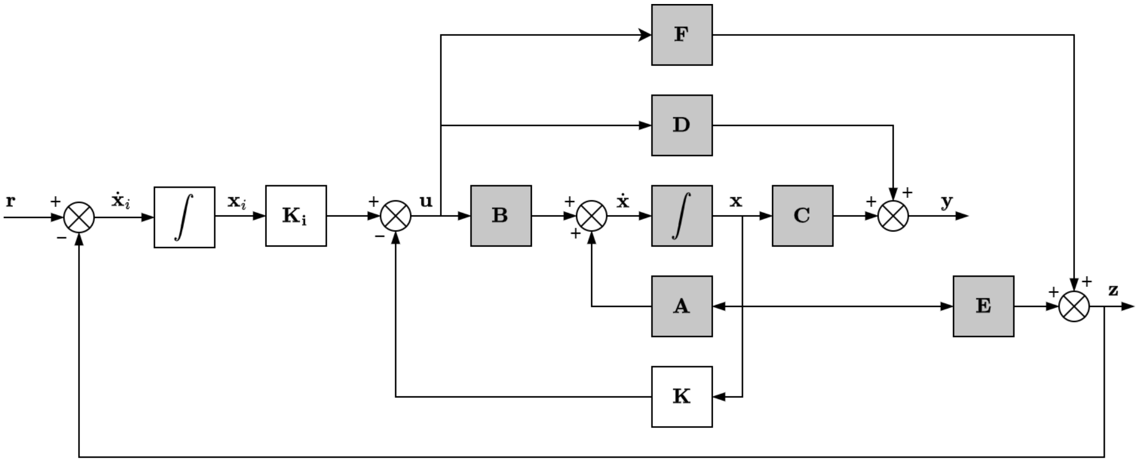

Figure 5.3 Regulator with state feedback and integral action

The control law is then:

$$\mathbf{u} = -\mathbf{K}\mathbf{x} + \mathbf{K}_i\mathbf{x}_i \tag{5.12}$$

with $\mathbf{x}_i$ the vector integral action state whose dynamics is defined by :

$$\dot{\mathbf{x}}_i = \mathbf{r} - \mathbf{z} = \mathbf{r} - \mathbf{E}\mathbf{x} - \mathbf{F}\mathbf{u} \tag{5.13}$$

This integral action eliminates the steady state error of the closed loop for step inputs, while also allowing the controller to compensate for errors introduced by modeling inaccuracies or system disturbances. The added integral state can be incorporated into the linear system equations by augmenting the system state and measured output vectors, resp. $\mathbf{x}_a$ and $\mathbf{z}_a$:

$$\mathbf{x}_a = \begin{bmatrix} \mathbf{x} \\ \mathbf{x}_i \end{bmatrix}, \quad \mathbf{z}_a = \begin{bmatrix} \mathbf{z} \\ \mathbf{x}_i \end{bmatrix} \tag{5.14}$$

which then allows us to assemble the state equations for the open-loop augmented system.

$$\dot{\mathbf{x}}_a = \underbrace{\begin{bmatrix} \mathbf{A} & \mathbf{0}_{n\times q} \\ -\mathbf{E} & \mathbf{0}_{q\times q} \end{bmatrix}}_{\mathbf{A}_a} \mathbf{x}_a + \underbrace{\begin{bmatrix} \mathbf{B} \\ -\mathbf{F} \end{bmatrix}}_{\mathbf{B}_a} \mathbf{u} + \begin{bmatrix} \mathbf{0}_{n\times q} \\ \mathbf{I}_q \end{bmatrix} \mathbf{r} \tag{5.15}$$

$$\mathbf{y}_a = \underbrace{\begin{bmatrix} \mathbf{C} & \mathbf{0}_{p\times q} \\ \mathbf{0}_{q\times n} & \mathbf{I}_q \end{bmatrix}}_{\mathbf{C}_a} \mathbf{x}_a + \underbrace{\begin{bmatrix} \mathbf{D} \\ \mathbf{0}_{q\times q} \end{bmatrix}}_{\mathbf{D}_a} \mathbf{u} \tag{5.16}$$

The control law (5.12) can now be rewritten as

$$\mathbf{u} = -\mathbf{K}\mathbf{x} + \mathbf{K}_i\mathbf{x}_i = -\underbrace{\begin{bmatrix} \mathbf{K} & -\mathbf{K_i} \end{bmatrix}}_{\mathbf{K}_a} \begin{bmatrix} \mathbf{x} \\ \mathbf{x}_i \end{bmatrix} = -\mathbf{K}_a\mathbf{x}_a \tag{5.17}$$

This results in a new linear system on which state feedback techniques can be used to determine $\mathbf{K}_a$, as long as the pair $(\mathbf{A}_a, \mathbf{B}_a)$ is controllable.

5.1.2 Eigenstructure assignment

One of the two methods used in this chapter for controller synthesis is known as Eigenstructure assignment. Given an LTI system and a set of desired pole positions, this method can be used to calculate the state feedback gain matrix that imposes the desired system dynamics. It can also serve to impose decoupling of certain inputs and outputs, in effect allowing the control of one output variable without significantly affecting the others.

Eigenvalues and Eigenvectors

Given a matrix $\mathbf{A} \in \mathbb{R}^{n\times n}$, the eigenvalues $\lambda_i \in \mathbb{C}$ and the associated right eigenvectors $\mathbf{v}_i \in \mathbb{C}^{n\times 1}$ are a set of vector-scalar pairs that each respect the relationship:

$$\mathbf{A}\mathbf{v}_i = \lambda_i \mathbf{v}_i \;\Rightarrow\; \Big(\mathbf{A} - \lambda_i \mathbf{I}\Big)\mathbf{v}_i = 0 \tag{5.18}$$

For an LTI system, the eigenvalues of $\mathbf{A}$ ($[\mathbf{A} - \mathbf{BK}]$ in closed-loop) represent the poles of the system, and thus the stability, rapidity and damping of each of the dynamic modes. The right eigenvectors can be used to determine the observability of each of the aforementioned dynamic modes:

$$\mathbf{E}\mathbf{v}_i \neq 0 \implies \lambda_i \text{ is observable by } \mathbf{z} \tag{5.19}$$

$$\mathbf{E}_k\mathbf{v}_i \neq 0 \implies \lambda_i \text{ is observable by } z_k \tag{5.20}$$

Pole placement

Applying Eq. 5.18 to the closed-loop state feedback equation 5.9a gives us the essential relationship for $\mathbf{K}$ to place a desired set of eigenstructures $(\lambda_i, \mathbf{v}_i)$:

$$\left(\mathbf{A} - \mathbf{BK}\right)\mathbf{v}_i = \lambda_i \mathbf{v}_i \tag{5.21}$$

which can be rewritten as

$$\begin{bmatrix}\mathbf{A} - \lambda_i \mathbf{I} & \mathbf{B}\end{bmatrix}\begin{bmatrix}\mathbf{v}_i \\ \mathbf{u}_i\end{bmatrix} = 0 \text{ with } \mathbf{K}\mathbf{v}_i = -\mathbf{u}_i \tag{5.22}$$

As such, the pair $(\lambda_i, \mathbf{v}_i)$ can be assigned in closed loop if and only if :

$$\begin{bmatrix}\mathbf{v}_i \\ \mathbf{u}_i\end{bmatrix} \in \ker\left(\begin{bmatrix}\mathbf{A} - \lambda_i \mathbf{I} & \mathbf{B}\end{bmatrix}\right) \tag{5.23}$$

Using full state feedback, we can place n eigenvalues, one for each system state. After finding a valid $\mathbf{v}_i$ and $\mathbf{u}_i$ for each, the gain matrix is calculated as follows:

$$\mathbf{K} = -\mathbf{U}\mathbf{V}^{-1} \text{ with } \begin{cases}\mathbf{V} \in \mathbb{C}^{n\times n} = \begin{bmatrix}\mathbf{v}_1 & \dots & \mathbf{v}_n\end{bmatrix} \\ \mathbf{U} \in \mathbb{C}^{m\times n} = \begin{bmatrix}\mathbf{u}_1 & \dots & \mathbf{u}_n\end{bmatrix}\end{cases} \tag{5.24}$$

Decoupling

For a MIMO system, decoupling between a given mode and a specific output z_k is ensured by the following relation:

$$\mathbf{E}_k\mathbf{v}_i + \mathbf{F}_k\mathbf{u}_i = 0 \implies \lambda_i \text{ has no influence on } z_k \tag{5.25}$$

Thus, we can augment the left side of Eq. 5.22 to include this additional constraint and simultaneously place a desired pole while decoupling its associated mode from output z_k :

$$\begin{bmatrix} \mathbf{A} - \lambda_i\mathbf{I} & \mathbf{B} \\ \mathbf{E}_k & \mathbf{F}_k \end{bmatrix} \begin{bmatrix} \mathbf{v}_i \\ \mathbf{u}_i \end{bmatrix} = 0 \implies \begin{bmatrix} \mathbf{v}_i \\ \mathbf{u}_i \end{bmatrix} \in \ker\left(\begin{bmatrix} \mathbf{A} - \lambda_i\mathbf{I} & \mathbf{B} \\ \mathbf{E}_k & \mathbf{F}_k \end{bmatrix}\right) \tag{5.26}$$

5.1.3 LQR Control

To find the set of desired eigenvalues to be placed with the previous method, we use optimal control, specifically LQR synthesis. The goal of this method is to find the state feedback control law $\mathbf{u} = -\mathbf{K}\mathbf{x}$ that minimizes the cost function

$$\mathcal{J} = \frac{1}{2}\int_0^\infty \left(\mathbf{x}^\top\mathbf{Q}\mathbf{x} + \mathbf{u}^\top\mathbf{R}\mathbf{u}\right) \mathrm{d}t,\ \mathbf{Q} = \mathbf{Q}^\top \succeq 0,\ \mathbf{R} = \mathbf{R}^\top \succ 0 \tag{5.27}$$

with $\mathbf{Q} = \mathbf{Q}^\top \in \mathbb{R}^{n\times n}$ a positive semi-definite matrix and $\mathbf{R} = \mathbf{R}^\top \in \mathbb{R}^{m\times m}$ a positive definite matrix. Thus, the cost function seeks to minimize both deviations from null state and the control effort exerted. The weight matrices $\mathbf{Q}$ and $\mathbf{R}$ are used to define the relative importance of each element. In order to calculate the optimal state feedback gain matrix $\mathbf{K}$, the conditions detailed in Tab. 5.1 must be met. The matrix $\mathbf{K}$ is then given by :

$$\mathbf{K} = \mathbf{R}^{-1}\mathbf{B}^\top\mathbf{P} \tag{5.28}$$

where $\mathbf{P}$ is the symmetric, positive semidefinite solution of the Ricatti equation:

$$\mathbf{P}\mathbf{A} + \mathbf{A}^\top\mathbf{P} - \mathbf{P}\mathbf{B}\mathbf{R}^{-1}\mathbf{B}^\top\mathbf{P} + \mathbf{Q} = 0 \tag{5.29}$$

Element	**Condition**
$(\mathbf{A}, \mathbf{B})$	Stabilisable
$\mathbf{R}$	Positive definite
$\mathbf{Q}$	Positive semi-definite
$(\mathbf{A}, \sqrt{\mathbf{Q}})$	Detectable

Table 5.1 Necessary conditions for LQR application

We can also directly weight the value of the output vector $\mathbf{z}$ instead of $\mathbf{x}$, such that the cost function reads as follows :

$$\mathcal{J} = \frac{1}{2}\int_0^\infty \left(\mathbf{z}^\top \mathbf{Q}\mathbf{z} + \mathbf{u}^\top \mathbf{R}\mathbf{u}\right) \mathrm{d}t \tag{5.30}$$

By substituting $\mathbf{z} = \mathbf{E}\mathbf{x}$ ($\mathbf{F}$ is generally null), the new cost function can be rewritten under the same form as the typical LQR cost function in Eq. 5.27 as :

$$\mathcal{J} = \frac{1}{2}\int_0^\infty \left(\mathbf{x}^\top \tilde{\mathbf{Q}}\mathbf{x} + \mathbf{u}^\top \mathbf{R}\mathbf{u}\right) \mathrm{d}t \tag{5.31}$$

with $\tilde{\mathbf{Q}} = \mathbf{E}^\top \mathbf{Q}\mathbf{E}$. Both of these versions of the LQR algorithm are available as part of Matlab's *Control System Toolbox*[1]. State based LQR (Eq. 5.27) can be performed using the `lqr` function, while the output based approach is implented as the `lqry` function.

5.1.4 Combined Procedure

Having outline all the necessary elements, we can now look at the whole procedure for synthesizing a state feedback controller from a given linear model. We first use LQR to find a state feedback that gives satisfying time responses, and yields the associated closed-loop poles. Next, we use eigenstructure assignment to calculate the state feedback gain matrix that places these same poles but ensures as well the desired decoupling, which was not achieved by the LQR synthesis. Finally, we eventually use the gain matrix to calculate the associated feedforward gain matrix for the system if needed. Figure 5.4 shows a visual representation of this process.

---

[1] `https://www.mathworks.com/products/control.html`

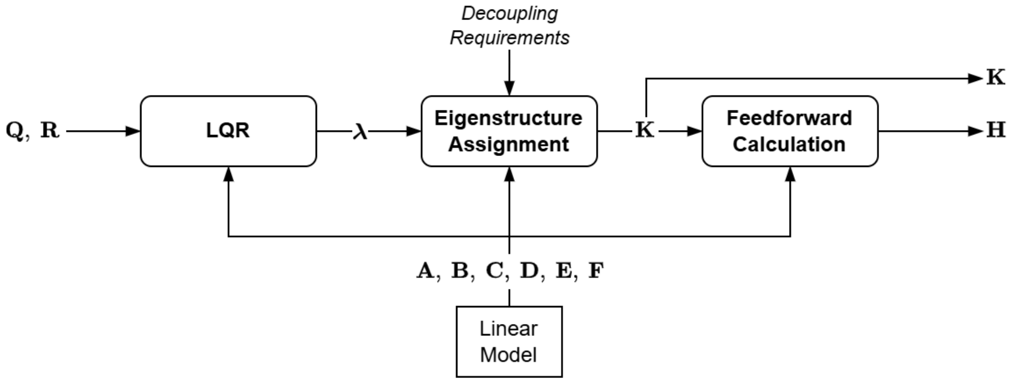

Figure 5.4 Workflow for controller synthesis

5.2 Controller synthesis

5.2.1 Control objectives

The controller to be synthesized here is the inner loop of a full trajectory based controller. To be able to navigate to a given point, the system must be able to maintain a desired heading and glide ratio. The heading is chosen instead of the yaw angle to allow the system to account for the presence of wind. Thus, the regulated output vector is $\mathbf{z} = \begin{bmatrix} \chi & GR \end{bmatrix}^\top$ with:

$$\chi = \operatorname{atan2}(V_E, V_N) \tag{5.32a}$$

$$GR = \frac{\sqrt{V_N^2 + V_E^2}}{V_D} \tag{5.32b}$$

For a given reachable setpoint, The performance objectives for the system response are:

- No steady-state error
- Less than 10% overshoot
- Less than 15 seconds settling time

A further criteria is the decoupling of both outputs. In other words, a change in the heading setpoint should minimally affect the glide ratio and vice versa.

5.2.2 General procedure

To account for the nonlinearities in the system resulting from varying air density, gain scheduling is applied to the controller, using the current altitude as the input argument. The model is linearized and the control law is synthesized for a set of altitudes within the operating range, and the resulting gains and equiblirium states are interpolated to obtain a control law that meets the given objectives over the entire flight envelope. Synthesis of the control law is performed in 3 stages:

1. **LQR synthesis to find desired pole positions**
   - 1.1 Select $\mathbf{Q}$ and $\mathbf{R}$ matrices to allow the desired performance in longitudinal and lateral control
   - 1.2 Calculate the equilibrium at the selected altitude and linearize the 4-DOF model
   - 1.3 Perform LQR synthesis and note the resulting poles
2. **Eigenstructure assignment to calculate gain matrices**
   - 2.1 Use eigenstructure assignment to synthesize gains that decouple longitudinal and lateral motion, and place the poles found in Step 1
   - 2.2 Calculate gain matrices for the given operating condition: state feedback $\mathbf{K}$, feed-forward gain $\mathbf{H}$ and integral action $\mathbf{K}_i$
3. **Gain scheduling over the range of operating conditions**
   - 3.1 Select series of operating points within range (altitudes)
   - 3.2 Repeat Steps 1 and 2 for each of the desired operating point altitudes
   - 3.3 Observe the evolution of the obtained gains and equilibrium values
   - 3.4 Establish an interpolation curve for each element: $\mathbf{H} = \mathbf{k}_{\mathbf{H}}(p_D)$, $\mathbf{K} = \mathbf{k}_{\mathbf{K}}(p_D)$, and $\mathbf{x}_{\mathbf{e}} = \mathbf{k}_x(p_D)$

5.2.3 Linear model

For synthesis, linearization is performed under no-wind conditions. The state, input, output and regulated output vectors are as follows:

$$\Delta\mathbf{x} = \begin{bmatrix}\Delta u_a & \Delta w_a & \Delta\phi & \Delta\psi\end{bmatrix}^\top \tag{5.33a}$$

$$\Delta\mathbf{u} = \begin{bmatrix}\Delta\delta_a & \Delta\delta_s\end{bmatrix}^\top \tag{5.33b}$$

$$\Delta\mathbf{y} = \begin{bmatrix}\Delta v_N & \Delta v_E & \Delta v_D & \Delta\phi & \Delta\psi\end{bmatrix}^\top \tag{5.33c}$$

$$\Delta\mathbf{z} = \begin{bmatrix}\Delta\chi & \Delta GR\end{bmatrix}^\top \tag{5.33d}$$

As the system is linearized about a steady glide with no control inputs, starting in a northern-facing direction, several equilibrium values are always zero.

$$\delta_{a,e} = \delta_{s,e} = \phi_e = \psi_e = \chi_e = 0 \tag{5.34}$$

The remaining states, GR_e, $u_{a,e}$ and $w_{a,e}$ must be determined numerically based on the steady-state at the chosen altitude.

5.2.4 Control architecture

The architecture selected is full state feedback with regulated outputs. To ensure zero steady state error even in the presence of modeling errors, the direct path for each of the regulated outputs must contain an integrator. For lateral control, δ_a affects roll angle, which is proportional to the derivative of the yaw angle and so no added integral action from the controller is actually necessary. For longitudinal control, δ_s affects the glide ratio directly, and in a slightly nonlinear fashion as shown in Figure 3.11b. Thus integral action is needed on the glide ratio error. Figure 5.5 shows the architecture used for the linear controller.

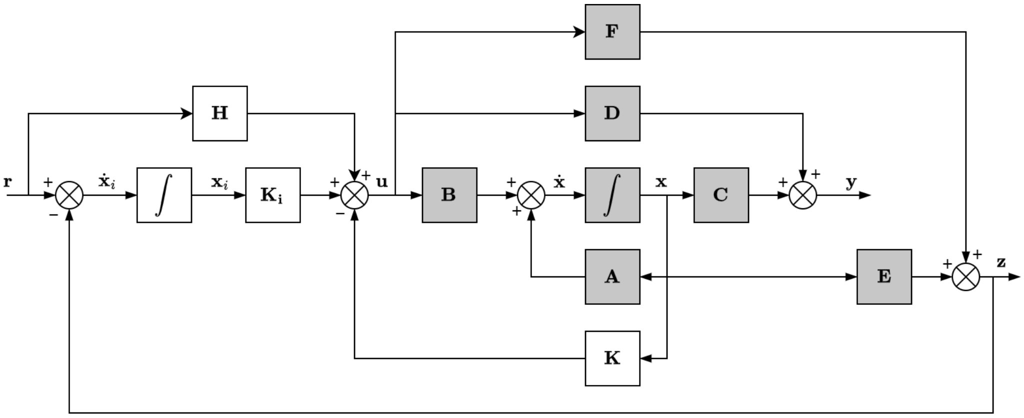

Figure 5.5 Architecture of the linear parafoil controller

The associated control law is

$$\Delta \dot{GR}_i = \Delta GR_d - \Delta GR \tag{5.35a}$$

$$\Delta \mathbf{u} = -\mathbf{K}\mathbf{x} + \mathbf{H}\mathbf{r} + \mathbf{K}_i GR_i \tag{5.35b}$$

The system state and outputs are therefore augmented to include the integral of the error for the GR setpoint. The integrator state is also included in the regulated output to be minimized during LQR synthesis:

$$\mathbf{x}_a = \begin{bmatrix} \Delta u_a & \Delta w_a & \Delta \phi & \Delta \psi & \Delta GR_i \end{bmatrix}^\top \tag{5.36a}$$

$$\mathbf{z}_a = \begin{bmatrix} \Delta \psi & \Delta GR & \Delta GR_i \end{bmatrix}^\top \tag{5.36b}$$

From there, we can define the augmented state matrices that will be used for synthesis:

$$\mathbf{A}_a = \begin{bmatrix} \mathbf{A} & \mathbf{0} \\ -\mathbf{E}_2 & 0 \end{bmatrix}, \quad \mathbf{B}_a = \begin{bmatrix} \mathbf{B} \\ -\mathbf{F}_2 \end{bmatrix} \tag{5.37a}$$

$$\mathbf{E}_a = \begin{bmatrix} \mathbf{E} & \mathbf{0} \\ \mathbf{0} & 1 \end{bmatrix}, \quad \mathbf{F}_a = \begin{bmatrix} \mathbf{F} \\ \mathbf{0} \end{bmatrix} \tag{5.37b}$$

5.2.5 LQR Synthesis

The weight matrices **Q** and **R** were chosen to prioritize heading accuracy over glide ratio, as for navigation purposes a precise heading is more important. After a number of iterations, the final values retained were as follows:

$$\mathbf{Q} = \begin{bmatrix} 10 & 0 & 0 \\ 0 & 0.1 & 0 \\ 0 & 0 & 0.1 \end{bmatrix} \quad \mathbf{R} = \begin{bmatrix} 1 & 0 \\ 0 & 1 \end{bmatrix} \tag{5.38}$$

The optimal state feedback gains and closed loop pools were calculated using MATLAB's `lqry` function.

5.2.6 Controller design at 500 m

Linearizing the system about a steady glide provided the system equilibrium values:

$$\mathbf{x}_e = \begin{bmatrix} 7.55 & 7.03 & 0 & 0 \end{bmatrix}^\top, \quad \mathbf{u}_e = \begin{bmatrix} 0 & 0 \end{bmatrix}^\top, \quad \mathbf{z}_e = \begin{bmatrix} 0 & 1.87 \end{bmatrix}^\top \tag{5.39}$$

as well as the augmented state matrices.

$$\mathbf{A}_a = \begin{bmatrix} -0.54 & 1.01 & 0 & 0 & 0 \\ -2.02 & -1.08 & 0 & 0 & 0 \\ 0 & 0 & -0.41 & 0 & 0 \\ 0 & 0 & 1.08 & 0 & 0 \\ -0.25 & 0.46 & 0 & 0 & 0 \end{bmatrix}, \quad \mathbf{B}_a = \begin{bmatrix} 0.07 & 0 \\ 0.04 & 0 \\ 0 & -1.86 \\ 0 & -6.23 \end{bmatrix} \tag{5.40}$$

Per the rank condition for controllability, the system is fully controllable, therefore full state feedback can place all the system poles. The calculated gains obtained with the procedure described in Section 5.2.2 are then:

$$\mathbf{K} = \begin{bmatrix} 0 & 0 & 3.01 & 1.58 \\ -0.18 & -0.12 & 0 & 0 \end{bmatrix}, \quad \mathbf{K}_i = \begin{bmatrix} 0 \\ -0.22 \end{bmatrix}, \quad \mathbf{H} = \begin{bmatrix} 1.58 & 0 \\ 0 & -1.182 \end{bmatrix} \tag{5.41}$$

Comparing the closed-loop dynamics to the open loop system (Fig. 5.6), we see that the Phugoid mode becomes faster and more damped, and the yaw and spiral modes combine into a pair of complex poles slightly slower than the original spiral mode. An additional pole also appears for the glide ratio integrator.

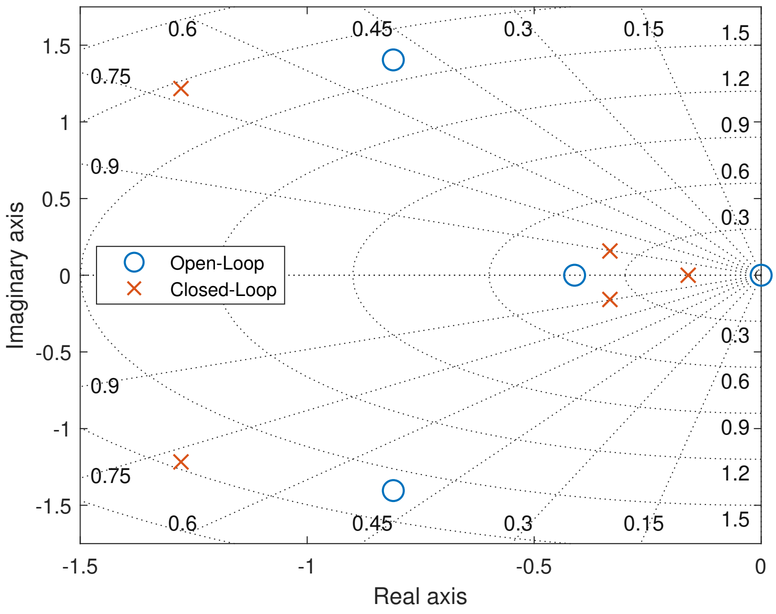

Figure 5.6 System poles at 500m

Analyzing the step responses of the closed-loop system (Fig. 5.7) confirms that the control objectives are met. The heading response settles in just over 12 seconds with no overshoot, while the glide ratio response settles in under 4 seconds with 10% overshoot.

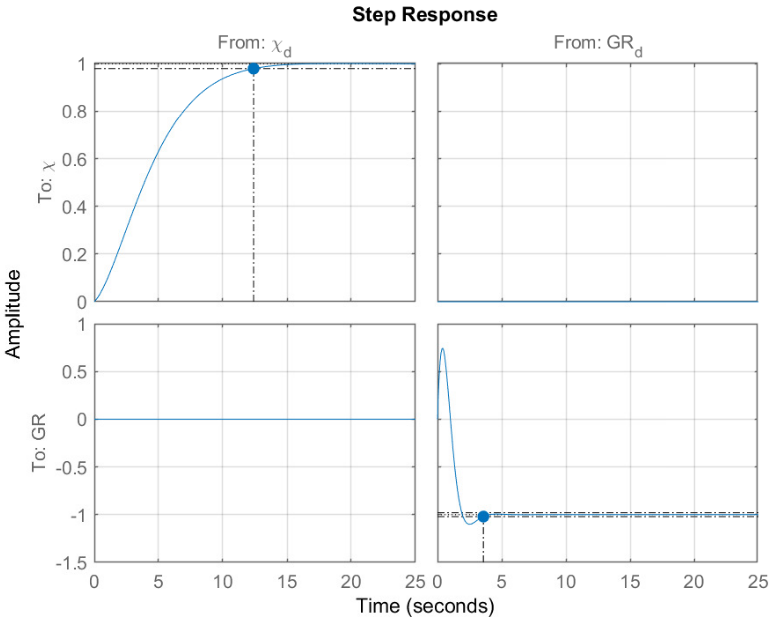

Figure 5.7 Closed loop step response of the linearized 4-DOF model

5.2.7 Gain Scheduling

The linear controller was synthesized at 6 different altitudes: 500 m, 4400 m, 8300 m, 12200 m, 16100 m, and 18000 m. The evolution of the closed-loop poles can be seen in Fig. 5.8.

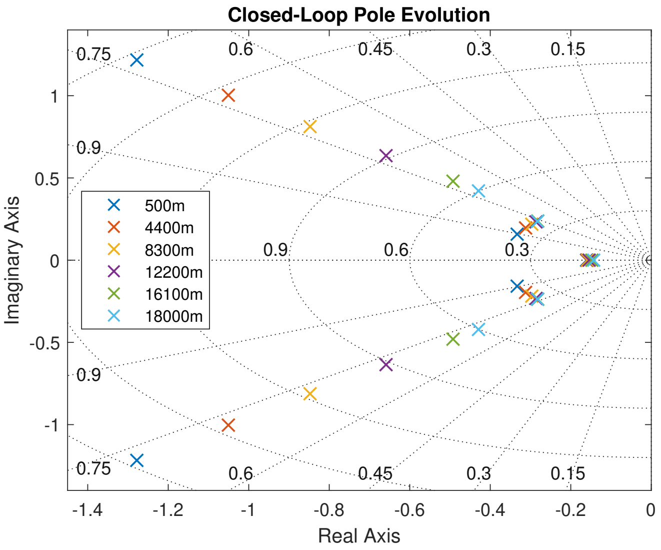

Figure 5.8 Closed-loop pole evolution with altitude

Interpolation curves were then constructed using quadratic functions.

$$k(h) = a_2 h^2 + a_1 h + a_0 \tag{5.42}$$

Table 5.2 shows the calculated coefficients for each of the scheduled parameters. The resulting curves provide a very good fit for the computed values, as seen in Figs. 5.9 and 5.10.

Element	$\mathbf{a_2} \times \mathbf{10^{10}}$	$\mathbf{a_1} \times \mathbf{10^{5}}$	$\mathbf{a_0}$
u_e	437	8.02	7.68
v_e	234	4.29	4.11
$\mathbf{K}_{13}$	-17.6	-6.90	3.05
$\mathbf{K}_{14}$	0	0	1.58
$\mathbf{K}_{23}$	-0.466	0.273	-0.181
$\mathbf{K}_{24}$	-0.657	0.633	-0.126
$\mathbf{K}_{i,2}$	0	0	-0.224
$\mathbf{H}_{11}$	0	0	0.158
$\mathbf{H}_{22}$	-0.296	-0.264	-0.182

Table 5.2 Polynomial coefficients for the gain scheduling curves.

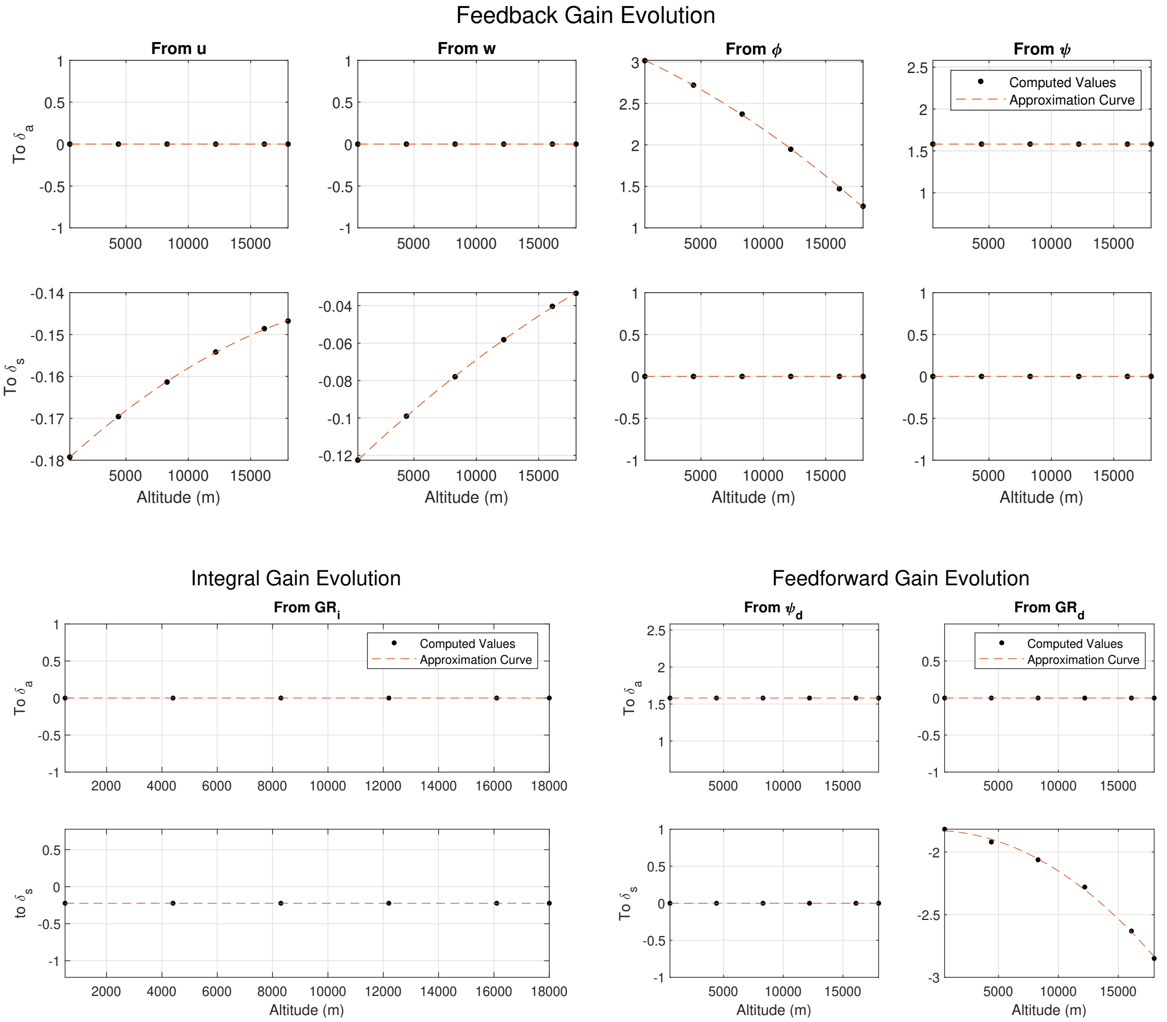

Figure 5.9 Gain Scheduling curves

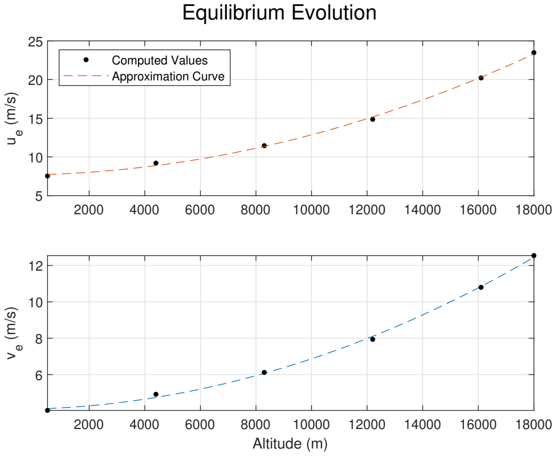

Figure 5.10 Body frame equilibrium curves

5.3 Validation of the synthesized controller

5.3.1 Implementation

The synthesized controller was implemented in Simulink for validation and testing, with some additional features. Input limiting based on altitude was applied to δ_a, constraining the roll angle during turns to remain below 0.15 radians (approximately 10°), i.e.,

$$\delta_{a,max} = \min\left(1, \frac{0.15V_{T,e}^2}{K_\phi}\right) \tag{5.43}$$

The physical limitations for symmetric deflection relative to asymmetric deflection (Eq. 3.49d) were also implemented as :

$$\delta_{s,max} = 1 - |\delta_a| \tag{5.44}$$

Integral clamping was applied to avoid integral windup when the δ_s input is saturated, i.e., when the output of the linear controller is outside the range of valid system inputs:

$$\dot{GR_i} = \begin{cases} GR_d - GR & \text{if } \delta_s \in [0, \delta_{s,max}] \\ 0 & \text{otherwise} \end{cases} \tag{5.45}$$

Finally, the control setpoints were rate limited to avoid oscillations in the nonlinear system:

$$\dot{\chi}_d \leq \frac{\pi}{60} \text{ rad/s}, \quad \dot{GR_d} \leq 0.01 \text{ s}^{-1} \tag{5.46}$$

The resulting full closed loop implementation in Simulink can be seen in Fig. 5.11.

5.3.2 Initial validation on the 4-DOF model

Initial validation was performed using the 4-DOF model, testing the system response over a range of altitudes to step inputs in glide ratio and heading, followed by a triangle wave input in heading. The results, shown in Fig. 5.12, demonstrate excellent performance in heading control.

The glide ratio response is also adequate, notwithstanding the limited range of valid setpoints and a slight degradation of performance at higher altitudes. Decoupling between outputs is also adequate with some degradation at higher altitudes.

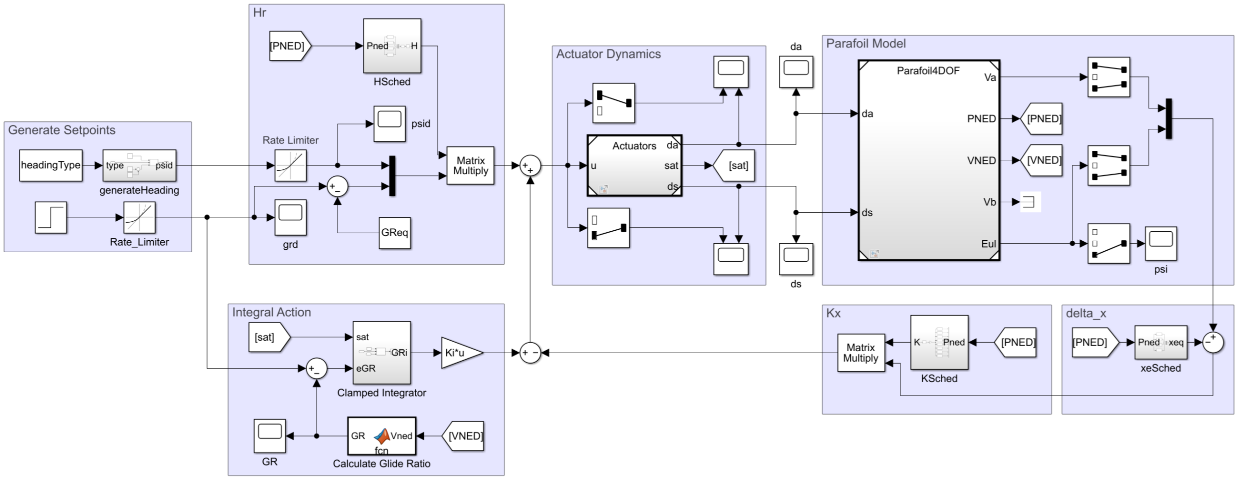

Figure 5.11 Simulink Model for the closed-loop 4-DOF system

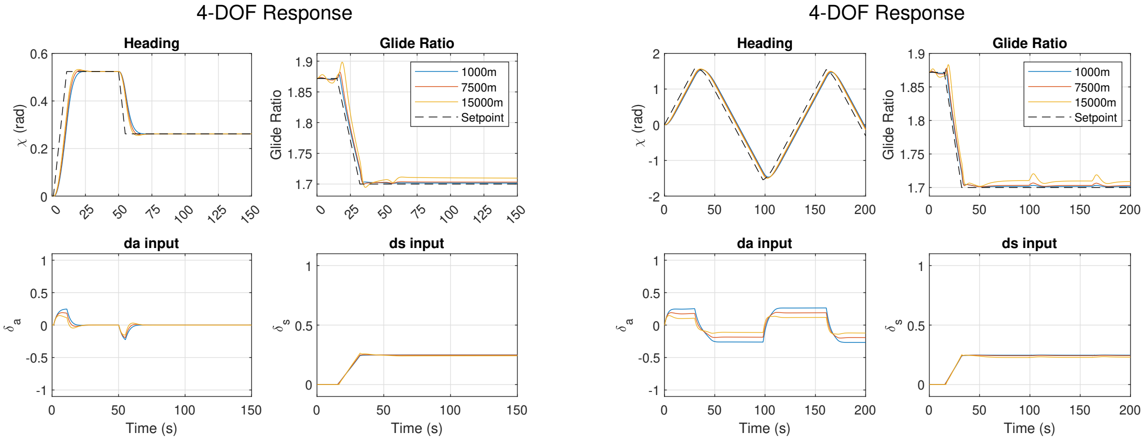

Figure 5.12 Simulated 4-DOF closed loop system reponse at various altitudes, without wind

5.3.3 Validation on the full 6-DOF model

Final validation was performed by applying the control law to the 6-DOF system for a series of trials. Each trial consisted of following a trajectory defined as a series of waypoints, which were randomly generated and selected to be reachable under no wind conditions within the glide ratio capabilities of the parafoil. The actively targeted waypoint was updated to the next waypoint when the ground distance between the parafoil and the current target crossed a threshold of 1 meter. All validation trials were run for 1500 seconds (25 minutes), or until touchdown.

Measured outputs were converted to the 4-DOF body-frame velocities and heading through the simple approximations defined in Eq. 5.47. Roll and yaw angle were taken directly from available measurements:

$$u_a = \sqrt{(V_N - W_N)^2 + (V_E - W_E)^2} \tag{5.47a}$$

$$w_a = \frac{V_D}{\cos \phi} \tag{5.47b}$$

The validation process tested controller robustness relative to three adverse factors:

- **Presence of wind**

  To validate the controller's robustness in the presence of winds, 3 trials were performed at an altitude of 5000 m, with varying amplitudes of easterly winds.

- **Changes in altitude**

  To validate the effectiveness of the gain scheduling algorithm, trials were performed at starting altitudes of 15000 m and 1500 m, shown in Figs. 5.14 and 5.13.

- **Variations in model parameters**

  Finally, to validate the controller's robustness to variations in model parameters, two series of Monte-Carlo simulations were performed at a starting altitude of 5000 m. In each trial, system parameters were individually varied according to a normal distribution about their nominal values (Tab. 3.4), following

  $$C_i = (1 + x)C_i,\ x \sim \mathcal{N}(0, \sigma_{param}) \tag{5.48}$$

  Two runs of 25 trials each were performed, with $\sigma_{param} = 0.1$ (Fig. 5.16) and 0.25 (Fig. 5.17).

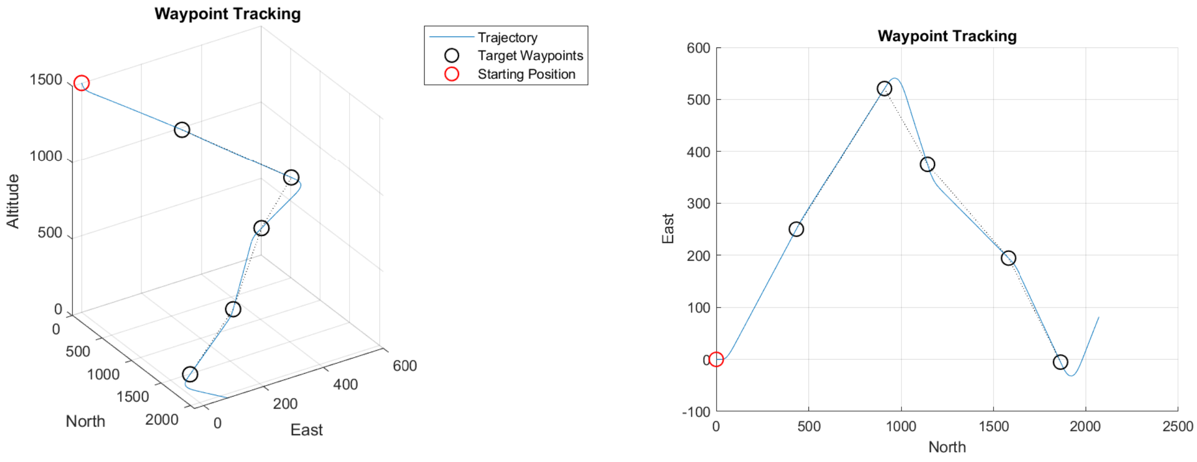

(a) Oblique view **(b)** Top view

Figure 5.13 Waypoint tracking: starting altitude 1500 m, no wind

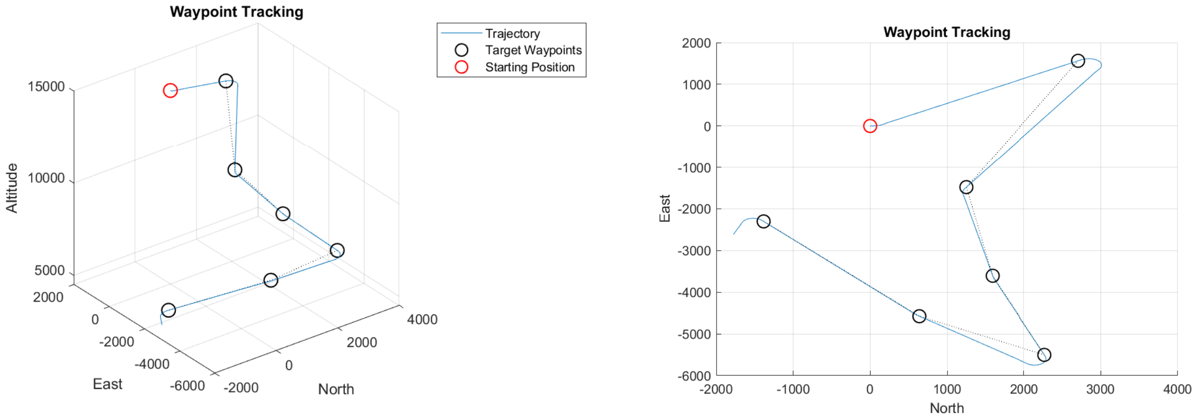

(a) Oblique view **(b)** Top view

Figure 5.14 Waypoint tracking: starting altitude 15000 m, no wind

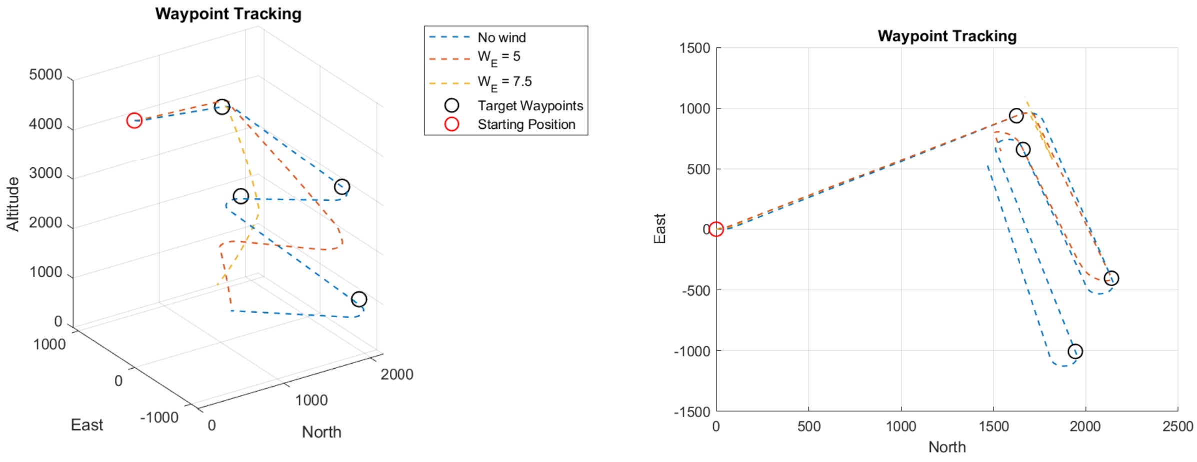

(a) Oblique view (b) Top view

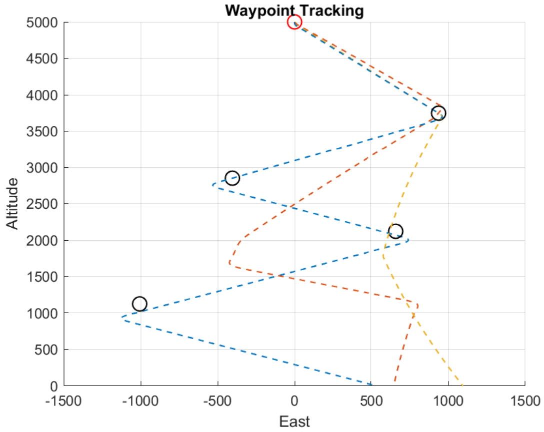

(c) Side view

Figure 5.15 Waypoint tracking: starting altitude 5000 m, with wind

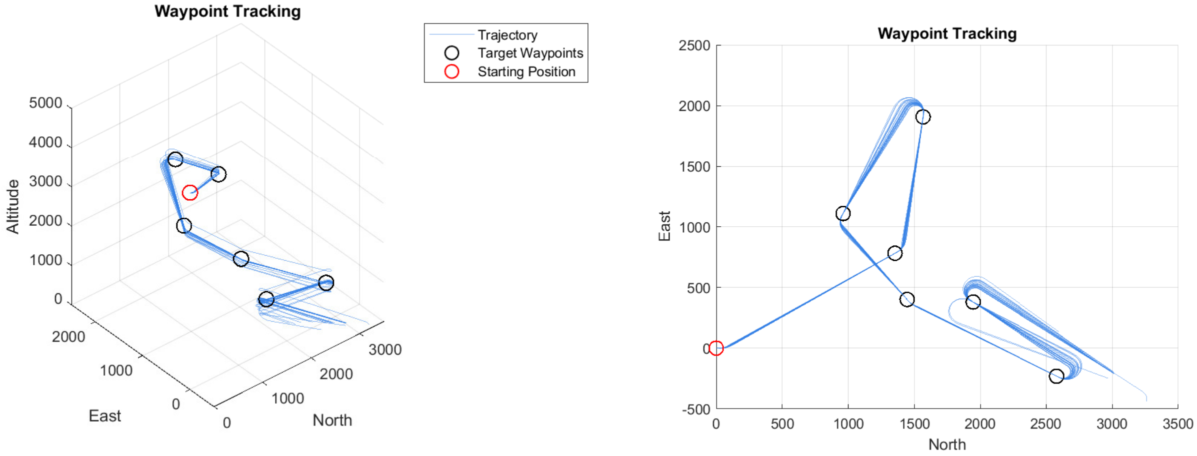

(a) Oblique view (b) Top view

Figure 5.16 Waypoint tracking: starting altitude 5000 m, no wind, $\sigma_{param} = 0.1$

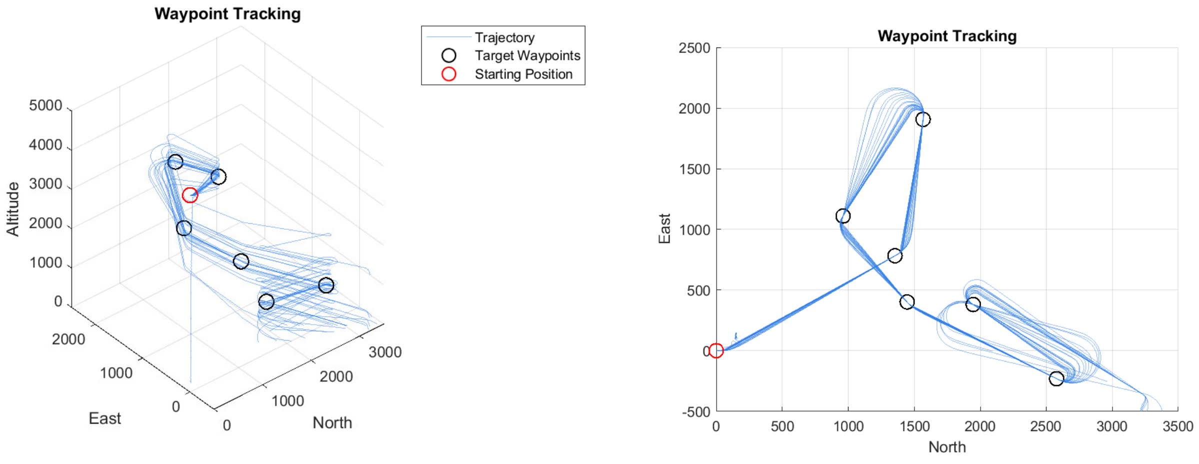

(a) Oblique view **(b)** Top view

Figure 5.17 Waypoint tracking: starting altitude 5000 m, no wind, $\sigma_{param} = 0.25$

From these trials the controller demonstrates good robustness in heading for every aspect tested, as evidenced by the top view of each figure. In almost all cases, the parafoil accurately follows the ground trajectory of the waypoints. The only deviation from this observation is when wind conditions present exceed the forward airspeed of the parafoil, at which point it is no longer able to navigate against the wind. This can be seen in Figure 5.15c for $W_E = 7.5$ m/s, where the trajectory begins drifting in the opposite direction of the second waypoint once the altitude reaches 1750 m.[2]

However, glide ratio control is severely affected by wind, but robust to altitude changes and modeling error. A tailwind equal to the forward airspeed of the parafoil will double its glide ratio, while a headwind of the same magnitude diminishes the glide ratio to zero, resulting in a trajectory that leads straight down. Due to the limited range of influence symmetric deflection on glide ratio, wind will easily bring the system into a state where δ_s input alone cannot effectively counteract the wind. In cases where this leads to overshooting the waypoint, additional maneuvers such as repeated turns can be used to shed altitude and reach the waypoint exactly, but in the opposite case the lost altitude cannot be regained, possibly requiring an adjustment to the rest of the planned trajectory. Two possible avenues could be explored to remedy this. On the one hand additional actuation methods could be incorporated to increase the amount of longitudinal control authority. Another solution would be to make use of publicly available atmospheric wind data to predict when such issues might arise and plan a more conservative trajectory in response.

---

[2] At higher altitudes, the vehicle's air speed is higher than the wind speed, so this effect does not manifest immediately. As air density increases, the parafoil slows down and cannot penetrate the wind as effectively.

For the application of guided descent to a target landing location, longitudinal control could also be omitted entirely in favor of choosing an objective that is either downwind or well within the range of the parafoil based on its nominal glide ratio, giving the operator plenty of vertical distance to spare, and regulating altitude through a series of additional maneuvers rather than direct control of the gondola's glide ratio.

CHAPTER 6 CONCLUSION

6.1 Summary of Works

The objective of this research work was to present and demonstrate a concretely usable framework for the modeling, identification and control of a parafoil and payload system, suited for the challenges of stratospheric applications. The methodology presented here is effective, and low enough in logistic and computational complexity to be versatile and applicable in many resource-limited contexts (e.g. startups, academic research and independent science).

Chapter 3 introduced an expanded version of an existing 4-DOF parafoil model from the literature that takes into account the effect of altitude and air density on lateral dynamics, increasing its accuracy while preserving the advantages offered by its low complexity. This was followed in Chapter 4 by the elaboration of an output-error based methodology that allows for identification of system parameters according to this model using measurements from a single low-altitude test flight, using GPS and filtered IMU data combined with actuator encoders. The accuracy of both the 4-DOF model and the identification methodology were validated through a series of trials using simulated measurements from a higher fidelity 6-DOF parafoil model, demonstrating the effectiveness of the identification results even in the presence of reasonably forseeable wind conditions. Finally, Chapter 5 demonstrated the effectiveness of the simplified model as a basis for controller synthesis, presenting one possible avenue for inner-loop control of the parafoil system. Using LQR synthesis and eigenstructure assignment, a combined longitudinal-lateral controller regulating both the heading and glide-ratio of the descent trajectory was synthesized and simulated on the 6-DOF model. The simulated trials highlighted excellent lateral control robustness over changes in altitudes, wind conditions and system uncertainty. Longitudinal control, while limited in scope, was also shown to be generally effective, despite a notable weakness in the face of unfavorable winds.

6.2 Limitations

Despite the general success of the efforts presented in this research work, some limitations to the methodology and solutions proposed must be highlighted.

Most evident is the heavy reliance on simulation for validation and testing of the various methodologies. While the data thusly gathered is a good indicator for the potential usefulness of the presented techniques, a more accurate depiction of performance must be obtained from real test flights in an uncontrolled environment before any definitive conclusions can be drawn. Additional insight could be gained into the problem through more rigorous and complex modeling, such as updating the simplistic wind model and its constant wind assumption, or further validating identification and control results on an even higher fidelity parafoil model (as stated in Section 3.2, contemporary models available in the literature can include as many as 12 degrees of freedom). Nonetheless, if the resources are available, real-world trials remain the best possible avenue for decisively validating the findings presented here.

Furthermore, a deeper look into the numerical stability of the output-error algorithm presented would be a welcome addendum to the content of Chapter 4, as convergence is dependent on the initial conditions given to the optimiser and is not guaranteed. While finding adequate initial values was largely achievable through non-rigourous means, the technique as presented does not offer a rigorous view of the stability limits of the algorithm, nor an easily implemented strategy for selecting initial parameter estimates.

As mentioned above, the longitudinal control of the parafoil also presents a challenge. Due mainly to the physical limitations of the selected actuator configuration, limiting inputs to left and right brake deflections and forgoing any other adjustments of the canopy geometry, the range of achievable glide ratios is constrained to approximately 1.4-1.9. While useful for minor in-flight adjustments, this range offers little recourse for the correction of larger deviations in trajectory.

6.3 Future research

Future work based on this thesis can be separated into two categories: either improving on the present methodology, or using it as a stepping stone for additional efforts in return-to-point functionality on parafoil systems.

In the first category, additional validation could be performed by replacing the simple wind model with a more accurate representation, including a wind vector that varies both as a function of time and altitude, incorporating the effects of wind gusts and turbulence. Adding a strategy for the selection of initial parameter estimates would guarantee convergence of the identification algorithm and reduce time spent fine-tuning the procedure for each new vehicle. Implementing a state observer to obtain more accurate inputs for feedback control would likely increase performance of the presented control law. And, as emphatically mentioned while discussing limitations, applying this entire methodology to a real-world system would be a very appropriate next step in efforts for validating and improving the results presented.

In the second category, armed with an appropriately accurate 4-DOF model for the parafoil system, more complex control efforts could be undertaken. Future researchers could shift their focus to optimally and robustly planning the flight trajectory, or use the simplified model directly to produce advanced implementations of robust or optimal controllers. An important consideration is the analysis and addition of specific flight maneuvers to the pallette of possible actions the vehicle can make, especially when it comes to the final approach before touchdown.

REFERENCES

[1] S. Sankey, "Blueprint for Wildland Fire Science in Canada (2019–2029)," Natural Resources Canada, Canadian Forest Service, Tech. Rep., 2018. [Online]. Available: https://ostrnrcan-dostrncan.canada.ca/handle/1845/250868

[2] T. Fields, J. LaCombe, and E. Wang, "One Degree of Freedom Approach for an Autonomous Descent Vehicle Using a Variable Drag Parachute," in *21st AIAA Aerodynamic Decelerator Systems Technology Conference and Seminar.* American Institute of Aeronautics and Astronautics, May 2011.

[3] S.-I. Higashino *et al.*, "The Antarctic Stratospheric Aerosol Observation and Sample-Return System Using Two-Stage Separation Method of a Balloon-Assisted Unmanned Aerial Vehicle," *Atmospheric Measurement Techniques Discussions*, vol. 2021, pp. 1–20, 2021.

[4] D. Jorgensen and M. Hickey, "The AGAS 2000 Precision Airdrop System," in *Infotech@Aerospace.* American Institute of Aeronautics and Astronautics, Jun. 2005.

[5] T. D. Fields, "Evaluation of Control Line Reefing Systems for Circular Parachutes," *Journal of Aircraft*, vol. 53, no. 3, pp. 855–860, May 2016.

[6] J. Haller, T. Fields, and O. Yakimenko, "Precision Aerial Delivery with a Steerable Cruciform Parachute," in *24th AIAA Aerodynamic Decelerator Systems Technology Conference.* Denver, CO: American Institute of Aeronautics and Astronautics, Jun. 2017.

[7] "Spacewedge." [Online]. Available: https://www.nasa.gov/image-article/spacewedge-4/

[8] R. V. Jategaonkar, *Flight Vehicle System Identification: A Time Domain Methodology.* American Institute of Aeronautics and Astronautics, 2006.

[9] S. Lingard, "Basic Analysis of Ram-Air Parachute," in *Precision Aerial Delivery Systems: Modeling, Dynamics, and Control*, ser. Progress in Astronautics and Aeronautics. American Institute of Aeronautics and Astronautics, Jan. 2015, pp. 73–125.

[10] Canadian Council of Forest Ministers, "Canadian Wildland Fire Strategy. A 10-year review and renewed call to action." Canadian Council of Forest Ministers, Tech. Rep., 2016. [Online]. Available: https://cfs.nrcan.gc.ca/publications?id=37108

[11] Natural Resources Canada, "Forest fires." [Online]. Available: https://natural-resources.canada.ca/our-natural-resources/forests/wildland-fires-insects-disturbances/forest-fires/13143

[12] "Software Overview." [Online]. Available: https://px4.io/software/software-overview/

[13] O. Yakimenko and N. Slegers, "Equations of Motion," in *Precision Aerial Delivery Systems: Modeling, Dynamics, and Control*, ser. Progress in Astronautics and Aeronautics. American Institute of Aeronautics and Astronautics, Jan. 2015, pp. 263–352.

[14] T. Jann, "Aerodynamic Model Identification and GNC Design for the Parafoil-Load System ALEX," in *16th AIAA Aerodynamic Decelerator Systems Technology Conference and Seminar*. Boston, MA: American Institute of Aeronautics and Astronautics, May 2001.

[15] G. Brown *et al.*, "The Affordable Guided Airdrop System (AGAS)," in *15th Aerodynamic Decelerator Systems Technology Conference*. Toulouse, France: American Institute of Aeronautics and Astronautics, Jun. 1999.

[16] S. Dellicker, R. Benney, and G. Brown, "Guidance and Control for Flat-Circular Parachutes," *Journal of Aircraft*, vol. 38, no. 5, pp. 809–817, Sep. 2001.

[17] O. A. Yakimenko *et al.*, "Synthesis of Optimal Control and Flight Testing of an Autonomous Circular Parachute," *Journal of Guidance, Control, and Dynamics*, vol. 27, no. 1, pp. 29–40, Jan. 2004.

[18] O. Yakimenko *et al.*, "On Control of Autonomous Circular Parachutes," in *AIAA Guidance, Navigation, and Control Conference and Exhibit*. Monterey, California: American Institute of Aeronautics and Astronautics, Aug. 2002.

[19] T. D. Fields, J. C. LaCombe, and E. L. Wang, "Autonomous Guidance of a Circular Parachute Using Descent Rate Control," *Journal of Guidance, Control, and Dynamics*, vol. 35, no. 4, pp. 1367–1370, Jul. 2012.

[20] ——, "Time-Varying Descent Rate Control Strategy for Circular Parachutes," *Journal of Guidance, Control, and Dynamics*, vol. 38, no. 8, pp. 1468–1477, Aug. 2015.

[21] T. D. Fields and O. A. Yakimenko, "Development of a Steerable Single-Actuator Cruciform Parachute," *Journal of Aircraft*, vol. 55, no. 3, p. 1041–1049, May 2018.

[22] ——, “Feasibility of a Steerable Single-Actuator Cruciform Parachute for Targeted Aerial Delivery,” in *24th AIAA Aerodynamic Decelerator Systems Technology Conference*, Jun. 2017.

[23] S. M. Herrington, T. D. Fields, and O. A. Yakimenko, “Flight Performance of Steerable Cruciform Parachute Systems,” in *31st Congress of the International Council of the Aeronautical Sciences*, Sep. 2018.

[24] T. D. Fields and O. A. Yakimenko, “The use of a steerable single-actuator cruciform parachute for targeted payload return,” in *2017 IEEE Aerospace Conference*, Mar. 2017, pp. 1–8.

[25] S. Dunker *et al.*, “Guided Parafoil High Altitude Research (GPHAR) Flight at 57,122 ft,” in *23rd AIAA Aerodynamic Decelerator Systems Technology Conference*. Daytona Beach, FL: American Institute of Aeronautics and Astronautics, Apr. 2015.

[26] S.-J. Lee and A. Arena, “Autonomous Parafoil Return-to-Point Vehicle for High Altitude Ballooning,” in *AIAA Guidance, Navigation, and Control Conference*, ser. AIAA SciTech Forum. American Institute of Aeronautics and Astronautics, Jan. 2014.

[27] N. Slegers and O. Yakimenko, “Optimal Control for Terminal Guidance of Autonomous Parafoils,” in *20th AIAA Aerodynamic Decelerator Systems Technology Conference and Seminar*. Seattle, WA: American Institute of Aeronautics and Astronautics, May 2009.

[28] O. Yakimenko, “PADS and Measures of Their Effectiveness,” in *Precision Aerial Delivery Systems: Modeling, Dynamics, and Control*, ser. Progress in Astronautics and Aeronautics. American Institute of Aeronautics and Astronautics, Jan. 2015, pp. 1–71.

[29] A. G. Sim *et al.*, “Development and flight test of a deployable precision landing system,” *Journal of Aircraft*, vol. 31, no. 5, pp. 1101–1108, Sep. 1994.

[30] P. Mortaloni *et al.*, “On the Development of a Six-Degree-of-Freedom Model of a Low-Aspect-Ratio Parafoil Delivery System,” in *17th AIAA Aerodynamic Decelerator Systems Technology Conference and Seminar*, May 2003.

[31] E. González *et al.*, “Development of a 6-DoF Simulator for Analysis and Evaluation of Autonomous Parafoil Systems,” International Centre for Numerical Methods in Engineering, Tech. Rep., Apr. 2011.

[32] M. Ward, S. Culpepper, and M. Costello, “Parametric Study of Powered Parafoil Flight Dynamics,” in *AIAA Atmospheric Flight Mechanics Conference*, ser. Guidance, Navigation, and Control and Co-located Conferences. American Institute of Aeronautics and Astronautics, Aug. 2012.

[33] C. Cumer *et al.*, “Simulation of generic dynamics flight equations of a parafoil/payload system,” in *2012 20th Mediterranean Conference on Control & Automation (MED)*, Jul. 2012, pp. 222–228.

[34] N. Slegers and C. Gorman, “Comparison and Analysis of Multi-body Parafoil Models With Varying Degrees of Freedom,” in *21st AIAA Aerodynamic Decelerator Systems Technology Conference and Seminar*, ser. Aerodynamic Decelerator Systems Technology Conferences. American Institute of Aeronautics and Astronautics, May 2011.

[35] G. Strickert, “Study on the relative motion of parafoil-load-systems,” *Aerospace Science and Technology*, vol. 8, no. 6, pp. 479–488, Sep. 2004.

[36] N. Slegers, E. Beyer, and M. Costello, “Use of Variable Incidence Angle for Glide Slope Control of Autonomous Parafoils,” *Journal of Guidance, Control, and Dynamics*, vol. 31, no. 3, pp. 585–596, May 2008.

[37] M. Ward, M. Costello, and N. Slegers, “Specialized System Identification for Parafoil and Payload Systems,” *Journal of Guidance, Control, and Dynamics*, vol. 35, no. 2, p. 588–597, Mar. 2012.

[38] R. A. Fisher, “On an Absolute Criterion for Fitting Frequency Curves.” *Messenger of Mathematics*, vol. 41, pp. 155–160, 1912.

[39] ——, “On the mathematical foundations of theoretical statistics,” *Philosophical Transactions of the Royal Society of London*, vol. 222, no. 594-604, pp. 309–368, 1922.

[40] ——, “Theory of Statistical Estimation,” *Mathematical Proceedings of the Cambridge Philosophical Society*, vol. 22, no. 5, pp. 700–725, 1925.

[41] P. Hamel and R. Jategaonkar, “Evolution of Flight Vehicle System Identification.” *Journal of Aircraft*, vol. 33, pp. 10–28, Jan. 1996.

[42] N. Slegers and M. Costello, “Model Predictive Control of A Parafoil and Payload System,” *Journal of Guidance, Control, and Dynamics*, vol. 28, no. 4, pp. 816–821, 2005.

[43] M. Ward and M. Costello, “Adaptive Glide Slope Control for Parafoil and Payload Aircraft,” *Journal of Guidance, Control, and Dynamics*, vol. 36, no. 4, pp. 1019–1034, 2013.

[44] A. Gavrilovski, M. Ward, and M. Costello, “Parafoil Glide Slope Control Using Canopy Spoilers,” in *21st AIAA Aerodynamic Decelerator Systems Technology Conference and Seminar*, ser. Aerodynamic Decelerator Systems Technology Conferences. American Institute of Aeronautics and Astronautics, May 2011.

[45] C. Gorman and N. Slegers, “Modeling of Parafoil-Payload Relative Yawing Motion on Autonomous Parafoils,” in *21st AIAA Aerodynamic Decelerator Systems Technology Conference and Seminar*. American Institute of Aeronautics and Astronautics, May 2011.

APPENDIX A COMPLETE LIST OF SIMPLFYING ASSUMPTIONS

Atmospheric conditions and wind

ISA atmosphere model

ASM–A1. Atmospheric conditions are constant in time.

ASM–A2. Air behaves as an ideal gas.

ASM–A3. The atmosphere has mass, and this mass induces a vertical pressure gradient that can be calculated through hydrostatic equilibrium.

ASM–A4. Temperature evolves linearly with altitude within a series of altitude segments.

Wind Model

ASM–A5. Wind velocities are constant over the duration of a flight segment.

ASM–A6. The wind has no vertical component.

Parafoil dynamics and kinematics

6-DOF model

ASM–D1. The parafoil operates on a flat, nonrotating Earth with constant gravitational acceleration.

ASM–D2. The payload and canopy act as a single rigid body.

4-DOF model

ASM–D3. Aerodynamic side-force is neglected. $(Y = 0)$

ASM–D4. Lift and drag coefficients are linearly dependent on symmetric brake deflection.

ASM–D5. Aerodynamic forces are independent of the angle of attack.

ASM–D6. The relationship between asymmetric brake deflection on roll angle can be modeled as a first-order transfer function.

ASM–D7. Aerodynamic moments are implicitly handled by the roll angle model.

ASM–K1. Pitching is neglected ($\theta = \dot{\theta} = 0$)

ASM–K2. The system has no lateral aerodynamic velocity ($v_a = \dot{v}_a = 0$)

ASM–K3. Sideslip is neglected ($\beta = 0$)

APPENDIX B DETAIL OF THE 6-DOF SIMULINK PARAFOIL MODEL

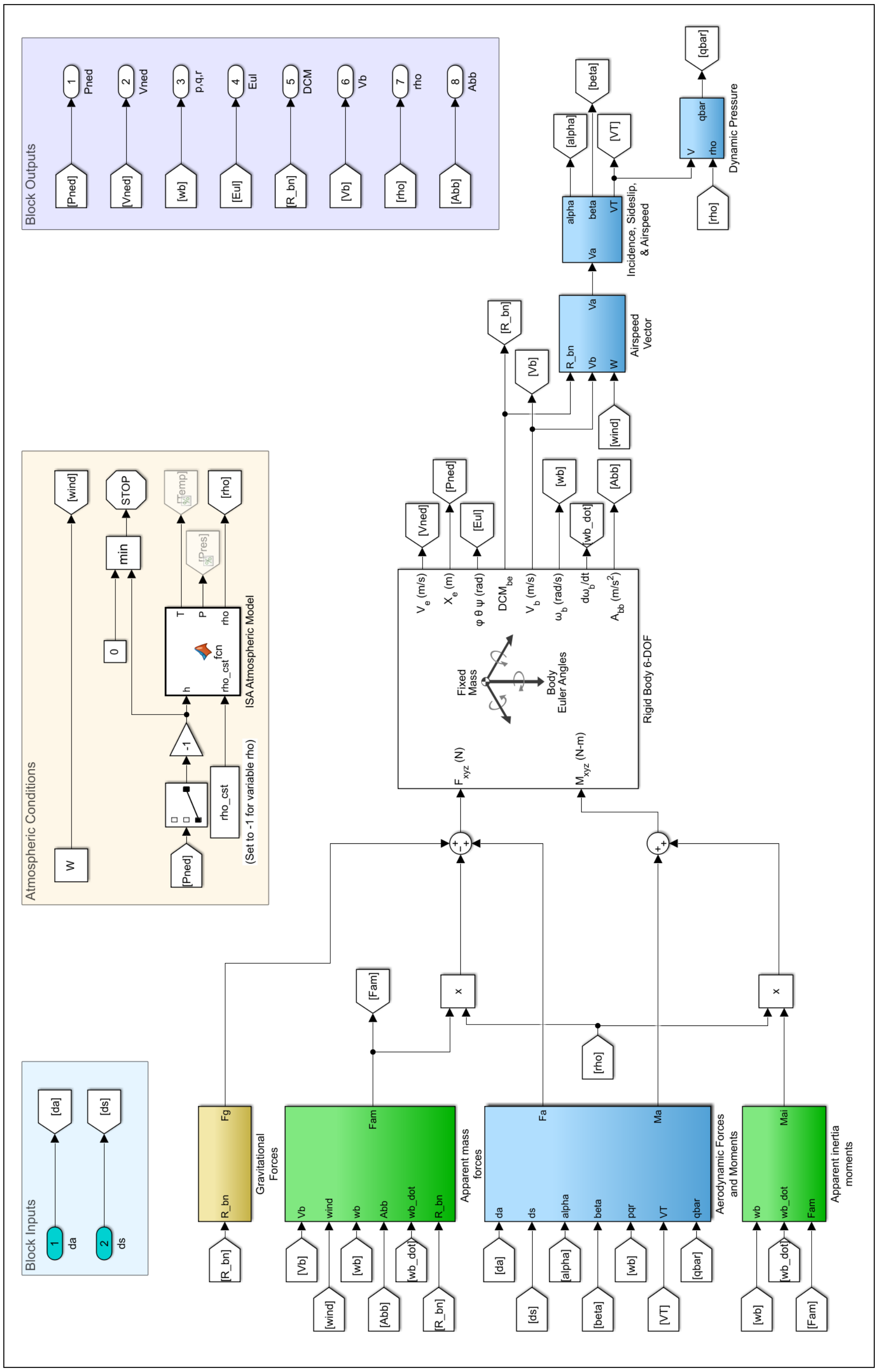

Figure B.1 Full 6-DOF Model in Simulink

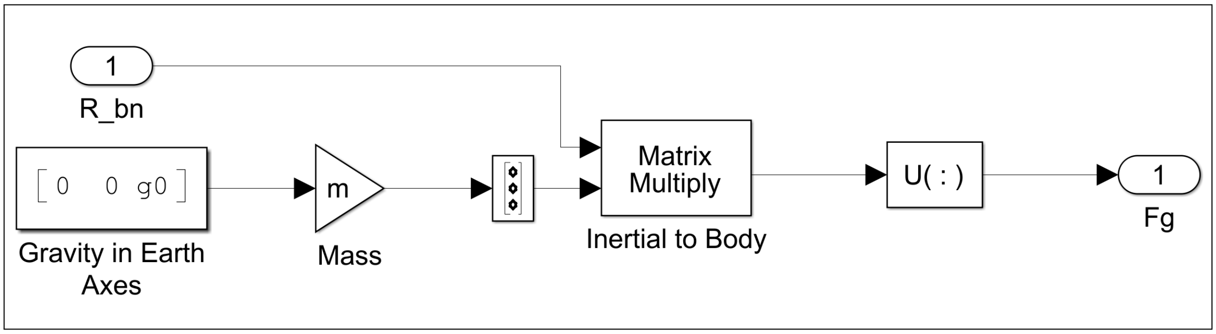

Figure B.2 Contents of the *Gravitational Forces* block

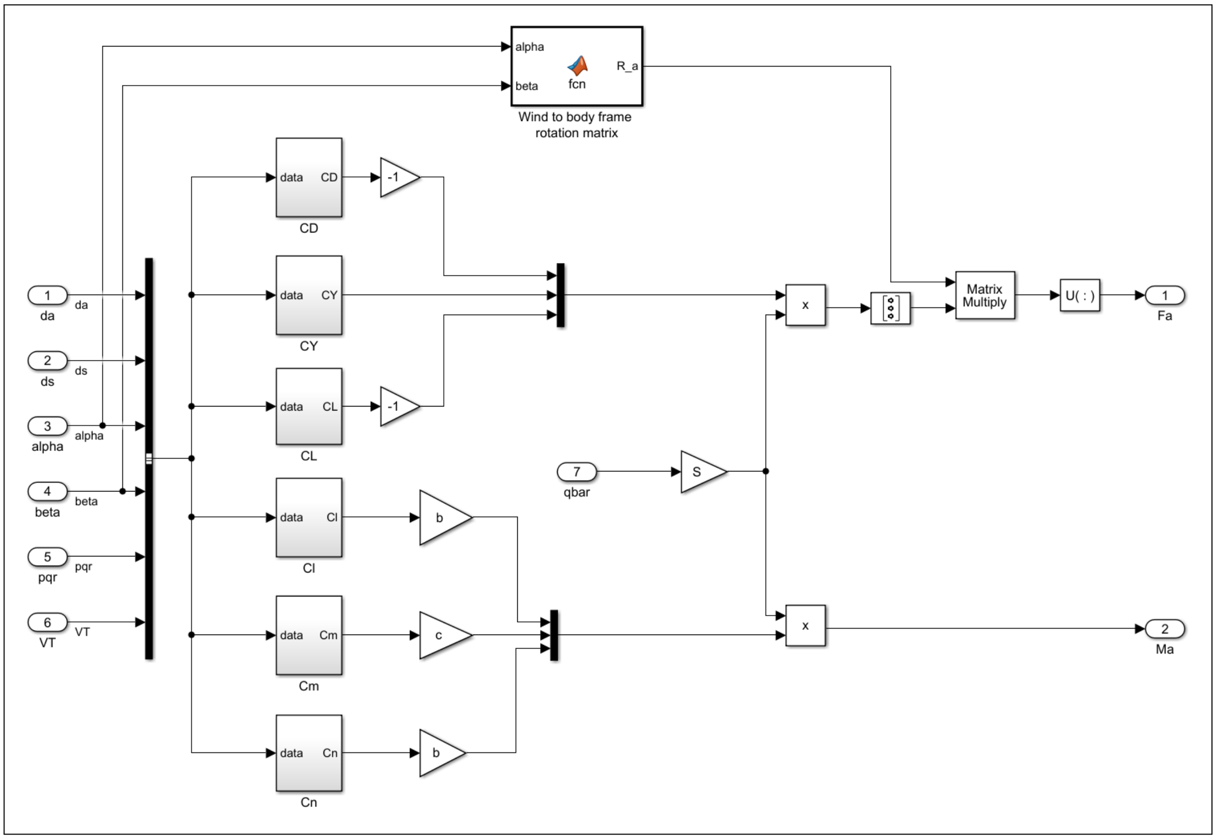

Figure B.3 Contents of the *Aerodynamic Forces and Moments* block

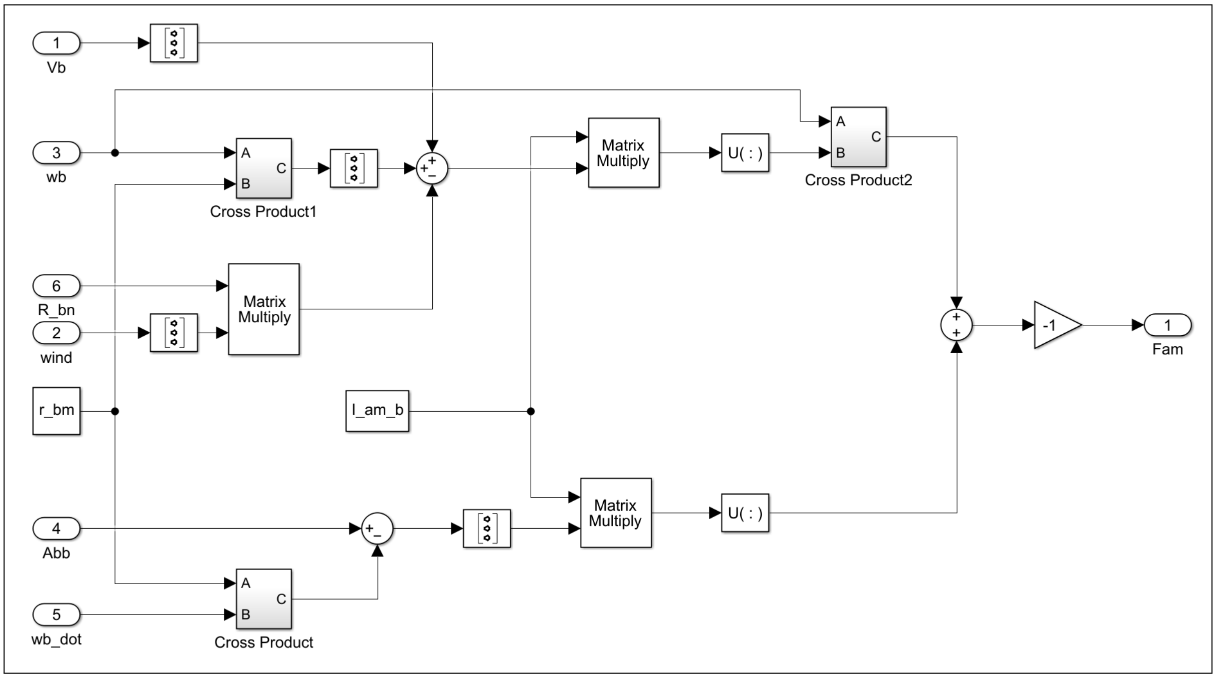

Figure B.4 Contents of the *Apparent Mass Forces* block

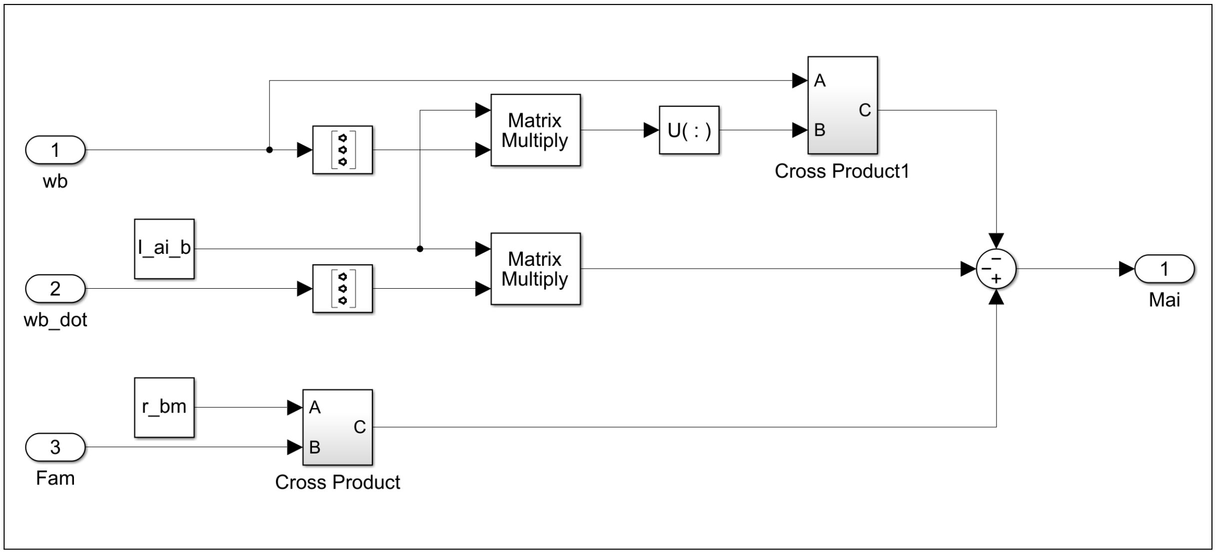

Figure B.5 Contents of the *Apparent Inertia Moments* block

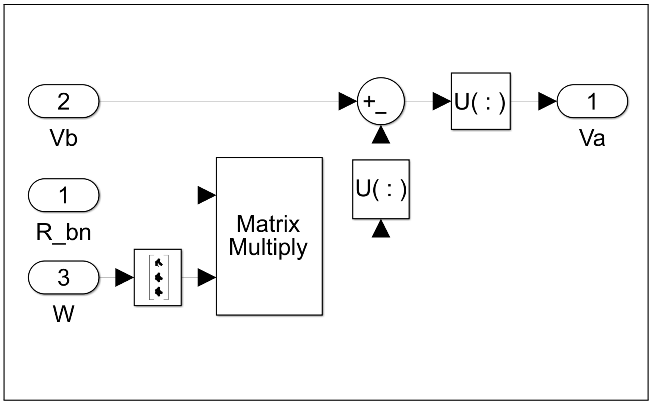

Figure B.6 Contents of the *Airspeed Vector* block

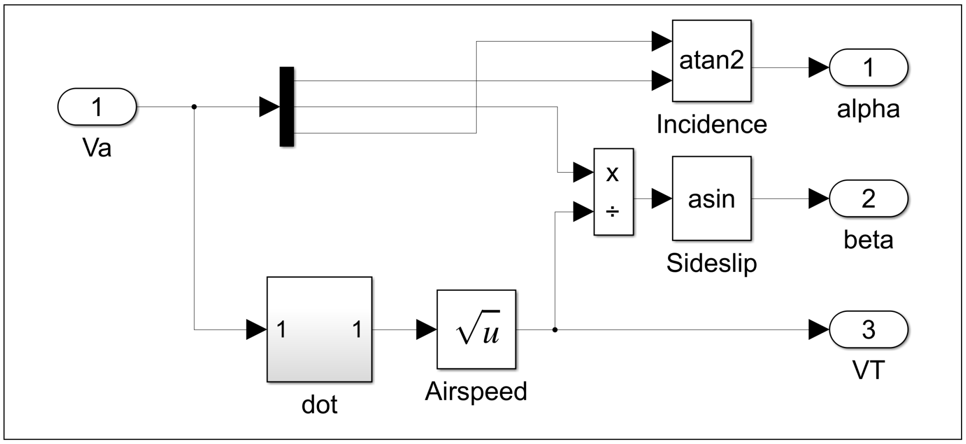

Figure B.7 Contents of the *Incidence, Sideslip & Airspeed* block

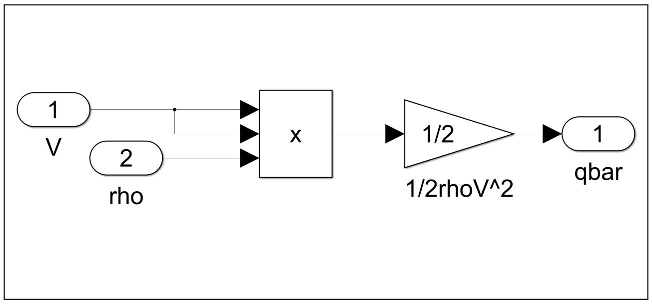

Figure B.8 Contents of the *Dynamic Pressure* block

APPENDIX C DETAIL OF THE 4-DOF SIMULINK PARAFOIL MODEL

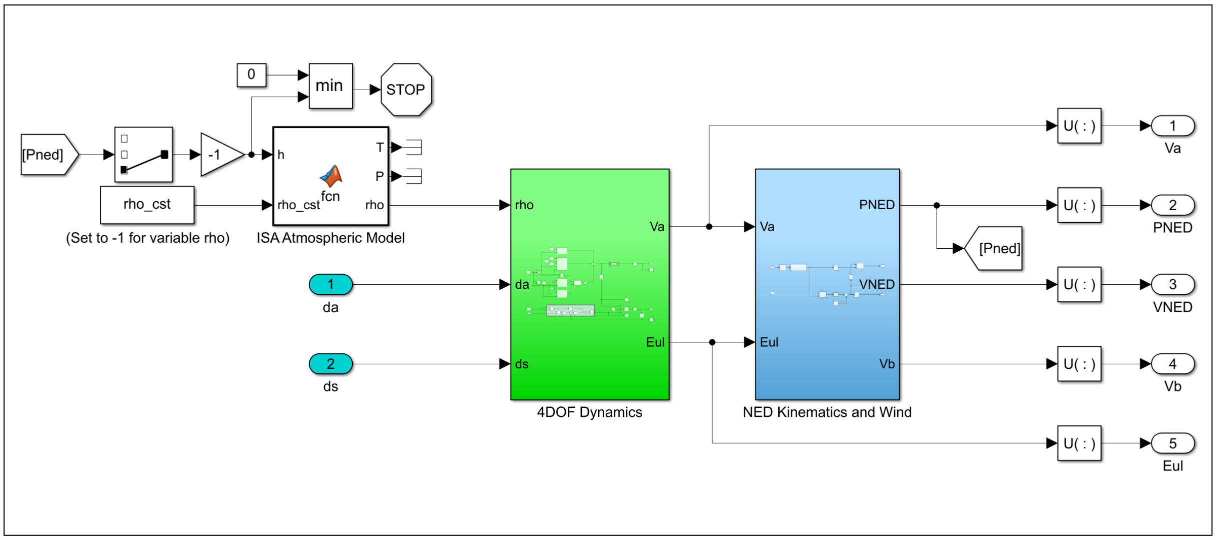

Figure C.1 Full 4-DOF Model in Simulink

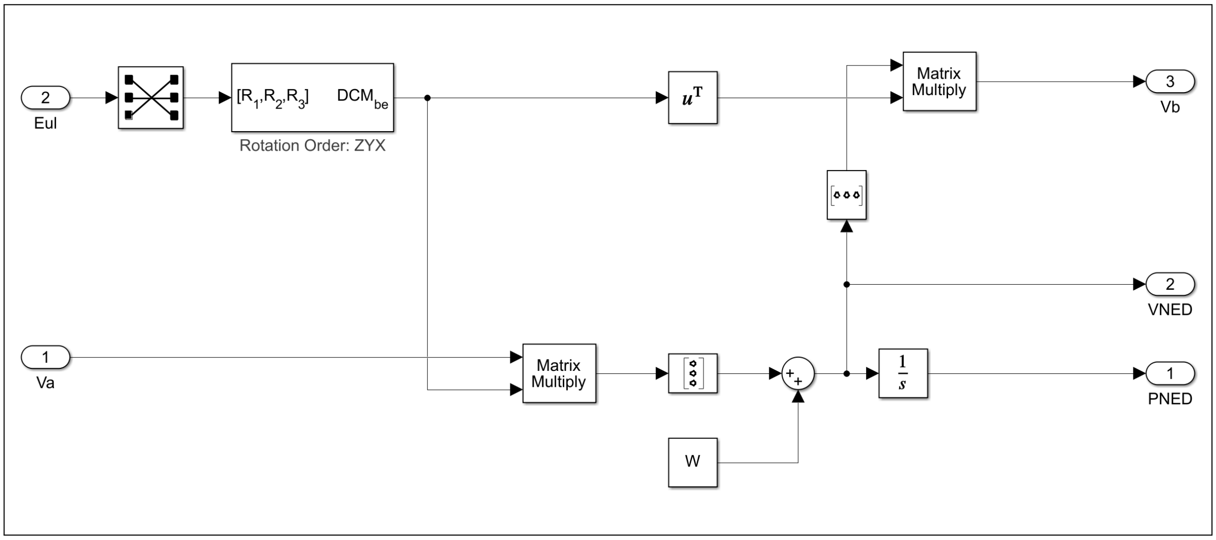

Figure C.2 Contents of the *NED Kinematics and Wind* block

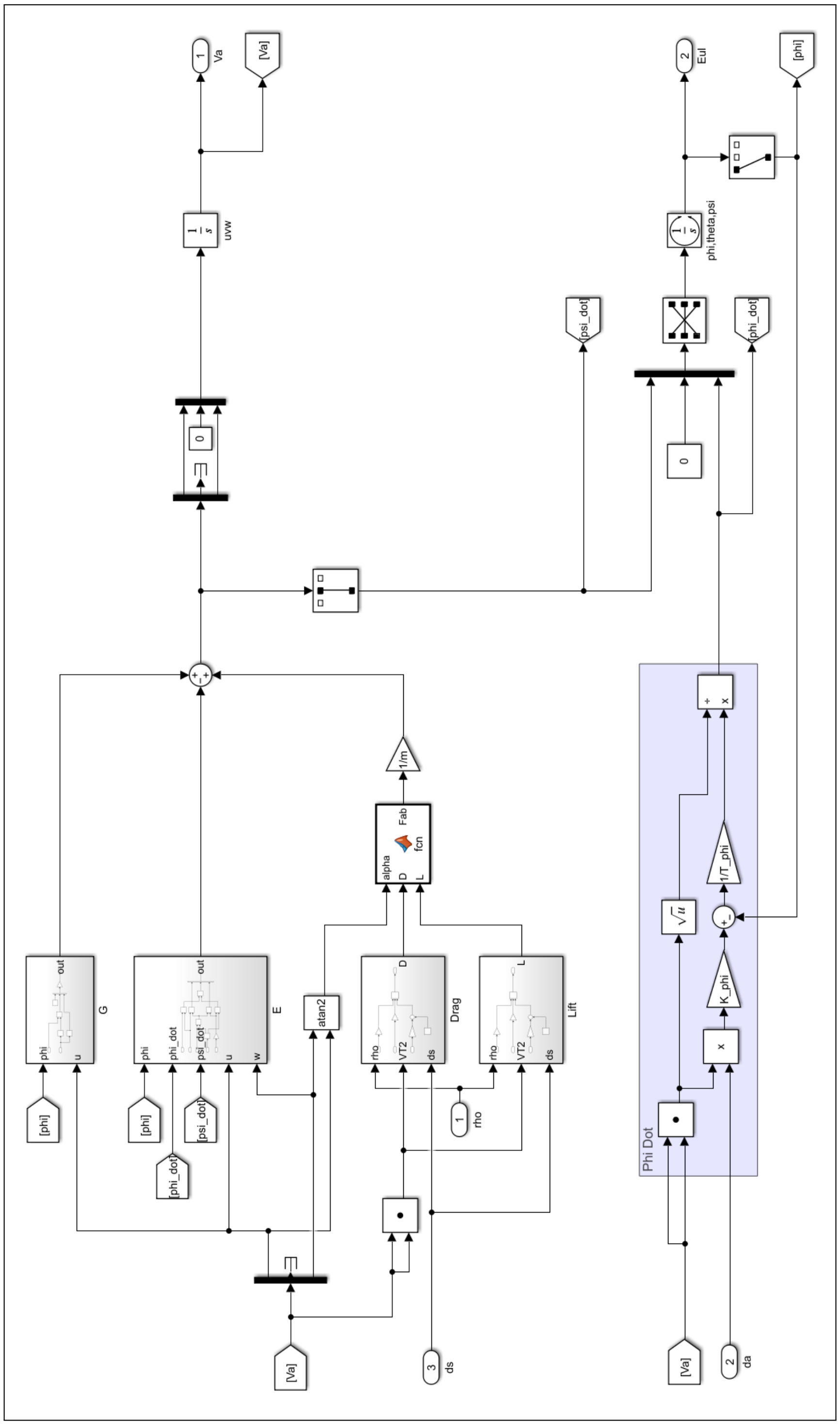

Figure C.3 Contents of the *4-DOF Dynamics* block

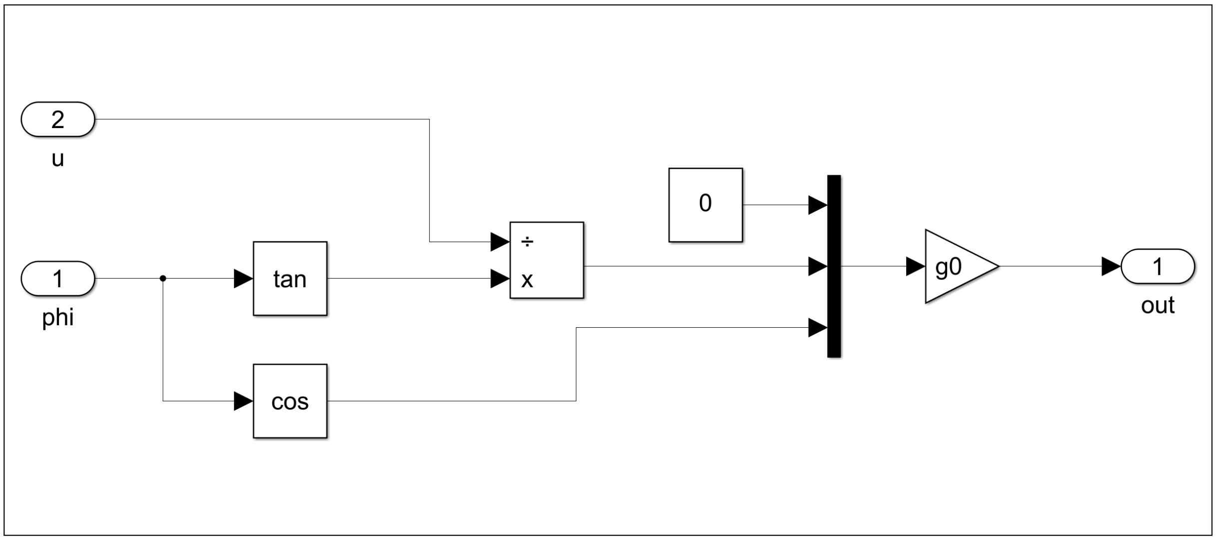

Figure C.4 Contents of the *4-DOF Dynamics/G* block

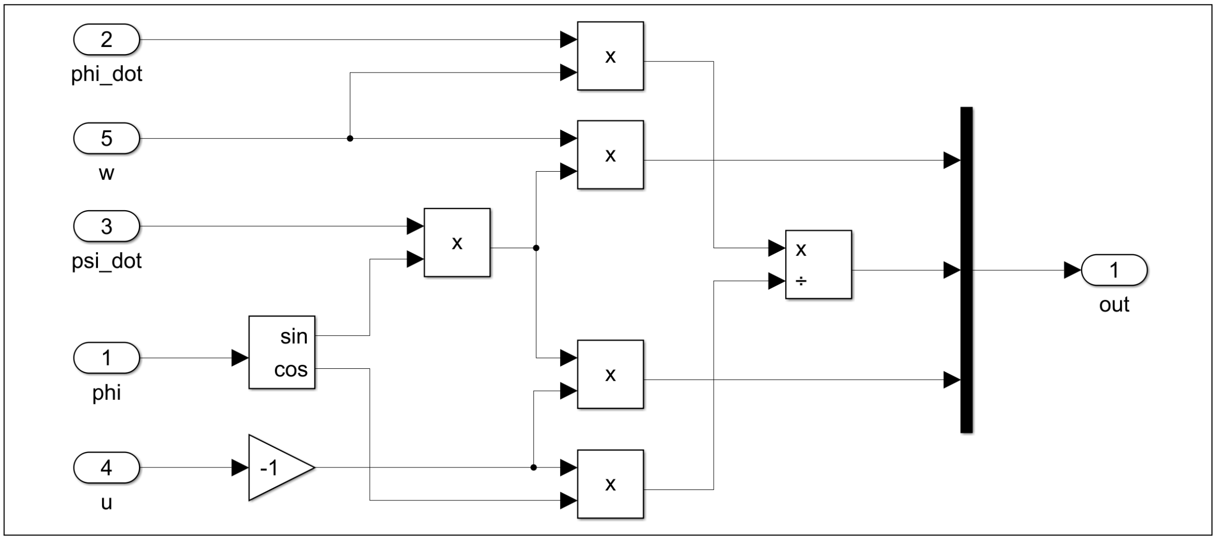

Figure C.5 Contents of the *4-DOF Dynamics/E* block

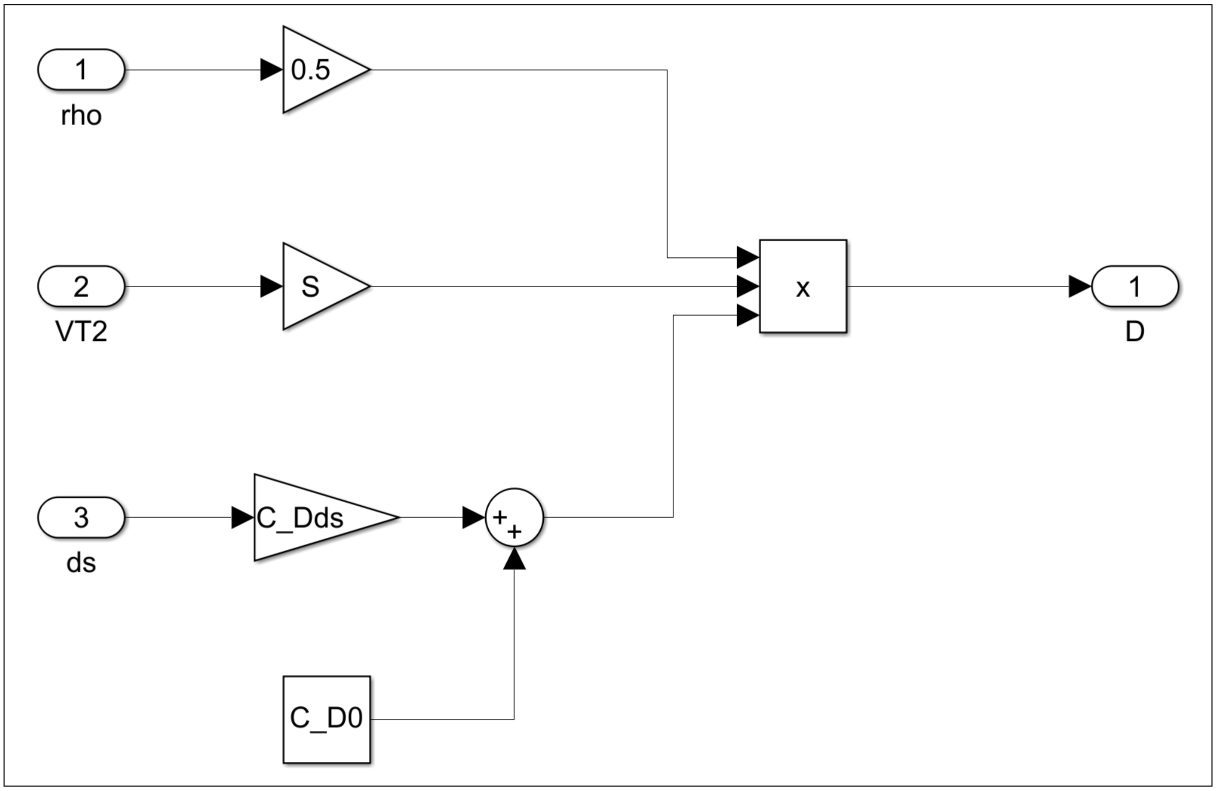

Figure C.6 Contents of the *4-DOF Dynamics/Drag* block

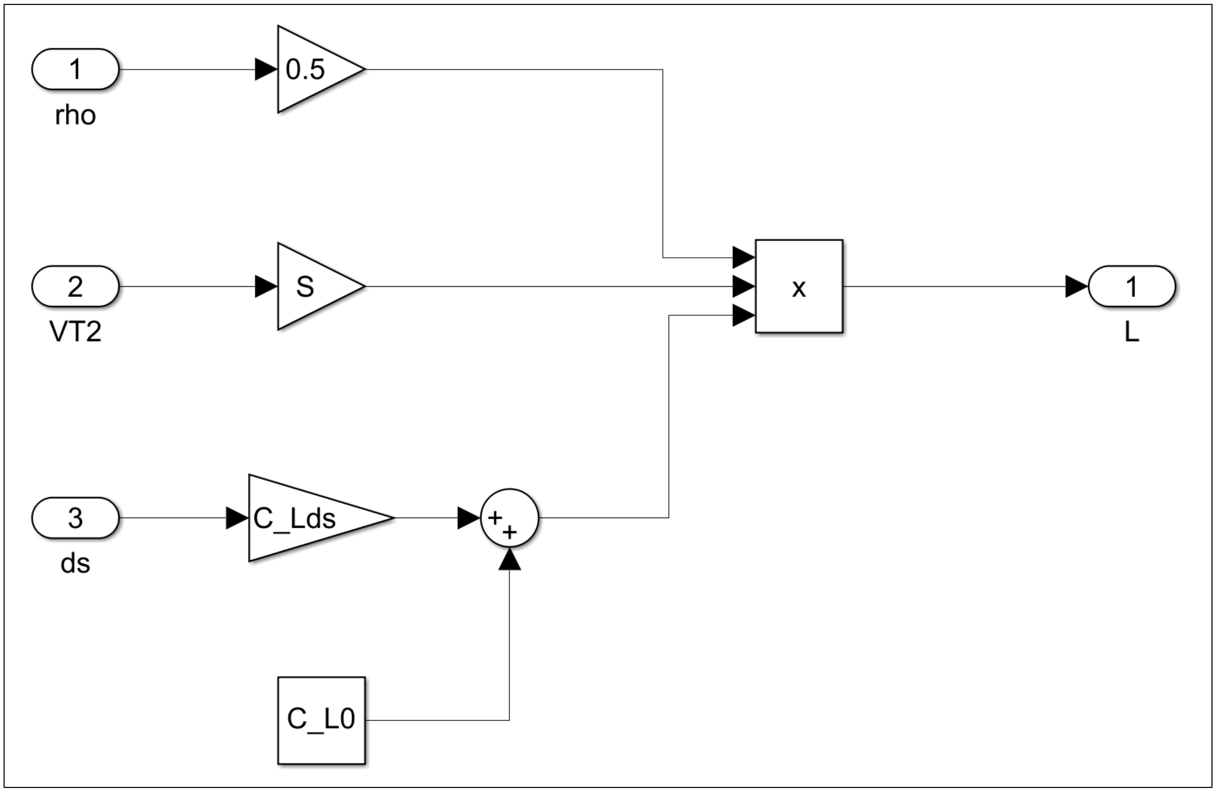

Figure C.7 Contents of the *4-DOF Dynamics/Lift* block